Université d'Ottawa · University of Ottawa

Prediction of Passive Scalar in a Mixing Layer using Vortex-In-Cell and Probability Density Function methods

Arif M. Baig

A thesis submitted to the Faculty of Graduate and Postdoctoral Studies
in partial fulfilment of the requirements for the degree of

MASTER OF APPLIED SCIENCE

in Mechanical Engineering

Ottawa-Carleton Institute for Mechanical and Aerospace Engineering
University of Ottawa
Ottawa, Canada

December 2001

Abstract

The transport equation for the probability density function (p.d.f.) of a scalar is applied in conjunction with the vortex-in-cell (VIC) method developed by Abdolhosseini and Milane (1998), to predict the passive scalar field in a two-dimensional spatially growing mixing layer. The VIC method predicts the instantaneous velocity field. Then the turbulent flow characteristics such as mean velocity, the root-mean-square (r.m.s.) longitudinal and lateral velocity fluctuations and the Reynolds shear stress are calculated. The scalar field is represented through the transport equation for the scalar p.d.f. and is solved using the Monte Carlo technique. In the p.d.f. equation, turbulent diffusion is modeled using the gradient transport model, wherein the eddy diffusivity is computed using Boussinesq's postulate and using the Reynolds shear stress and gradient of mean velocity from the VIC solution. The molecular mixing term is closed by a modified Curl model, and the convection term uses the mean velocity from the VIC solution.

The computational results were compared with available two-dimensional experimental results. The predicted turbulent flow characteristics, i.e., mean velocity and r.m.s. longitudinal fluctuation in the simulations' region of similarity, show a good agreement with the experimental measurements. Mixing statistics of the passive scalar are also in reasonable agreement with the experimental measurements. Comparison between the mean concentration profile and the mean velocity profile shows the scalar mixing region extends further into the free stream than does the momentum mixing region, indicating enhanced transport of scalars over momentum. The r.m.s. concentration profiles exhibit

mixing asymmetry, with high speed fluid mixing at a faster rate than the low speed fluid. The asymmetry in the present work, however, is found to be due to the selection of the value of the centre of the tangent hyperbolic profile, used as inflow boundary condition in the scalar field simulation. The p.d.f. shape of the passive scalar shows higher mixed fast stream fluid probabilities over a larger cross-stream extent of the mixing layer as compared with the slow stream fluid. The effect of Schmidt number, mixing models, and variation of mixing frequency is also evaluated.

Acknowledgements

I wish to express my gratitude to my advisor, Dr. Roger Milane, for his time, ideas and guidance, which he supplied throughout the course of my graduate studies. In addition, I thank him for sharing his wealth of experience with me.

I wish to express my appreciation to the academic members and staff of the department of mechanical engineering, especially Solange Lamontagne, Marie Rainville, Lise Ouellet, Ruth Neil and France Raincourt for their help.

I would also like to thank my friends and colleagues for their suggestions and encouragement.

Finally, I would like to thank my parents and members of the family for their continual support and encouragement.

Table of Contents

Chapter 3. Formulations and Numerical Schemes (VIC)

Chapter 4. Formulations and Numerical Schemes (PDF)

Chapter 5. Results

List of Figures

Figure 5.29: PDF shape of passive scalar at several cross-stream locations, for downstream station x=24cm (x/H=0.75). a) η_c=0.054; b) η_c=0.024; c) η_c=0.002; d) η_c=-0.01; e) η_c=-0.02; f) η_c=-0.035.

Nomenclature

Latin Symbols

A	Area of the cell
d	Distance between point vortices
dt	Time step
dx, dy, dz	Distances in a cell
c	Concentration
$c_{U,} c_L$	Concentration of the free stream above and below the splitter plate
c_c	Average concentration
H	Computational domain length
k	Turbulent kinetic energy
L	Length of the computational domain
M	Number of vortices
n	Number of particles
N	Number of particles at a node
P, p	Probability
PDF, pdf	Probability density function
r	Velocity ratio
$R_{i,j}$	Residual
S_{cT}	Turbulent Schmidt number
t	Time
u	Velocity vector
u,v	Cartesian velocity components
u′,v′	Turbulent velocity fluctuations
u_n,v_n	Velocity components of the vortices
U	Mean velocity in stream-wise direction
U_H,U_L	Fast upper and slow lower free stream velocities
U_c	Arithmetic average of the free stream velocities
x_v, x_c	Virtual origins for velocity and concentration
x,y	Cartesian coordinates
x_n, y_n	Coordinates of the vortices
y_0	y-coordinate of the centerline
Δx,Δy	Cell size in the vortex-in-cell method

Greek Symbols

C_ϕ	Constant
Γ	Circulation

Γ_n	Circulation of the vortex element number n
Γ_x, Γ_y	Components of circulation vector of vortex elements
δ_w	Vorticity thickness
η_v	Similarity variable for velocity
η_c	Similarity variable for concentration
η_c'	Similarity variable for concentration (includes a spreading factor)
μ	Viscosity
ν	Kinematic viscosity
ν_T	Eddy viscosity, turbulent diffusivity
ρ	Density
σ	Core size radius
σ_0	Initial core size
χ	Trajectories of vortices
ψ	Stream function
ω_f	Mixing frequency
$\boldsymbol{\omega}$	Vorticity vector
ω_x,ω_y	Components of vorticity vector
ξ	Mixture fraction, or concentration
α	A variable specified by distribution function describing the mixing model
β	A co-effecient describing the mixing model
ϵ	Dissipation rate of kinetic energy
Ω_{rms}	Root-mean-square of vorticity
γ_T	Scalar diffusivity

Chapter 1

Introduction

1.1 Turbulent Mixing Layer Flow

Turbulence is a universal phenomenon of fluids. Most aspects of nature, as well as engineering, involve turbulent flows. These flows are very efficient at mixing fluids. Turbulent flows, instead of being simply laminar or smooth, are highly irregular and complex, containing many co-existing vortices, eddies, or swirling motions of different sizes and shapes. The physics of turbulent flows, notably the ability of turbulence to stir fluids across many scales simultaneously, results in accelerated fluid mixing which occurs much faster compared to simple molecular diffusion. Humans interact with turbulence in many contexts. Examples include flow past cars, flow around and inside aircraft, flow in propulsion engines, flow in the atmosphere, flow of blood in arteries, and flow generated by a golf ball. Turbulence is, in essence, a problem in statistical dynamics. It is a superposition of an irregular eddying motion on a mean stream whose detailed configuration is neither reproducible from one experiment to the next nor predictable theoretically, but whose statistical properties are significant (Phillips, 1969).

Turbulent flows can be defined by a set of characteristics. These flows have a disorder which is not reproducible in detail. They mix efficiently and they have vorticity fluctuations in three dimensions. Turbulent flows are three-dimensional, but something like turbulent motion can occur in two dimensions. Large-scale weather systems and the flow in a plane mixing layer have some of this character. However, in a two-dimensional flow, vorticity behaves as a scalar, and there is no vorticity production by vortex filament stretching. Another basic concept in defining turbulence is the " cascade". Turbulent flows are composed of eddies, also known as vortices, in a broad range of sizes. The largest eddies are produced by the forces driving the flow. These large groups of fluid particles move laterally or longitudinally in the flow field. While undergoing these motions, an eddy can change its shape or stretch, and rotate or break into two or more eddies. Large eddies break down into smaller ones, which break down into yet smaller eddies, and so on. This process continues until eventually molecular viscosity suppresses further cascading and dissipates the eddies. One of the main characteristics of the eddies is vorticity, which may be distributed throughout the entire fluid, but often the vorticity is very large only in a thin thread of fluid while the remaining fluid is virtually without vorticity. Therefore, a simplified approach is to view all the vorticity lumped into a concentrated vortex filament around which the fluid spins. The mutually-induced velocities of these vortex filaments cause some of them to stretch, and this stretching produces turbulence with smaller eddies and higher vorticity.

Turbulent mixing governs the flow field in combustion chambers and flow reactors whose size or efficiency depends on the rate of mixing. Often in combustion devices one works to increase the turbulence level of the flow to increase mixing and therefore, have

more efficient burning. In any real fluid the action of the viscosity causes the dissipation of the kinetic energy, and in the absence of any external source the turbulent motion will decay. One of the simplest ways of producing and maintaining turbulence is using mean shear flow. The plane mixing layer where two initially separated parallel flows come into contact and mix is one of the simplest conceivable free shear flows, and a generic mixing configuration for many practical applications. The fundamentals of plane mixing layers have been the subject of extensive theoretical and experimental investigations due to their apparent simplicity, common technological occurrences, and significant importance in mixing processes, often combined with chemical reactions and combustion. The plane mixing layer is representative of the mixing and reaction zones that exist in real combustion devices. The engineering applications of the mixing layer are found in gas turbine combustors, chemical lasers, flow behind inlet valves in internal combustion engines, and many others.

The governing equations of turbulent flows are known, namely those of conservation of mass, momentum and energy. Due to the complexity of turbulent flows most of the information about the characteristics of turbulent flows is obtained from experiments. Recent advances in computer technology have made feasible the numerical simulation of turbulent flows. Following is a brief explanation of various methods of computing turbulent flows.

1.2 Direct Numerical Simulation

Direct numerical simulation (DNS) of turbulent flow employs a grid fine enough so that all scales of motion in the flow can be calculated directly from the Navier Stokes equations.

Since DNS resolves all scales of motion, no additional modeling is needed to account for the effects of turbulence. In this approach, rather than averaging the equations first, a time and space resolved flow field is computed, and then an ensemble average is taken to enable comparison with the experiments. The only errors made in the DNS approach are numerical ones. The DNS is then the most attractive approach, but computationally very demanding. The range of scales or size of whirling eddies, in turbulence, can vary 1000 fold or even more. The computational grid for DNS must be fine enough to resolve the smallest eddies, but large enough to encompass all the large scale motions. The scales of motion increase rapidly with the increase in Reynolds number, therefore, the application of the DNS approach is limited to low Reynolds numbers. Examples of DNS calculations can be found in Shirani et al. (1981), Feiereisen et al. (1981), Rogallo (1981), Corcos and Sherman (1984) and Riley et al. (1986).

1.3 Reynolds Averaged Equations

In this method, the Navier-Stokes equations are averaged over the scales of turbulent fluctuations. Averaging may be over time or homogeneous directions in the flow. When the averaging is performed, the equations of motion contain averages of products of fluctuating velocities, and the number of unknowns is more than the number of equations. This is the well-known "closure problem", because the set of equations can never be closed by further averaging. To close the problem, empirical models must be constructed to relate the additional variables to the old ones. The Reynolds Averaged Navier-Stokes (RANS) method

is one of the most affordable methods of computing turbulent flows because velocity fluctuations are not calculated, and all turbulent scales are modelled. The weakness of RANS is that it is not an appropriate method for a Lagrangian type simulation of turbulent flows, because, when the velocity fluctuations are not calculated, a Lagrangian element cannot be traced at each time step. In other words, RANS methods may be applied for the numerical simulation of the shear flows using an Eulerian approach.

1.4 Large Eddy Simulation

A method that lies between DNS and RANS is the Large Eddy Simulation (LES). The dynamics of turbulence are largely determined by the large scale eddies. Experimental observation indicate that the large scale motions differ from one flow to another, but the small scale motions are almost universal. The large eddies contains the most energy and are responsible for setting the rate of energy transfer to smaller eddies through the energy cascade. The small eddies are relatively passive, taking the energy that is cascaded down from larger scales and dissipating that energy through molecular viscosity into internal energy. The small scale eddies tend to be approximately isotropic (Rogallo and Moin 1984). This means that modeling of the small scale turbulence is significantly easier than modeling all the scales of a turbulent flow since the large scale eddies are usually highly anisotropic. In LES the large scale eddies in the flow are fully resolved while the small scale eddies are modeled using a turbulence model. A spatial filter function can be employed to filter a range of small scales (subgrid scales) in the momentum or vorticity equations. In these filtered

equations, the terms representing the large scale structures are separated from those representing the small scale motions, Leonard (1974). The effect of the small eddies is then introduced using subgrid scale models. As a result, large eddy motions of the resolved scales are simulated by solving the filtered Navier-Stokes equations. This approach was first used by Smagorinski (1963), followed by Lilly (1967). Other examples can be found in Leslie and Quarini (1979), Bardina et. al. (1980), Antonopoulos (1981), Rogallo and Moin (1984), Lin and Pratt (1987), Lesieur (1995), Milane and Nourazar (1995 and 1997).

1.5 Vortex Methods

Vortex methods are a tool for the direct numerical simulation of incompressible viscous flows; however, large eddy simulation using vortex methods has also been done (Lin and Pratt 1987). Vortex methods offer an alternative to finite difference and spectral methods for high resolution numerical solutions of the Navier Stokes equation. Unlike other numerical methods, such as finite difference and finite elements, the vortex methods are fundamentally linked to the physics they aim to produce (Koumoutsakos 1999). Vortex methods are based on the discretization of the vorticity field and the Lagrangian description of the governing equations that, when solved, determine the evolution of the computational elements. Vortex methods have been used extensively to simulate incompressible flows, especially two-dimensional problems. In the pure Lagrangian approach, the basic idea is the application of the Biot-Savart law of interaction between vortices. The Biot-Savart law can be derived mathematically from the conservation of mass for a potential flow assuming an

incompressible fluid. It determines kinematically the instantaneous velocity field related to a given vorticity field. In this technique only fluid particles with concentrated vorticity (vortex points or blobs) need to be tagged and traced. As time proceeds, the change of vorticity distribution within a blob is governed by the vorticity transport equation. This method was first introduced by Rosenhead in 1931, prior to the availability of digital computers. Aided by computers, Abernathy and Kronauer (1962) used the point vortex method to simulate vortex streets. Chorin (1973) solved the two-dimensional problem through the use of vortex blobs. He also introduced a three-dimensional solution using a filament method. Ashurst (1979) applied Chorin's method to a two-dimensional mixing layer. The downstream evolution of the large scale structures were almost similar to Brown and Roshko's experiment (1974). A description of direct numerical simulation using vortex methods can be found in many papers, such as Leonard (1980), Inoue (1985), Ng and Ghoneim (1985), Ghoneim and Ng (1986), Inoue and Leonard (1987). The large eddy simulation using vortex methods can be found in Lin and Pratt (1987), and Milane and Nourazar (1995, 1997), amongst others. Also, the reviews of Clements and Maull (1975), Saffman (1981), and Sarpkaya (1994) give a complete description of the vortex methods.

Another approach which has been developed for calculating vortex problems is known as the vortex-in-cell(VIC) or the cloud-in-cell(CIC) method. This method combines some of the best features of both Lagrangian and Eulerian approaches. In the VIC method vortex markers are treated in a Lagrangian fashion, but these markers move through an Eulerian mesh system. In this method, the velocity field is calculated from Poisson's equation, and the vorticity distribution is obtained from the Laplacian of the stream function.

In the VIC method the Eulerian scheme is used to calculate the velocity field and the Lagrangian scheme to track the vortices. Examples of calculations employing the VIC method can be found in Christiansen (1973), Baker (1979), Aref and Siggia (1980). In addition, the reviews of Leonard (1980) and Sarpkaya (1994), provide a description of this technique.

1.6 Probability Density Function Methods

The evident importance of turbulent flows involving mixing and reaction has stimulated a wide variety of theoretical approaches. The aim of these approaches is to calculate the important properties of the flow field. For inert flows, the turbulence closure problem makes this a difficult task and, for reactive flows, the difficulty is compounded by non-linear reaction rates and large density variations. The pdf methods overcome the most important of these closure problems, some of which are discussed in later paragraphs. Also, in comparison to conventional turbulence models, the pdf methods derive their advantage from their more complete representation of the turbulent flow field (Pope 1985). Taking for example, a flow involving three scalar quantities. With a two-equation turbulence model (e.g. the k-ϵ model), this turbulent reactive flow is represented by eight quantities at each point (Launder and Spalding 1972). In the pdf method, on the other hand, this flow is represented by the joint pdf of the three velocities and the three scalars. At each point, this is a function of six independent variables. The six-dimensional joint pdf will then contain much more information than the eight quantities considered in the conventional turbulence model

approach (Pope 1985).

The pdf methods are well suited to flows with complex thermochemistry, and most of the work on the pdf's has been applied to reactive flows. However, compared to conventional turbulence models, the pdf methods also have many advantages for non-reactive flows. A modelled pdf equation was first solved by Lundgren (1969). He derived, modelled, and solved a transport equation for the joint pdf of velocity, in which convective transport appears in closed form. In mean flow closures a model is needed for the Reynolds stresses (which transport momentum), and in Reynolds stress closures a model is needed for the triple velocity correlations (which transport the Reynolds stresses). These transport processes are usually modelled by gradient diffusion, but in the velocity pdf equation these processes do not have to be modelled and so the gradient diffusion assumption is avoided.

Dopazo and O'Brien (1976), and Pope (1976) derived, modelled, and solved the transport equation for the composition joint pdf, that is, the joint pdf of a set of scalars (e.g. mass fractions and enthalpy). In this equation complicated reactions can be treated without approximation. This is in marked contrast to conventional turbulence models in which the mean reaction rate can be determined only in special circumstances, that is, when the reaction rate is linear or when it is either very fast or very slow compared with the turbulent time scales.

The modelled composition joint pdf equation has been solved for a variety of flows, demonstrating its ability to handle non-linear reactions. There have also been several solutions of the transport equation for the pdf of a conserved scalar. While the composition-pdf equation overcomes the closure problem associated with non-linear reaction rates, it does

not address the problem of determining the turbulent flow field. In most of the composition pdf calculations, the standard k-ϵ turbulence model is used to determine the mean velocity and turbulence fields. In the present work, the mean velocity, turbulent diffusivity and mixing frequency in a mixing layer are computed by the vortex-in-cell method, which predicts the instantaneous velocity field. The mean velocity, turbulent diffusivity and mixing frequency are then used as inputs to the transport equation for the pdf of a passive scalar. The turbulent transport is modelled by gradient diffusion.

Pope (1980), devised a Monte Carlo method to solve the composition joint pdf equation. For problems with large number of independent variables, Monte Carlo methods provide a feasible alternative means of obtaining numerical solutions. The pdf equations can be solved by either Eulerian or Lagrangian methods. The present study adopts the Lagrangian approach.

Chapter 2

Literature Survey

2.1 Mixing Layer Experiments

The fundamentals of plane mixing layers have been the subject of extensive theoretical and experimental investigations due to their apparent simplicity, common technological occurrences, and significant importance in mixing processes, often combined with chemical reactions and combustion. The plane mixing layer is representative of the mixing and reaction zones that exist in real combustion devices. In spite of extensive experimental and theoretical studies, the understanding of mixing and chemical reactions in these flows is incomplete, as evidenced by the discrepancies between experimental observations and predictions from current turbulent reacting flow models.

Konrad (1976) studied experimentally the extent of mixing in a mixing layer between two streams of fluid with equal density and a velocity ratio of 0.3. Nitrogen was used as the high speed gas and a mixture of argon and helium having the same density as nitrogen was used as the low velocity gas. He reported results for Reynolds numbers which were lower and higher than the Reynolds number (Re) corresponding to the mixing transition. The

results showed that the mixing process is strongly affected by the Reynolds number. In a mixing layer, the mixing transition is a region where the small scales are generated. The amount of mixing is found to be small at Re below the mixing transition Re, and the mixing increases drastically for Re higher than the mixing transition Re. The probability density function (p.d.f.) , also denoted as pdf and PDF in this text, showed the same values for the most probable concentration across the mixing layer.

Batt (1977) investigated experimentally the mixing of passive scalars and chemically reacting species in a gaseous mixing layer (jet) flow. The p.d.f. data showed peaks of preferred (most probable) concentration, with marching behavior across the mixing layer. The p.d.f.s have been observed to fall into two classes: marching p.d.f.s, in which the most probable value of the scalar varies across the layer, with the most probable value on each side of the layer being closer to the free stream value of that side, and non-marching p.d.f.s, in which the most probable value of the scalar is substantially independent of the position in the layer (Rogers and Moser 1994). The results of Batt (1977) also showed a nearly Gaussian distribution for the p.d.f. for the middle 50% of the mixing layer, i.e., around the centerline region. On the other hand, a deviation from the Gaussian shape was evident near the lateral edges of the layer. The r.m.s. of the passive scalars (concentration and temperature) showed a bimodal behavior, i.e., a dip in the r.m.s. profile.

Masutani & Bowmann (1986) examined the structure of a chemically reacting, gas phase, two stream plane mixing layer. They also conducted non-reacting flow experiments to establish the entrainment and mixing characteristics of the layer. This investigation provides information on the concentration structure and data on a pre-mixing transition

mixing layer, under both non-reacting and reacting flow conditions. Observations were made of the probability density functions (p.d.f.s) and associated statistical quantities of the conserved and reactive scalars. Based on their experimental data, Masutani & Bowmann (1986) have suggested that fluid in the mixing layer exists in three states: tongues of unmixed free-stream fluid which on occasion stretch across the layer, finite thickness interfacial diffusion zones of mixed fluid which border the parcels of unmixed fluid, and regions comprising fluid of nearly homogeneous composition. The results of this experiment also confirm previously reported asymmetry in the entrainment rates from the two feed streams. This study indicates that, for the conditions of this experiment, the layer entrains and subsequently mixes high speed fluid at approximately twice the rate of low speed fluid.

Lucht et al. (2001) realizing the inability of most passive scalar measurement techniques to resolve the smallest mixing scales, present resolution independent measurements of molecular mixing in a fully developed gaseous planar mixing layer. In their experimental work, the probability density functions (p.d.f.) of low and high speed fluid revealed new details regarding the entrainment process. Pure fluid from the low speed free stream was not typically transported across the entire width of the mixing layer, as shown by the p.d.f.s. By contrast, the p.d.f.s of high speed fluid showed marching behaviour on the low speed side, with significant regions of mixing layer at a preferred high speed fluid mixture fraction. Lucht et al. (2001) also emphasize the fact shown by a number of studies, that certain initial conditions, such as velocity ratio, initial turbulence level, initial momentum thickness, shredding frequency, splitter plate thickness (i.e. wake effects), and artificial forcing can have significant effects on shear layer mixing and development. This makes it

difficult to compare the results from various experimental and numerical investigations.

2.2 Mixing Layer Simulations

2.2.1 Vortex Methods

There has been an increased effort to simulate two-dimensional turbulent mixing layer flow using the vortex method. Works by Ashurst (1979), Leonard (1980), Inoue (1985), Ng and Ghoneim (1985), Ghoneim and Ng (1986), Lin and Pratt (1987), Milane and Nourazar (1995) and Abdolhosseini and Milane (1998) are among the numerous numerical simulations of two dimensional mixing layers that utilize the vortex method. A detailed review of mixing layer simulations is given by Ho and Huerre (1984). Ashurst (1979) used blobs and the random walk technique (Chorin, 1973) to simulate the mixing layer and concluded that the roll-up of a pair of lumps is the primary growth mechanism of mixing layers and is responsible for the entrainment of the surrounding non-turbulent fluid. His first calculation with constant core radius blobs at a low Reynolds number gave a Reynolds shear stress twice the experimental value, while r.m.s. longitudinal and lateral velocity fluctuations were in good agreement with the experiment. By including the use of an exponentially spreading blob, he obtained results consistent with the experiment. Inoue (1985) attributed the entrainment of the non-turbulent fluid into the mixing layer region partly to the vortex pairing and mostly to the vertical velocity induced by the Biot-Savart law.

Aref and Siggia (1980) simulated a temporally growing mixing layer in which the velocities of the flows above and below the splitter plate are in opposite directions. They

calculated the roll-up of a two-dimensional mixing layer using the vortex-in-cell method. The results for the r.m.s. longitudinal and Reynolds shear stress were in agreement with the experiment, whereas the r.m.s. lateral velocity fluctuations indicated much larger values than the experimental results. Aref and Siggia attributed this discrepancy to the effect of viscosity and vortex stretching, which is due to the non-negligible effect of three-dimensionality. Inoue (1985) reasoned that the disagreement between Aref and Siggia's results and the experimental observations is due to the use of fourth order integral scheme rather than the attributed effects. In his work, Inoue (1985) used a first order Euler scheme for time integration with larger time steps. His results showed that the r.m.s. lateral fluctuations are smaller than the r.m.s. longitudinal fluctuations which was in reasonably good agreement with the experiments.

The effect of forcing on the structure of mixing layers has also been studied. Inoue (1985) and Ng and Ghoneim (1985) simulated unforced layers, while Inoue and Leonard (1987) and Ghoneim and Ng (1986) reported the effect of harmonic forcing on the formation of large structures in mixing layers. Their results for the forced mixing layer were in excellent agreement with experiment, while the r.m.s. lateral velocity fluctuations for unforced mixing layer simulation was twice the experimental values. They concluded that the differences between the experimental and numerical results were mainly due to the neglect of the effect of the third dimension in calculations. Since forcing has a suppressing effect on the third dimension, a forced mixing layer can be considered a two-dimensional flow, but the unforced mixing layer is three-dimensional (Oster and Wygnansky, 1982).

Mansour (1985) used a two-dimensional hybrid scheme for a spatially growing

mixing layer. He divided the computational domain into two regions and solved the vorticity equation by different methods. He applied a two-dimensional vortex-in-cell method in the upstream region immediately after the splitter plate where the turbulent eddies are small relative to the size of grids and an Eulerian method (finite difference) in the downstream region where the eddies are larger than the grids. His results showed that the r.m.s. longitudinal velocity fluctuations were over-predicted, whereas the r.m.s. lateral velocity fluctuations were about the same as the experimental values. In two-dimensional simulations, the r.m.s. lateral velocity component is expected to be greater than the experimental results, because the energy transfer from the streamwise component is only to the cross-stream component. Kuwahara and Takami (1983) investigated the amalgamation of two eddies by using first order and fourth order schemes for the time integration. They concluded that for the first order scheme, there is a built-in eddy-viscosity modeling due to the larger numerical errors. They also concluded that introducing more viscosity has a suppressing effect on the roll-up and vortex pairing processes. In addition, results of Nakamura et al. (1982) showed that the effective viscosity for first order Euler scheme with small time steps is the same as fourth order Runge-Kutta with the larger time steps.

2.2.2 Probability Density Function of Scalar

The probability density function (pdf) method has been widely used to solve turbulent flows for over five decades (Hawthorne (1949) and Lockwood et al. (1975)). Lundgren (1969) derived, modeled, and solved a transport equation for the joint pdf of velocity, in which

convective transport appears in closed form. This is in contrast with the momentum equation in which, the convective terms have been solved using classical mean flow closure models or Reynolds stress closure models. In mean flow closures the Reynolds stresses transporting momentum need to be modeled (Launder and Spalding 1972), and in Reynolds-stresses closures the triple velocity correlations transporting the Reynolds stresses need to be modeled (Lumley 1978). But in the velocity pdf equation these processes do not have to be modeled and so the gradient diffusion assumption is avoided. Pope (1976) derived, modeled, and solved the transport equation for the composition joint pdf, that is, the joint pdf of a set of scalars. The standard k-ϵ turbulence model is used to determine the mean velocity and turbulence fields. The mean velocity, turbulent diffusivity and frequency are then used as inputs to the modeled transport equation, which is solved using the Monte-Carlo technique. The turbulent transport is modeled by gradient diffusion.

Kollmann and Janicka (1982) simulated a two-dimensional gaseous mixing layer flow using a classical two equation turbulence model. The results of the pdf showed good agreement with the experiment of Batt (1977) mentioned in section 2.1. The calculated pdf of Kollmann and Janicka (1982) showed peaks of preferred concentration, with marching behavior across the mixing layer.

Lin and Pratt (1987) used Monte-Carlo technique to solve the time dependent conservation equation for the pdf of a scalar in conjunction with a sub-grid scale vorticity model. The pdf did not show any preferred concentration across the mixing layer. Their results for statistical quantities such as the mean velocity, the growth rate, the r.m.s. velocity fluctuations and the Reynolds shear stress are quantitatively in agreement with experiments,

except for the r.m.s. lateral velocity fluctuations which were over-predicted. The discrepancies between their results and experimental values were attributed mainly to the non-negligible three-dimensionality effect. Lin and Pratt (1987) estimated the mixing frequency in Curl's coalescence/dispersion model by using Broadwell and Breidenthal's (1982) theory of micromixing, which involves Schmidt number. The results of Lin and Pratt's (1987) study found that the mean concentrations were insensitive to Schmidt number, whereas the concentration fluctuations for the higher Schmidt number fluid (liquid) were greater than those in the lower Schmidt number (gas).

Sandham and Reynolds (1989) used a DNS approach to simulate a two-dimensional mixing layer at low Reynolds number. They investigated the effect of the wake shed from the splitter plate on the development of a forced mixing layer, and suggest that the splitter plate wake effect is the most probable cause for the large initial asymmetry of entrainment, which has also been observed experimentally by Masutani and Bowmann (1986). The results for the pdf showed a preferred concentration across the mixing layer with non-marching behavior.

Vanormelingen and Bulck (1999) simulated an inert plane mixing layer for predicting the scalar transport. The free stream velocities correspond to Batt's (1977) experiment for a jet inlet. They applied finite volume procedures to obtain the velocity field, with the k-ϵ closure used to describe the turbulent transport. The scalar field is represented through the modeled evolution equation for the scalar pdf and is solved using a Monte-Carlo simulation. This study found that the bimodal shape of the root-mean-square (r.m.s.) scalar fluctuations can be numerically reproduced only by Monte-Carlo pdf method using a micro-mixing

model, whereas standard gradient diffusion calculations do not predict this effect. Vanormelingen and Bulck (1999) found that the pdf shape of passive scalar were best predicted by using the Least Mean Square Estimation (LMSE) mixing model. The results were compared with the experiment of Batt (1977). The study also links the bimodal behaviour to existence of non-u variations of mixing frequency with lateral distance.

Bilger (2000) in his review of progress in turbulent combustion outlines the issues of current interest and makes forecasts on approaches that are likely to lead to significant advances. Modeling approaches such as Conditional Moment Closure and Monte-Carlo Simulation of the transport equation for the probability density function are said to be enjoying considerable success and have the most promise for pollutant prediction in non-premixed systems, and also in partially premixed systems. For swirling flows and non-stationary premixed systems, Large Eddy Simulation is predicted to be the best choice in near future.

2.3 Objectives

The objective of this thesis is to apply the transport equation for probability density function (pdf) of a scalar in conjunction with the vortex-in-cell (VIC) to predict the passive scalar field in a two-dimensional spatially growing mixing layer. The vortex-in-cell (VIC) method, along with the computer code was developed and validated by Abdolhosseini (2000). For the present study, some additions have been made in the VIC code to compute eddy diffusivity and mixing frequency. The scalar pdf approach used in conjunction with

the k-ϵ turbulence model to determine the mean velocity, turbulence characteristics, and the scalar field, is a Reynolds Averaged Navier-Stokes (RANS) approach (Pope 1985). By contrast, when the k-ϵ turbulence model is replaced by the VIC, which is essentially a DNS approach, the prediction of the scalar field may be improved because the instantaneous velocity field is predicted rather than the average quantities pertaining to the velocity field. Specifically, in the present work the mean velocity, Reynolds stresses, turbulent diffusivity and mixing frequency will be computed by the vortex-in-cell method (DNS approach). These quantities will then be used as inputs to the transport equation for the pdf of a passive scalar, which is solved by the Monte Carlo technique (Lagrangian approach). In the pdf equation the turbulent transport term will be split into turbulent diffusion and convection due to turbulent diffusion. The convection due to turbulent diffusion is governed by the gradient of the eddy diffusivity. The gradient transport will be used to model the turbulent diffusion, wherein the eddy diffusivity will be computed using the Boussinesq's postulate and related to the scalar diffusivity using the turbulent Schmidt number. The molecular mixing term will be closed by a modified Curl model, and the convection term will use the mean velocity from the VIC solution.

The computational results will be compared with two-dimensional experimental results of Masutani and Bowmann (1986) because the two-dimensionality of the flow was carefully maintained and verified, but keeping in mind the fact that comparisons between experiments and computational results are difficult because of the high sensitivity of the mixing layer to initial conditions and free stream turbulence phenomenon. To counter the

influence of these effects, inflow boundary conditions are used in the present numerical simulation. Comparison is made with experimental data, for the predicted turbulent flow, such as, mean velocity, r.m.s. longitudinal fluctuation, momentum thickness, and for the mixing statistics of the passive scalar, in the simulations' region of similarity. Observation will be made of any asymmetry in root-mean-square (r.m.s.) scalar fluctuations, and how the scalar mixing region extends into the free stream compared to the momentum mixing region. The pdf shapes of the passive scalar will be looked at to evaluate entrainment behaviour, and any bias in favour of high-speed fluid. The effect of Schmidt number, mixing models, and variation of mixing frequency will also investigated.

Chapter 3

Formulations and Numerical Schemes (VIC)

3.1 Vorticity equation and Two-Dimensional Formulation

A mixing layer contains rotational flow with high levels of fluctuating vorticity. Therefore, vorticity is one of the main features that characterizes the level of turbulence in such flows. In performing numerical computation of viscous and incompressible flow by vortex methods, the governing equation solved is the vorticity transport equation.

The vorticity transport equation for an incompressible and viscous fluid flow is,

$$\frac{\partial \omega_i}{\partial t} + u_j \frac{\partial \omega_i}{\partial x_j} = \omega_j \frac{\partial u_i}{\partial x_j} + \nu \frac{\partial^2 \omega_i}{\partial x_j \partial x_j} \tag{3.1}$$

where ω_i represents the components of the vorticity vector ω, u_i and u_j represent the components of the velocity vector $\mathbf{u}$, and ν is the kinematic viscosity. The left-hand side of equation (3.1) includes the rate of change of vorticity in time and due to convection, respectively. The first term on the right-hand-side (R.H.S.) of the equation is the vortex stretching term, and the second term on the R.H.S. is the viscous diffusion.

The stretching term vanishes in two-dimensional cases, because the vorticity vector

ω is perpendicular to the gradient of **u**. Thus, the vorticity transport equation reduces to

$$\frac{\partial \omega_i}{\partial t} + u_j \frac{\partial \omega_i}{\partial x_j} = \nu \frac{\partial^2 \omega_i}{\partial x_j \partial x_j} \tag{3.2}$$

Assuming a flow parallel to the xy-plane, i.e. the velocity vector **u**=**u**(x,y,t), the vorticity vector reduces to one component in the z-direction perpendicular to the xy-plane (the plane of the motion),

$$\omega_z = \frac{\partial v}{\partial x} - \frac{\partial u}{\partial y} \tag{3.3}$$

where u and v are respectively the x and y components of the velocity. Since the divergence of the velocity is zero because of the continuity equation,

$$\frac{\partial u}{\partial x} + \frac{\partial v}{\partial y} = 0 \tag{3.4}$$

the components of the velocity **u** can be expressed as the gradients of a scalar, i.e. gradients of the stream-function ψ,

$$u = \frac{\partial \psi}{\partial y}, \qquad v = -\frac{\partial \psi}{\partial x} \tag{3.5}$$

Combining equations(3.3) and (3.5), Poisson's equation is obtained as

$$\nabla^2 \psi = -\omega_z \tag{3.6}$$

Equations (3.5) and (3.6) can be used to determine the velocity field knowing the vorticity field ω_z.

In the vortex method, equation (3.2) is split in two fractional steps:

$$\frac{\partial \omega_z}{\partial t} + u\frac{\partial \omega_z}{\partial x} + v\frac{\partial \omega_z}{\partial y} = 0 \tag{3.7}$$

$$\frac{\partial \omega_z}{\partial t} = \nu \left(\frac{\partial^2 \omega_z}{\partial x^2} + \frac{\partial^2 \omega_z}{\partial y^2}\right) \tag{3.8}$$

The first fractional step in eq. (3.7) describes the interaction of the vortices. The second fractional step in eq. (3.8) handles the diffusion of vorticity. The solution of equation (3.7) is equivalent to solution of the Poisson equation (3.6) together with the Lagrangian movement of the vortices described by the VIC method. The essence of applying the fractional step in the vorticity transport equation is that in one fractional step the flow is considered inviscid, so that the theorem of conservation of vorticity and circulation can be applied. Using the second fractional step, the viscosity effect is handled. This technique is well suited for slightly viscous flows.

3.2 Vortex-In-Cell Method

The method has been developed and described together with the computer code, in

Abdolhosseini (2000), and a brief description is given here. The VIC method is a mixed Eulerian-Lagrangian approach, with vorticity moved back and forth between point vortices moving with the flow and nodes of a fixed grid. The vorticity field is discretized into N point vortices, such that the total circulation of the field is given as,

$$\sum_{n=1}^{N} \Gamma_n = \int_A \omega \, dA \tag{3.9}$$

where Γ_n is the circulation of the vortex element n, and A the areas shown in figure (3.1a). The circulation Γ_n is the same for all vortices and will be denoted by Γ, as given in section (3.3). The vorticity from the point vortex (i.e., the Lagrangian element) is distributed to the four neighbouring nodes surrounding each vortex using the area-weighting scheme (Baker, 1979) as,

$$\omega_{i,j} = (\Delta x - dx)(\Delta y - dy)\Gamma_n / (\Delta x \Delta y)^2 = A_1 / A^2 \Gamma_n \tag{3.10-a}$$

$$\omega_{i+1,j} = dx(\Delta y - dy)\Gamma_n / (\Delta x \Delta y)^2 = A_2 / A^2 \Gamma_n \tag{3.10-b}$$

$$\omega_{i,j+1} = (\Delta x - dx)dy\Gamma_n / (\Delta x \Delta y)^2 = A_3 / A^2 \Gamma_n \tag{3.10-c}$$

$$\omega_{i+1,j+1} = dxdy\Gamma_n / (\Delta x \Delta y)^2 = A_4 / A^2 \Gamma_n \tag{3.10-d}$$

where dx and dy are as shown in figure (3.1a), Δx and Δy are the grid sizes.. The total vorticity at each nodal point is obtained by summing the contributions of all the surrounding vortices. Then the Poisson equation (3.6) is solved in order to obtain the streamfunction $\psi(i,j)$ at each node (i,j) of the computational domain (figure 3.1b) using the extrapolated

Liebmann's method (Chow, 1979). The components of the velocity at the nodes are then determined using a central difference scheme as

$$u(i,j) = \{\psi(i,j+1) - \psi(i,j-1)\} / 2\Delta y \tag{3.11a}$$

$$v(i,j) = -\{\psi(i+1,j) - \psi(i-1,j)\} / 2\Delta x \tag{3.11b}$$

The point vortices are connected using the velocity $\boldsymbol{u}_n=(u_n, v_n)$ acting on the n^{th} vortex, calculated using the velocities of the neighbouring nodes employing a bilinear interpolation (Baker, 1979) as:

$$u_n = \left(\sum_{k=1}^{4} u(k)\, A_k\right) / \Delta x \Delta y \tag{3.12a}$$

$$v_n = \left(\sum_{k=1}^{4} v(k)\, A_k\right) / \Delta x \Delta y \tag{3.12b}$$

The notation of Figure 3.1a has been used in eqs. (3.12a) and (3.12b), where k = 1,2,3,4 and $u(k)$ and $v(k)$ are components of the velocity at the nodes. In the first fractional step the position $\chi=(x_n,y_n)$ of the n^{th} vortex is calculated by integrating,

$$d\chi/dt = \boldsymbol{u}_n(\chi(x,y,t)) \tag{3.13}$$

using a first-order Euler scheme to yield,

$$x_n(t+\Delta t) = x_n(t) + u_n \Delta t \tag{3.14a}$$

$$y_n(t+\Delta t) = y_n(t) + v_n \Delta t \tag{3.14b}$$

where Δt is the time-step, and x_n and y_n are the coordinates of the nth vortex.

For the second fractional step in eq. (3.8), the effect of diffusion is simulated using the random walk method (Chorin, 1979). This is handled by superimposing the random walk on the motion due to convection of the vortices from the first fractional step:

$$x_n(t+\Delta t)=x_n(t)+u_n \Delta t+\eta_1 \tag{3.15a}$$

$$y_n(t+\Delta t)=y_n(t)+v_n \Delta t+\eta_2 \tag{3.15b}$$

where, η_1 and η_2 are obtained from a Gaussian distribution with zero mean and standard deviation $(2\nu\Delta t)^{1/2}$. The above-mentioned interpolation and area-weighting schemes are applied back and forth between the Lagrangian particles and the Eulerian mesh system. It is noted that in Eulerian techniques, such as finite difference and finite element methods, computation is affordable but numerical dissipation is inherent. Lagrangian techniques such as vortex methods (Sarpkaya, 1994), are immune from numerical dissipation but they are computationally expensive. The mixed Lagrangian-Eulerian vortex-in-cell (VIC) method, combines the best features of Lagrangian and Eulerian methods, i.e. the numerical dissipation is reduced relative to the purely Eulerian method, and the computational time is reduced relative to the Lagrangian method.

3.3 Boundary and Initial Conditions

The computational domain in figure (3.1b) consists of a uniform rectangular grid with grid sizes $\Delta x=\Delta y=\Delta$. The lower left corner of the grid system is located at $x=1$ and $y=1$. The Neumann conditions apply to the inflow and outflow boundaries. The inflow and outflow boundary correspond to a hyperbolic tangent velocity profile (Monkewitz and Huerre 1982) as,

$$(\partial\psi/\partial y)_{N,j} = (\Delta U/2)\ tanh\ \{2(y-y_{ov})/\delta_w\} + U_c \qquad (3.16)$$

where subscript j corresponds to the grid in the y-direction, U_H and U_L are the velocities of the high-speed side and the low-speed side respectively, $\Delta U=U_H - U_L$ is the velocity difference across the layer, $U_c=(U_H+U_L)/2$ is the average velocity, y_{ov} is the y coordinate of the centre of the profile, and $\psi=0$ at $y=0$. The vorticity thickness δ_w, defined in eq. (3.20), is based on the maximum slope of streamwise mean velocity and is a measure of the spread of the mean velocity. The following expression for vorticity thickness has been deduced from the mixing layers experiments.

$$\delta_w = 0.181\,(x-x_v)\,\Delta U/U_c \qquad (3.17)$$

where x_v is the virtual origin. The hyperbolic tangent profile has been used in the inviscid linear stability of 2D mixing. However, experimental measurements indicate that the mean velocity profile is closer to an error function, so an error function could also be used for the

inflow boundary condition. The effect of using a convection outflow condition will be discussed in section 5.1.2. Slip conditions are assumed for the top and bottom boundaries. The Dirichlet condition is used for the bottom boundary at $y=1$, consistent with $\psi_{i,0}=0$ at $y=0$, as

$$\psi_{i,1} = y_L \times U_L \tag{3.18}$$

where y_L =1 and for the top boundary

$$\psi_{i,N} = U_L y_{sp} + U_H(y_{i,N} - y_{sp}) \tag{3.19}$$

Initially, the velocity discontinuity across the splitter plate is simulated using a vortex sheet, discretized into a row of point vortices as shown in figure 3.1b. At time $t=0$, the point vortices are equidistant, and separated by a distance d = H/N, where N is the number of vortices and H is the computational domain length. The vortex closest to the edge of the splitter plate is moved vertically a small distance $0.5d$ to initialize the Helmholtz instability. The total circulation in the computational domain is $H(U_H - U_L)$. The circulation is equally distributed among the N vortices as $\Gamma = H(U_H - U_L)/N = d(U_H - U_L)$. Then the vorticity at the nodes is calculated using the area-weighting scheme (Baker, 1979) as discussed in section (3.2). In this scheme the vorticity of each vortex, calculated as $\Gamma/(\Delta x \Delta y)$, is assumed to be uniformly distributed within the grid that surrounds the vortex element. Typically, several vortices are in one cell at a given time, especially in the region of the mixing layer at the level of the splitter plate. Diffusion effects, i.e. the second fractional step, may be simulated either by random walk motion (Chorin, 1973) or by modifying the circulation of the point vortices keeping their location fixed (Sarpkaya, 1994). The former

approach has been adopted in this study.

Initially, the vorticity is nil at all nodes, except for the nodes that are at the level of the splitter plate. Furthermore, if at the end of each time step Δt, defined as the characteristic time $\Delta t = d/U_c$, a vortex with circulation Γ is introduced at the trailing edge of the splitter plate, the vorticity generation rate is $\Gamma/\Delta t = (U_H - U_L)/U_c$ and therefore the Kutta condition is satisfied. The oldest vortex (i.e. the largest residence time) is discarded from the calculations when a new vortex is introduced at the edge of the splitter plate. The time step is $\Delta t = d/U_c$, and the strength of vortices does not decay with time. Therefore, by keeping the total number and strength of vortices constant throughout the simulation, the conservation of circulation and vorticity is satisfied. Furthermore, the vortices can move freely in and out through the outflow boundary to avoid the collection of vortices at the end of the computational domain, and their effect is disregarded when they are outside the domain.

3.4 Solution Procedure

The solution procedure consists of the following steps:

a. Initializing by equidistant vortices at the level of the splitter plate, and by assuming initial values for ψ at at internal nodes together with the boundary conditions in eq. 3.17 to 3.19.

b. Distributing the vorticity to the four neighbouring nodes using the area-weighting scheme.

c. Solving Poisson's equation for ψ, using Gauss-Seidel iteration, with left-to-right sweep of the grid points and bottom-to-top sweep of the lines. The iterations are conducted until the difference between consecutive values of ψ is less than 0.001%.

d. Computing the velocities u and v at the nodes using equation 3.5.

e. Calculating the velocities at the location of each vortex (u_n,v_n) using a bilinear interpolation given by eq. (3.12a and 3.12b).

f. Updating the coordinates of the vortices using eq. (3.15a and 3.15b).

g. Introducing a new vortex at the edge of the splitter plate, and discarding the oldest one.

h. Computing the vorticity thickness and eddy viscosity, as discussed in sections 3.5 and 3.6.

i. Marching in time by repeating the calculations from step b through g.

3.5 Vorticity Thickness

The vorticity thickness is computed as

$$\delta_\omega = \frac{\Delta U}{(\partial \overline{U}/\partial y)_{max}} \tag{3.20}$$

where $\Delta U = (U_H - U_L)$ is the velocity difference between fast U_H and slow U_L free streams, and $(\partial \overline{U}/\partial y)_{max}$ is the maximum lateral change of the mean velocity $\overline{U}$. The growth of the layer vorticity thickness $\delta_\omega' = d\delta_\omega/dx$ from the simulation is compared in the results section, with Brown & Roshko's (1974) empirical relation for vorticity thickness growth rate,

$$\delta_\omega' = 0.181\left(\frac{1-r}{1+r}\right) \tag{3.21}$$

where $r = U_L / U_H$ is the velocity ratio.

3.6 Eddy Viscosity

Eddy viscosity ν_T is computed using Boussinesq's postulate,

$$\nu_T = - \frac{\overline{u'v'}}{\partial \overline{U}/\partial y} \tag{3.22}$$

where $\overline{U}$ is the streamwise mean velocity, y is the cross-stream direction, and $-\overline{u'v'}$ is the Reynolds shear stress. The Reynolds shear stress is calculated as $\overline{(U-\overline{U})(V-\overline{V})}$, where U and V are the streamwise and cross-stream instantaneous velocities respectively, and $\overline{V}$ is the cross-stream mean velocity. The maximum value of ν_T can be validated by establishing a relation with vorticity thickness δ_w. Re-writing eq. (3.22) in terms of maximum values,

$$\nu_{T_{max}} = - \frac{(\overline{u'v'})_{max}}{(\partial \overline{U}/\partial y)_{max}} \tag{3.23}$$

and multiplying both sides of eq. (3.23) by ΔU^2 and rearranging,

$$\nu_{T_{max}} = \Delta U \frac{-(\overline{u'v'})_{max}}{\Delta U^2} \quad \frac{\Delta U}{(\partial \overline{U}/\partial y)_{max}} \tag{3.24}$$

Now ΔU is constant, and the maximum values of the cross-stream correlation $-(\overline{u'v'})_{max}$ normalized by ΔU^2 are constant because of similarity:

$$[-(\overline{u'v'})_{max} / \Delta U^2] \approx Constant \tag{3.25}$$

Equation (3.24) therefore can be written as

$$\nu_{T_{max}} = Constant \times \delta_w \tag{3.26}$$

or,

$$\nu_{T_{max}} \propto \delta_w \tag{3.27}$$

The relation between maximum eddy viscosity and the vorticity thickness is shown and discussed in the results section.

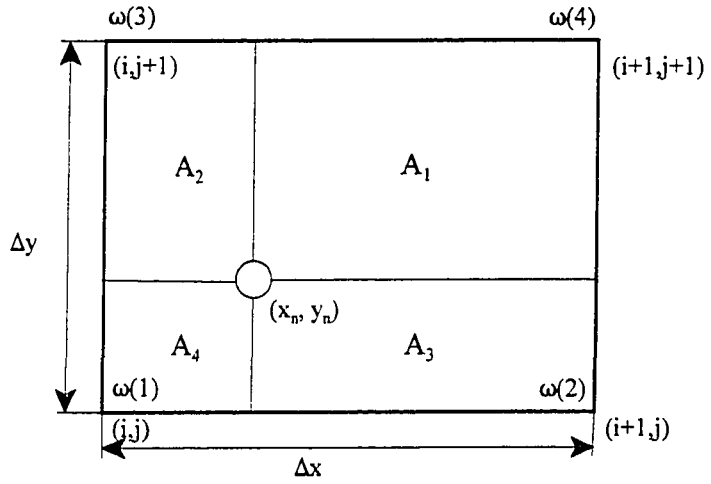

(a)

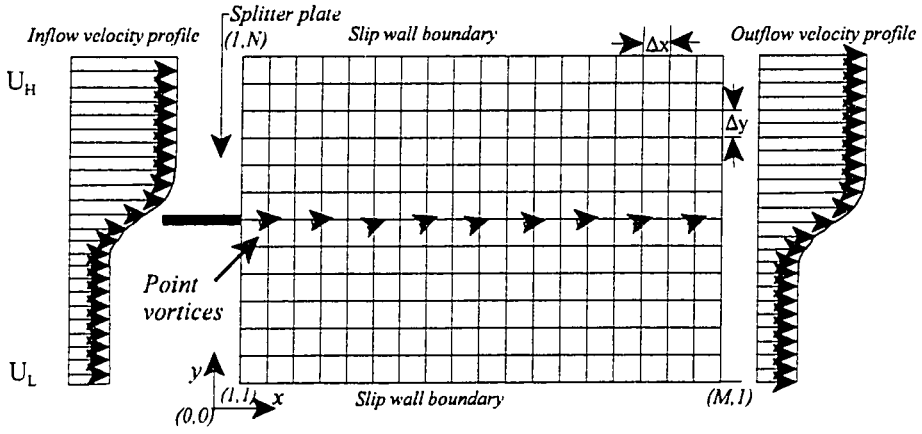

(b)

Figure 3.1 (a) Two dimensional area-weighting scheme in the VIC method. (b) Computational domain, rectangular grid, initial position of the vortices, and boundary conditions.

Chapter 4

Formulations and Numerical Schemes (PDF)

4.1 The Passive Scalar Joint pdf Transport Equation

The probability density function (pdf) is the relative frequency density of a realization over an ensemble. A transport equation can be derived for the pdf of a passive scalar, using the fine-grained pdf. The corresponding equation for the pdf of the mixture fraction ξ (Dopazo 1994, Pope 2000) is,

$$\frac{\partial P}{\partial t} + \frac{\partial(\overline{U}_j P)}{\partial X_j} + \frac{\partial}{\partial X_j}(<U_j'|\xi>P) = -\frac{\partial^2}{\partial \xi^2}(<D|\frac{\partial \xi}{\partial X_j}|^2|\xi>P) \qquad (4.1)$$

where, $\overline{U}_j$ and U_j' are the mean and velocity fluctuation respectively, t is time, X is the space variable, and D is the diffusivity. The symbol $<U_j'|\xi>$ indicates the expected value of U_j' conditional on the satisfaction of the constraint ξ . The mixture fraction ξ has been chosen as the conserved scalar and is defined as,

$$\xi = \frac{c - c_U}{c_L - c_U} \qquad (4.2)$$

where c is the concentration of passive scalar, and $c_U = 0$ and $c_L = 1$ are respectively the

concentrations of the upper and lower bounds of the variable ***c***.

The first term on the L.H.S. of eq. (4.1) is the transient term and the second is the convection term. The two are in closed form. The third term representing the turbulent transport is not closed, and the model is discussed in the following section (4.1.1). The first term on the R.H.S., the molecular dissipation or the molecular mixing term, is also not closed. The closure requires the joint statistics of ξ and its gradients, for which several models have been proposed [Dopazo (1994), Pope (2000)]. The two mixing models used to close the molecular mixing term are the Curl and modified Curl models. These models are discussed in sub-section (4.1.2).

4.1.1 Turbulent Transport Term

The closure of the turbulent transport term requires knowledge of the expected value of the velocity fluctuation conditioned to ξ. This term is only known when the joint statistics of U and ξ are known, i.e. when P is their joint pdf. In this study U is not included in P, and the turbulent transport term is modeled with the conventional gradient model,

$$\frac{\partial}{\partial X_j}(\langle U_j' | \xi \rangle P) = -\frac{\partial}{\partial X_j}(\nu_T \frac{\partial P}{\partial X_j}) \tag{4.3}$$

This term may also be viewed as

$$\frac{\partial}{\partial X_j}(\langle U_j' | \xi \rangle P) = -\nu_T \frac{\partial^2 P}{\partial X_j^2} - \frac{\partial \nu_T}{\partial X_j}\frac{\partial P}{\partial X_j} \tag{4.4}$$

In the two dimensional simulation the second of the two terms on the right hand side of eq. (4.4) is interpreted as convection with a velocity which has components $(-\frac{\partial \nu_T}{\partial x}, -\frac{\partial \nu_T}{\partial y})$, where x and y are stream-wise and cross-stream directions respectively.

The turbulent eddy diffusivity ν_T is related to diffusivity of the scalar γ_T as,

$$\gamma_T = \nu_T / S_{c_T} \tag{4.5}$$

where S_{c_T} is the turbulent Schmidt number. The turbulent eddy diffusivity ν_T is computed using Boussinesq's postulate,

$$\nu_T = - \frac{\overline{u'v'}}{\partial \overline{U}/\partial y} \tag{4.6}$$

where, y is the cross-stream direction. The Reynolds stress $- \overline{u'v'}$ and the streamwise mean velocity $\overline{U}$ are given by the vortex-in-cell solution of the mixing layer.

4.1.2 Molecular Mixing Models

Every molecular mixing model must satisfy several requirements during mixing (Pope 2000). A satisfactory model that fulfills these requirements has yet to be developed. In the particle implementation, i.e. the Monte-Carlo technique, the Curl and the modified Curl models satisfy the conservation of the mean values of scalar, the exponential decay in time of the scalar variance, and the boundedness condition upon mixing. The Curl mixing model, Curl

(1963), is based on an analogy between the mixing and break-up of parcels of fluids in a turbulent single-phase flow.

In the particle implementation, the pdf evolves by selecting randomly particles in pairs,

$$n_m = \beta\, \omega_f\, N\, \Delta t \tag{4.7}$$

Here n_m denotes number of pairs of particles that will mix, ω_f is the mixing frequency and coefficient β is a function of the mixing model. After mixing, the concentrations of the two particles in a mixing pair is given by, (see for example Craig and Milane 2000)

$$c_1^* = [(1-\alpha)c_1 + \frac{\alpha(c_1+c_2)}{2}] \tag{4.8a}$$

$$c_2^* = [(1-\alpha)c_2 + \frac{\alpha(c_1+c_2)}{2}] \tag{4.8b}$$

where c_1 and c_2 denotes the concentrations of the two particles before mixing, and c_1^* and c_2^* denotes the concentrations after mixing. The variable α is specified by a distribution function describing the mixing model. For the Curl model α=1 and β=2, Pope (2000). When employing the modified Curl model, β=3 and α is varied randomly between 0 and 1 according to the flat pdf, P(α)=1.

4.1.3 Mixing Frequency

Like most mixing models, the Curl and the modified Curl models require an externally supplied "scalar dissipation or mixing frequency". For a non-reactive flow the mixing frequency ω_f is related to the flow field as

$$\omega_f = C_\phi(\epsilon/k) \tag{4.9}$$

The ratio ϵ/k is the inverse of the turbulent integral time scale. Pope (1985) assigned a value of 2 for the constant C_ϕ . However, C_ϕ can vary from 0.6 to 3.1, depending on the flow geometry. Sensitivity of the results to C_ϕ is assessed in the results section. Furthermore, the proportionality constant C_ϕ in equation (4.9) relates the decay of the turbulent velocity fluctuations to the decay of concentration fluctuations, and hence, in a non-reactive flow the choice of the mixing frequency is related to the scalar field topology.

The turbulent kinetic energy k is obtained by,

$$k = \frac{1}{2}\left[(u'_{rms})^2 + (v'_{rms})^2\right] \tag{4.10}$$

where u'_{rms} and v'_{rms} are the root-mean-square values of the longitudinal and lateral velocity fluctuations. If the Reynolds number is very large, it is estimated that ϵ, the dissipation rate of k, is approximately equal to $\nu\Omega^2_{rms}$, where ν is the kinematic viscosity, (Tennekes and Lumley 1977), and Ω_{rms} is the root-mean-square of vorticity fluctuations. Considering the proportionality to $\epsilon \sim \Omega^2_{rms}$, the mixing frequency is computed as,

$$\omega_f = C_\phi \Omega^2_{rms} / \tfrac{1}{2}[(u'_{rms})^2 + (v'_{rms})^2] \qquad (4.11)$$

The parameters Ω_{rms}, u'_{rms}, v'_{rms}, come from VIC solution of the mixing layer.

4.2 Monte-Carlo Simulation

The passive scalar pdf transport equation (4.1) is solved using the Monte Carlo method. A finite-difference mesh is first generated for the computational domain. At each node, an ensemble of N particles is created. Each particle is identified by a representative value of the scalar concentration c. The particles in an ensemble are subjected to changes due to convection, turbulent transport, and molecular mixing. The turbulent transport term is split between turbulent diffusion, and convection due to turbulent diffusion (eq. 4.4). The four processes describe the four fractional steps by which eq. (4.1) is solved at each node, for each time step Δt. The first three processes involve particle exchange between two adjacent nodes, and the last involves mixing between pairs of particles at a node. The four fractional steps are summarized as follows:

Convection due to mean flow

The first fractional step is implemented by the Lagrangian displacement of n_c particles within the computational domain between the neighbouring nodes with,

$$n_{cx} = \Delta t \frac{|\overline{U}|}{\Delta x} N \qquad \text{and} \qquad n_{cy\pm} = \Delta t \frac{|\overline{V}|}{\Delta y} N \qquad (4.12)$$

in x and y directions respectively. Here $\overline{U}$ and $\overline{V}$ are respectively, the stream-wise and the cross-stream mean velocities, Δx and Δy are the respective grid sizes, and N is the total number of particles at each node. The particles are displaced in the direction of the velocity components.

Convection due to turbulent diffusion

The second fractional step is implemented by the Lagrangian displacement of n_t particles within the computational domain between the neighbouring nodes with,

$$n_{ctx\pm} = |\partial\gamma_T/\partial x| \frac{\Delta t}{\Delta x} N \qquad \text{and} \qquad n_{cty\pm} = |\partial\gamma_T/\partial y| \frac{\Delta t}{\Delta y} N \qquad (4.13)$$

in x and y directions respectively. The gradients of eddy diffusivity $-\partial\gamma_T/\partial x$ and $-\partial\gamma_T/\partial y$, are interpreted as velocity components in x and y directions, respectively. The particles are displaced in the direction of the velocity components.

Turbulent Diffusion

The third fractional step is implemented by the Lagrangian displacement of n_d particles within the computational domain between the four neighbouring nodes with,

$$n_{dx\pm} = \gamma_T \frac{\Delta t}{\Delta x^2} N \qquad \text{and} \qquad n_{dy\pm} = \gamma_T \frac{\Delta t}{\Delta y^2} N \qquad (4.14)$$

in x and y directions respectively, where γ_T is the eddy diffusivity at the node.

Mixing

The fourth fractional step is implemented by mixing pair of particles at each node. The

number of mixing pairs is given by,

$$n_m = \beta\ \omega_f\ N\ \Delta t \tag{4.15}$$

where n_m denotes the number of particle pairs, ω_f is the mixing frequency given by (eq. 4.11), and value of coefficient β is a function of the mixing model (see section 4.1.2).

At the end of the time step, the nodes are updated for the particle concentrations that were transferred by the three transport steps and the mixing step. The particles convected outside the computational domain are discarded, and an equal number of particles is replenished at the corresponding node of the opposing boundary. Particles exit the top, bottom, and the outflow domain boundaries by convection due to mean flow and by convection due to gradient of diffusivity. Particles do not diffuse out of the computational domain.

4.3 Computation of Probability Density Function

As mentioned in section (4.2), an ensemble of N particles is created at each node within the computational domain. Each particle is identified by a representative value of the concentration c. Now, the whole range of c (0 to 1) is sub-divided into W=100 intervals or windows, so that any one particle belongs in an interval based on its value of c.

The probability of finding a particle having concentration c within an interval $\psi_i \leq c \leq \psi_{i+1}$ is written as,

$$p(\psi)\ \Delta\psi_i = \frac{n_i}{N} \tag{4.16}$$

where n_i is the number of elements in the interval $\Delta\psi_i$. An ensemble is so created at a node that it represents the pdf at that point as N approaches infinity. With the Monte Carlo method simulating the changes of elements in an ensemble, the pdf is then obtained by eq. (4.16).

4.4 Time Criteria

Particles at a node are depleted by processes of stream-wise and cross-stream convection, and turbulent transport, described by the first three fractional steps. The resulting state at a node then undergoes mixing, described by the fourth fractional step. The number of particles that will deplete depends on the time step size Δt, the total number of particles N at a node at the beginning of the time step, and the fractional step considered. Therefore, the time step Δt may not be so large that a process removes more particles than there exist at the node or even completely deplete the node. On the other hand, an arbitrarily selected small Δt may lead to an unnecessarily long computation time. The criterion also ensures that the number of particles that mix will not be more than the total number that exist at the node. The time criteria applied to compute Δt are explained below. The time step size is derived from the equations for convection, diffusion, and mixing, described in section (4.2).

The number of particles convected is given by eq. (4.12). In order to have a number of convected particles n_c less than total number of particles N at the node, i.e. $n_c < N$, the conditions $\Delta t_c < \frac{\Delta x}{\overline{U}}$ and $\Delta t_c < \frac{\Delta y}{|\overline{V}|}$ must be met. The minimum of the two values is selected as Δt_c:

$$\Delta t_c < \min\left[\frac{\Delta x}{\overline{U}}, \frac{\Delta y}{|\overline{V}|}\right] \tag{4.17}$$

where Δx and Δy are the grid size, and $\overline{U}$ and $\overline{V}$ are stream-wise and cross-stream mean velocities, respectively.

Convection due to turbulent diffusion moves particles from a node in compliance with eq. (4.13). The condition $n_{ct} < N$ is obtained by ensuring that $\Delta t_{ct} < \frac{\Delta x^2}{|\partial \gamma_T / \partial x|}$ and $\Delta t_{ct} < \frac{\Delta y^2}{|\partial \gamma_T / \partial y|}$, i.e.,

$$\Delta t_{ct} < \min\left[\frac{\Delta x^2}{|\partial \gamma_T / \partial x|}, \frac{\Delta y^2}{|\partial \gamma_T / \partial y|}\right] \tag{4.18}$$

where gradients of eddy diffusivity $\partial \gamma_T / \partial x$ and $\partial \gamma_T / \partial y$, are interpreted as velocity components.

By turbulent diffusion, the particles move in four directions from a node, in compliance with eq. (4.14). In order to satisfy $n_d < N$, the conditions $\Delta t_d < \frac{\Delta x^2}{\gamma_T}$ and $\Delta t_d < \frac{\Delta y^2}{\gamma_T}$ must be assured. i.e.,

$$\Delta t_d < \min\left[\frac{\Delta x^2}{\gamma_T}, \frac{\Delta y^2}{\gamma_T}\right] \tag{4.19}$$

where, γ_T is the eddy diffusivity.

The number of particles that will mix is given by eq. (4.15). The number of mixing pairs n_m must be less than half the total number of particles at the node. Therefore, for $n_m < ½ N$ the condition

$$\Delta t_m < 1 / (2 \beta \omega_f) \tag{4.20}$$

must be satisfied. Here it is recalled that ω_f is mixing frequency given by eq. (4.11), and the value of coefficient β is a function of the mixing model (see section 4.1.2).

The minimum of the four values determines the time step size,

$$\Delta t = \min [\Delta t_c , \Delta t_{ct} , \Delta t_d , \Delta t_m] \tag{4.21}$$

Furthermore, the time-step Δt used in the calculations is divided by four, as a conservative estimate.

4.5 Boundary and Initial Conditions

The computational domain for the Monte Carlo simulation consists of a rectangular grid, with uniform grid sizes $\Delta x = \Delta y = \Delta$. The fast stream above the splitter plate has an initial concentration of $c_U = 0.0$, and the lower slow stream has an initial concentration of $c_L = 1.0$. A boundary condition at the inlet is described by a hyperbolic tangent concentration profile, in order to include the effects of the splitter plate. Similar to the inflow velocity profile in eq. (3.16), the inlet boundary condition for concentration is given by,

$$c(y)_{I,j} = (\Delta c/2) \tanh \{2(y-y_{oc}) / \delta_c\} + c_c \tag{4.22}$$

where subscript j corresponds to the grids in the y-direction, $\Delta c = c_L - c_U$ is the concentration difference across the layer, $c_c = (c_L + c_U)/2$ is the average concentration, and y_{oc} is the y

coordinate of the centre of the profile. Similar to the experimental expression for the vorticity thickness in eq. (3.17), the expression $\delta_c = 0.181\,(x - x_c)\,\Delta c/c_c$ is used for concentration, where x_c is the virtual origin. The outflow boundary condition is not specified because the displacement of concentration due to streamwise convection is very high, as compared to the displacement of concentration due to backward diffusion and gradient of diffusion. Therefore, the concentration values in the downstream flow do not have any effect upstream.

Concentrations are allowed to exit the top, bottom, and the outflow domain boundaries by convection due to mean flow and by convection due to the gradient of diffusivity. The domain is replenished at the corresponding nodes of the boundary opposing the boundary of the particle exit. At the inlet the replenished concentrations are defined by the inlet B.C., and at the top and bottom the concentrations assume the fast and slow free stream values of 0 and 1, respectively. Concentrations do not leave the domain by the third fractional step of diffusion. This is allowed, because there is no diffusion near the top and bottom boundaries. Also, streamwise displacement of concentration due to diffusion is negligible compared to displacement due to streamwise convection.

4.6 Solution Procedure

The solution procedure consists of the following steps:

a. Initialize the number of particles at each node in the computational domain.

b. Assign each particle the initial concentration. A value of 0 and 1 above and below the splitter plate respectively is used, together with the boundary condition (eq. 4.22).

c. Read-in the flow-field parameters given by the vortex-in-cell solution of the mixing layer.

d. Apply the time criteria (eq. 4.17 to 4.21) to compute the time step size Δt.

e. Displace the particles (concentrations) on random basis, using (eq. 4.12 to 4.14).

f. Update the nodes for the new state, i.e. the number of particles and associated concentrations.

g. At each node, carry out mixing using eq. (4.15), and update for post-mixing concentrations.

h. Allow the field to develop in the first 1000 time-steps. Between step 1000 and 4000, the mean concentration is computed. The r.m.s. of concentration, and unmixedness are then computed from step 4000 to 12000. The details are discussed in section 5.2.

i. March in time by repeating steps d to h, with step h performed only within the defined range of time steps.

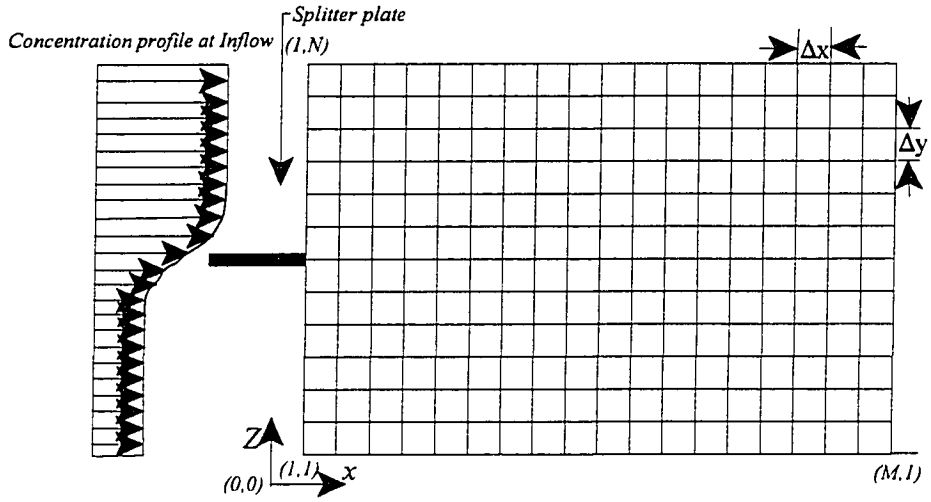

(a)

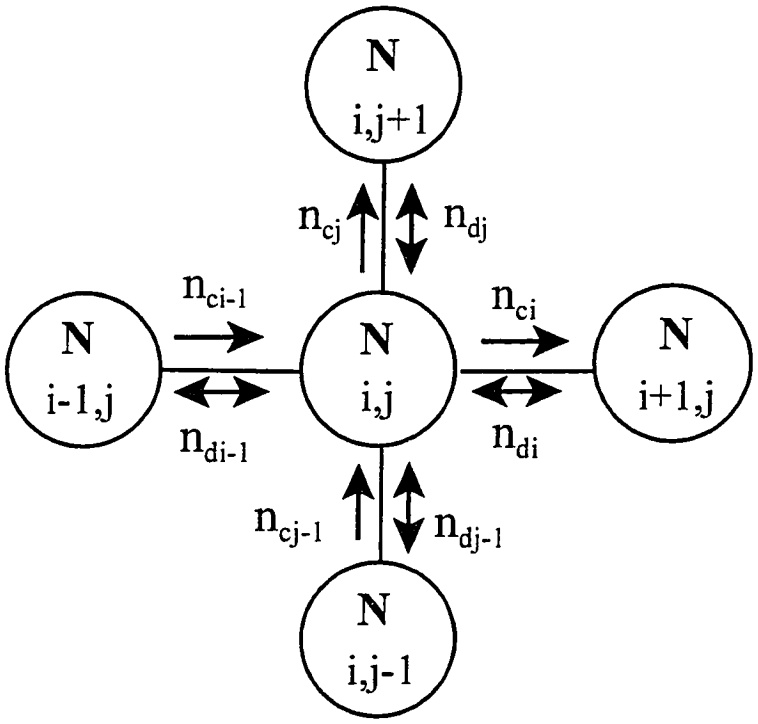

(b)

Figure 4.1: (a) Computational domain for Monte-Carlo,
(b) Monte-Carlo Simulation

Chapter 5

Results

The experimental mixing layer data published by Masutani & Bowmann (1986), also denoted by M&B in the text, is used to validate the computational results because the two-dimensionality of the flow was carefully maintained and verified. It is to be noted that comparisons between experiments and computational results are difficult because of the high sensitivity of the mixing layer to certain initial conditions such as initial turbulence level, shedding frequency, splitter plate thickness (i.e. wake effects), and other effects like free stream turbulence phenomena. To counter the influence of these effects, it is important to consider appropriate inflow boundary conditions in numerical simulation of mixing layers.

Masutani & Bowmann (1986) indicated that the growth of their layer was about 15-20% larger than the value measured by the majority of other experiments. This may be due to an acoustic field established within the experimental rig (acoustic forcing can enhance the growth of the shear layer by initiating early roll-up and pairing, Ng and Ghoneim (1987)). The effect of difference in the growth rates will appear in all comparisons; for example, the experimental velocity profiles are expected to spread into the free streams faster than the predicted profiles. Masutani & Bowmann (1986) have also stated that, while their flow cannot be considered to be fully developed, the mean velocity and concentration profiles

relaxed to equilibrium distributions and the mean characteristics of the layer stabilized by x=7.0 cm. The grid length for the experiment is not stated; however results are reported up to x=18cm. The mean velocity and concentration profiles for present simulation reach self-similarity by downstream location x=18 cm. for a computational domain length of 32 cm. The results of the numerical simulation are presented in the region of self-similarity, which is from x= 18 cm. to 24 cm., i.e. $0.56 \leq x/H \leq 0.75$. The result at x=13 cm., i.e. x/H=0.41, a location in the region of non-similarity is also reported. The results will be qualitatively compared with the Masutani & Bowmann (1986) experiment.

5.1 Flow Field and Numerical Parameters

Results reported in this work are for the simulation with a velocity ratio $r = U_L/U_H = 0.5$ (velocity ratio of the lower velocity side of the splitter plate to the higher velocity side). The uniform velocities used for the present simulation are U_H= 600 cm/s and U_L = 300 cm/s, similar to the parameters used in the experiment of Masutani and Bowmann (1986). Therefore, the velocity difference is $\Delta U = U_H - U_L = 300$ cm/s and the average velocity is U_c = 450 cm/s. The reported results are for a viscous flow condition with $\nu = 14.5 \times 10^{-2}$ cm^2/s (the kinematic viscosity of air at 18 °C). The centre of the hyperbolic tangent profile y_{ov}, discussed in section 3.3, is set as 16.99 cm. for inflow and as 16.95 cm. for outflow boundary conditions, respectively. The results for the mean velocity, the root-mean-square (r.m.s.) longitudinal and lateral velocity fluctuations, and Reynolds shear stress are obtained by averaging the unsteady solution over a period of time. The results for statistics are reported

at downstream locations, $0.41 \leq x/H \leq 0.75$, where H=32cm is the computational domain length of the simulation.

A base run using a 256×256 grid system with uniform grid size $\Delta x = \Delta y = 0.125$ cm. is chosen for this work. At the level of the splitter plate, the shear layer is discretized into a layer of M=19800 equidistant vortex elements. Therefore, the circulation of each vortex is $\Gamma = \Delta U.\, d = 4.85\times10^{-5}\ m^2/s$, where d is the initial spacing between the vortices. The time step used for the simulation is calculated as $\Delta t = d/U_{av}$, where $U_{av} = (U_H + U_L)/2$. Accordingly, for the simulation using 19800 vortex elements the time step is 3.59×10^{-6} sec. The simulation is run for 36 residence times, i.e 36M =712,800 time-steps. Turbulent characteristics are obtained by averaging the last 25M time-steps. The computational time of the present run using the VIC method is 28 hours on a DEC Alpha.

5.1.1 Streamwise mean velocity profile

The streamwise mean velocity normalized as $(U - U_L)/(U_H - U_L)$ is shown in Figure 5.1 as a function of the similarity variable η_v at four downstream locations, where U is the mean velocity, $\eta_v = (y-y_0)/(x-x_v)$, and y_0 is the ordinate of the velocity centerline. The agreement with the experiment of Masutani and Bowmann (1986) is adequate. However, the slower free stream is reached at $\eta_v = -0.06$ in the simulation, which is earlier than $\eta_v = -0.07$ for the experiment. Self-similar profiles are obtained for $0.56 \leq x/H \leq 0.75$. The velocity centerline, defined as the locus of locations with the average velocity U_c, is tilted toward the low-speed side. Its slope, obtained from a linear curve-fit of the streamwise centerline points, is equal

to -0.013. The virtual origin, defined as the x-location at the intersection of the velocity centerline with the horizontal line at the level of the splitter plate, is $x_v = 4.21$ cm., that is, 3.21 cm. from the edge of the splitter plate, in the coordinate system shown in Figure 3.1b.

5.1.2 Momentum Thickness

The time averaged momentum thickness θ is evaluated as,

$$\theta = \frac{\Sigma_{m=1}^{m=M} \int_{-\infty}^{\infty} \{(1/4)-((u-U_c)/\Delta U)^2\}\, dy}{M} \qquad (5.1)$$

where M is the number of time steps, and u is the instantaneous velocity (see e.g. Schlichting (1968) for details). Figures 5.2a and 5.2b show the momentum thickness θ and the streamwise momentum thickness growth rate $d\theta/dx$ respectively, as a function of x/H. Figure 5.2b shows the region of nearly linear growth between $0.25 < x/H < 0.65$, where the slope is equal to about 0.0162. This value of the slope is close to the experimental value 0.0165 of Masutani and Bowmann (1986), as deduced by Ghoniem et. al. (1990). Between $0.65 < x/H < 0.95$, the growth rate becomes faster. Then after $x/H > 0.95$, the growth rate decays and the momentum is adjusted by the experimentally prescribed outflow boundary condition.

Abdolhosseini and Milane (1998) investigated and found that the outflow boundary does not have any bearing on the momentum thickness development in the region of linear growth. They also compared the results obtained using the tanh outflow boundary condition in equation (3.16) with the ones obtained with the velocity profile based on Gortler's error

function as suggested by the experimental investigation of Spencer and Jones (1972). The results showed no significant difference. Abdolhosseini and Milane (1998) also conducted numerical experiments using a reflection boundary condition, i.e. a convection outlet condition, rather than specifying an outflow boundary condition for the stream-function. The authors found that the momentum thickness was not too different up to x/H ≈ 0.25 cm., after which the momentum thickness growth rate is faster when the reflection boundary condition is used. The tanh outflow boundary condition has been adopted in this study because it constrains the growth rate of the momentum thickness, and yields a slope for the linear growth region, i.e. $0.25 < x/H < 0.65$, in close agreement with the experiment. Therefore, it is concluded that the need to prescribe the outflow boundary condition when the VIC method is used, highly restricts the prediction of the general flows where an outflow boundary condition is not a priori known.

5.1.3 Reynolds Stresses

The r.m.s. longitudinal (r.m.s. u') and lateral (r.m.s. v') velocity fluctuations normalized with ΔU are shown in Figures 5.3a(i) and 5.3a(ii). Self-similar profiles are obtained for $0.56 \leq x/H \leq 0.75$. The Reynolds shear stress $(\overline{-u'v'})$ normalized with ΔU^2 is shown in Figure 5.3a(iii). The r.m.s.u' from simulation is shown against data from the Masutani and Bowmann (1986) experiment in Figure 5.3a(i). Opposite to the trend observed in the experimental data, the values for the r.m.s. u' in the simulation slightly increase along the streamwise direction. Similar behaviour is found in the numerical work of Ghoniem (1990), who explains that

velocity fluctuations should decrease at later stages of the mixing layer, as dissipation due to molecular diffusion becomes important. This anomaly may be investigated in detail in a future study. The data for r.m.s. v' and $(\overline{-u'v'})$ is not reported in the M&B experiment. The comparison for r.m.s. v' and $(\overline{-u'v'})$ is made in Figure 5.3b, with data from the experiment of Oster & Wygnanski (1982) conducted at velocity ratio of 0.6, which is slightly different than the value of 0.5 for the present simulation. The experiment of Oster & Wygnanski (1982) is also referred to as O&W in this text. The statistics in Figure 5.3b are given against $(y - y_0) / \theta$, as used by O&W for similarity. Here, y_0 is the ordinate of the velocity centerline and θ is the momentum thickness.

In the present study the simulation is run for 36 residence times, i.e 36M =712,800 time-steps, and turbulent characteristics obtained by averaging the last 25M time-steps. The Reynolds shear stress $(\overline{-u'v'})$ requires more time-steps, because it includes the contributions from pairs of clusters of vortices of various stages of rotation and amalgamation, as discussed in Aref and Siggia (1980). The negative cross-stream correlation $(\overline{-u'v'}/\Delta U^2)$ is believed to be well predicted, because it is linked to the mean flow by the mean momentum and the mean flow is in good agreement with the experiment, as indicated by Figure 5.1

5.1.4 Vorticity Thickness and Eddy Viscosity

Figure 5.4 shows the plot for the vorticity thickness. The growth rate of the layer vorticity thickness δ_ω', deduced from Figure 5.4, is about 0.062 for this simulation. This is less than

the value of $\delta_\omega' = 0.0706$ found by Masutani and Bowmann (1986), who have indicated that the growth rate of their layer was 15-20% larger than the value measured by the majority of other experiments. The vorticity thickness growth rate value from the simulation is closer to the value of $\delta_\omega' = 0.0603$ from Brown & Roshko's (1974) empirical relation (eq. 3.18). Figure 5.5 shows the plot for eddy viscosity ν_T as a function of the similarity variable η_v, at downstream locations $0.41 \leq x/H \leq 0.75$. The peak values of eddy viscosity ν_T increase with the downstream position, as shown in Figure 5.6. This is consistent with the discussion of eq. (3.27), which indicates that $\nu_{T_{max}} \propto \delta_w$, and with the fact that δ_ω grows in a nearly linear fashion as shown in Figure 5.4.

5.2 Scalar Field and Numerical Parameters

The base run for the scalar field utilizes a rectangular computational domain with a 256x64 grid, in the streamwise and cross-stream directions, respectively. A shorter domain is used in the cross-stream direction as compared to the flow field domain, to reduce the computational time. This did not present any discrepancy because the flow field develops well within the 64 grid points. The uniform grid size $\Delta x = \Delta y = 0.125$ cm. is the same as with the flow field. The total number of particles N at any grid point is initialized as 100. For each of the particles, the concentration is initialized at time t = 0.0 as c = 1.0 in the low speed stream and c = 0.0 in the upper high speed stream. The distribution of concentration immediately downstream of the splitter plate is described by the hyperbolic tangent profile in eq. (4.22). The centre of the hyperbolic tangent profile (y_{oc} in eq. (4.22)), is set as 16.9 cm.

The p.d.f. solution requires specifying the constants C_ϕ, S_{CT}, and the mixing model. The effect of the constants and the mixing models will be discussed in the following sections. For the base run, the modified Curl model is used with a value of the constant $C_\phi = 0.8$. The value of 0.8 is less than the $C_\phi = 2.0$ used by Pope (2000), but it falls within the range C_ϕ = 0.6 - 3.1 suggested by the experiments. The Turbulent Schmidt number used is $S_{CT} = 0.3$, which is lower than the typical value of 0.5 to 1.0 used in the literature. This is done to enhance diffusion (turbulent transport), and therefore provide a better fit to the experimental data. The base run did not include the convection due to turbulent diffusion given by eq. (4.13), because it resulted in a deterioration of the fit between the experimental data and the model, as will be shown in section 5.2.7.

To achieve statistically stationary solutions, the Monte Carlo simulation is run for 12000 time-steps. The results are allowed to develop in the first 1000 time-steps, then steps 1000 to 12000 are used to compute ensemble averages and statistics. Between step 1000 and 4000, the mean concentration is computed. Initial test runs computed the mean concentration beyond step 4000, and the results clearly showed that the mean values of concentration become stationary, i.e. stop changing by step 4000. The r.m.s. of concentration, and unmixedness are computed from step 4000 to 12000. The number of time steps to be run were decided as a conclusion of several tests, with the program run up to a maximum of 20000 steps. The results converged adequately by step 12000. The time step, $\Delta t = 5.2 \times 10^{-5}$, is governed by convection due to streamwise mean velocity given by eq. (4.12). The results for the base run are discussed in sections 5.2.1 to 5.2.4, whereas the effects of constants C_ϕ, S_{CT}, the mixing models, and constant mixing frequency are discussed in sections 5.2.5 to

5.2.8. The computational time of the base run is 26 hours on DEC Alpha.

5.2.1 Mean Concentration

The mean concentration $\bar{\xi}$ is shown in Figure 5.7, as a function of the similarity variable η_c,

$$\eta_c = (y - y_{oc}) / (x - x_c) \tag{5.2}$$

where y_{oc} is the concentration centerline location at any streamwise station, and x_c is the x-location of the virtual origin for concentration, found to be 7.15 cm. from the edge of the splitter plate. The mean concentration profiles appear to have achieved reasonable similarity when plotted against η_c downstream of x_c, and the agreement with the experiment is adequate. Figure 5.7 shows that the high speed free stream concentration, to the right of the concentration centerline $\eta_c = 0$, is reached later than the low speed free stream concentration. Taking for example, x-location 21 cm., the high speed concentration c = 0 is reached at about $\eta_c = 0.11$, whereas, the low speed concentration c = 1 is reached at about $\eta_c = -0.05$. This shows that the concentration values in the mixing layer are influenced more by the high speed fluid, and indicates that the layer entrains more of the high speed fluid. Comparison between the mean concentration profile and the mean velocity profile in Figure 5.8 shows that, the scalar mixing region extends further into the free stream than does the momentum mixing region, indicating enhanced transport of scalars over momentum. This fact is clarified further in section 5.2.4.

5.2.2 Root-Mean-Square Concentration

The root-mean-square (r.m.s.) of concentration ξ_{rms} plot against η_c at four downstream positions is shown in Figure 5.9. The r.m.s. profiles exhibit mixing asymmetry, with high speed fluid mixing at a faster rate than the low speed fluid. The lower r.m.s. on the high speed side of concentration centerline η_c=0.0 in Figure 5.9 is explained based on the variation of mixing frequency with lateral distance shown in Figures 5.10a and 5.10b. Whereas the mixing frequency shown in Figure 5.10b is symmetric about the velocity centerline η_v=0.0, it is asymmetric about the concentration centerline η_c=0.0, as shown in Figure 5.10a, with higher values on the high speed side. This simulation however, could not reproduce the bimodal behavior or the dip in the r.m.s. profile. The bimodal behavior is probably linked to diffusion. A test case with a small Schmidt number, S_{CT} = 0.05, was run to enhance turbulent diffusion $\gamma_T = \nu_T / S_{CT}$. The result in Figure 5.14 shows that the dip in the r.m.s. profile becomes evident; however, other parts of the results have deteriorated as will be discussed in section 5.2.5. The absence of a dip in the profile may be attributed to the modeling of the turbulent transport term in eq. (4.1) with the conventional gradient diffusion model, or to inappropriate inflow boundary conditions. One approach to improve the results would be to use instantaneous velocity fluctuations in the turbulent transport term, $\frac{\partial}{\partial X_j}(\langle U_j' | \xi \rangle P)$.

The r.m.s. of concentration of the simulation is also given against the experiment of Batt (1977). This experiment is conducted with slow stream inlet velocity of 1.6 ft/s (49 cm/s) and fast stream inlet (jet) velocities of 23 ft/s (701 cm/s) and 50 ft/s (1524 cm/s). The corresponding velocity ratios are approximately 0.07 and 0.03 respectively. Batt (1977)

defines the similarity variable as $\eta_c' = 12\,(y - y_{oc}) / (x - x_c)$, where 12 is a spreading factor. To make a reasonable comparison the data in Figure 5.9b, i.e., for the present simulation, M&B (1986), and Batt (1977), is presented against η_c'. Also, in the present simulation the positive y (lateral axis) direction is towards the high speed side, and therefore, positive η_c' values represent the high speed side. Batt (1977) present their data, taking positive y direction and therefore positive η_c' towards low speed side. In presenting Figure 5.9b, a reflection of Batt (1977) data is taken, so that positive η_c' represent high speed side for both the experiment of Batt (1977) and the present simulation. The r.m.s. concentration profile of Batt (1977) shows a higher spreading rate and much lower r.m.s. values compared to the simulation. Figure 5.9b also shows a bimodal trend in Batt (1977) data and an asymmetry with lower r.m.s. concentration values on the high speed side similar to the numerical study by Ghoniem & Heidarinejad (1990) and the experiment of Masutani & Bowmann (1986). These results confirm the existence of bimodal trend in the r.m.s. concentration profiles of mixing layer. The prediction of the data of the Batt (1977) experiment is left for future study.

5.2.3 Un-Mixedness

Non-reacting flow simulation is carried out to determine the mixing characteristics of the plane mixing layer. The established results may be used in interpretation of an isothermal reacting which is different than cold combustion. Therefore, it is important to know the degree of mixing that occurs in the layer. The root-mean-square value of concentration gives an estimate of the extent of mixing. However, a better measure is "un-mixedness" UM, or

segregation index (Lin and Pratt 1987), defined by,

$$UM = \frac{< c^2 >}{< c > (1 - < c >)} \tag{5.3}$$

where c and $< c >$ are respectively, the instantaneous and average concentrations at a node. These equations though, become ill-defined near the edges of the mixing layer. Konrad (1976) proposed a better definition as

$$UM = \frac{\int_{t1}(c - < c >)\, dt_1 + \int_{t2}(< c > - c)\, dt_2}{\int_{t1}(1 - < c >)\, dt_1 + \int_{t2} < c >\, dt_2} \tag{5.4}$$

where t_1 is the time when $c \geq < c >$, and t_2 is the time when $c < < c >$.

Figure 5.11 shows UM plotted against η_c at four downstream locations. A direct comparison with the Masutani and Bowmann (1987) experiment can not be made because UM has not been reported by them. The trend of the UM profile however, seems correct in comparison with the experiment of Konrad (1977), and the numerical simulation of Lin and Pratt (1987). As with the r.m.s. profile, the bimodal behavior or the dip does not appear. A possible reason for which, as explained in the previous section 5.2.2, is the use of the gradient diffusion hypothesis to model the turbulent transport term, or the inflow boundary condition.

Figure 5.11 indicates that the un-mixedness is large, which suggests that large scale turbulent eddies are present in the flow. This is consistent with the streaklines of point vortices given in Abdolhosseini and Milane (1998), where the large eddies appear in the

mixing layer development.

5.2.4 Spread of Concentration and Velocity

The mixing layer at each downstream location is characterized by the region between the velocity values of $1.05U_L$ and $0.95U_H$, where $U_L = 300$ cm/s is the lower slow free stream velocity and $U_H = 600$ cm/s is the upper fast stream velocity. Similarly, the scalar fractions (concentrations) are characterized by the region between values of 0.05 and 0.95. Note that the concentration values in the upper and lower free streams are 0.0 and 1.0 respectively. The above definition enables a convenient comparison between the spreads of velocity and concentration. Figure 5.12 shows a higher spread for concentration, i.e. the scalar mixing region extends further into the free stream than does the momentum mixing region, indicating enhanced transport of scalars over momentum. The spread of concentration plots also allow one to see any effects of varying parameters S_{CT}, C_ϕ, and mixing models on the scalar field, as will be shown in sections 5.2.5 to 5.2.7.

5.2.5 Effect of turbulent Schmidt number

The turbulent Schmidt number $S_{CT} = \nu_T/\gamma_T$, is inversely related to the scalar diffusivity γ_T. Numerous tests were performed to examine the effects of varying scalar diffusion by varying S_{CT}, with convection and mixing remaining constant. Figures 5.13 to 5.15 show the results of the tests with $S_{CT} = 0.7, 0.5, 0.3, 0.2, 0.05$. Figure 5.13 and 5.14 show that the results with

$S_{CT} = 0.2$ and 0.3 are in closer agreement with the experiment than the results with $S_{CT} = 0.5$ and 0.7. The values of 0.5 and 0.7 are reported because they have been used in previous literature. The mean concentration in Figure 5.13 shows that the scalar field for $S_{CT} = 0.2$ spreads further and reaches the fast stream at $\eta_c = 0.12$, whereas for $S_{CT} = 0.3$ the fast stream is reached at $\eta_c = 0.13$. Figure 5.15 confirms that as the diffusion is increased by reducing the S_{CT}, the concentrations spread further into the free stream. The results of the lowered S_{CT} demonstrated a marked influence of higher diffusion on r.m.s. profiles, as shown in Figure 5.14. A case with a smaller $S_{CT} = 0.05$ was run to see if enhanced diffusion can lower the r.m.s. near concentration centerline $\eta_c = 0.0$ and create a bimodal shape, as found by the experiment of Masutani & Bowmann (1986). Figure 5.14 shows that a higher level of diffusion is a component in creating the bimodal shape, i.e., two levels of decay rates as the profiles develop from the low speed stream to the high speed stream. However, it is clear from the trend of the r.m.s. profile that a simple increase in diffusion is not adequate because the fit in the data has deteriorated. A different approach is required to model the turbulent transport term, as was discussed in section 5.2.2., or improve the inflow boundary condition.

The Figure 5.14b shows r.m.s. of concentration for $S_{CT} = 0.3$ and $S_{CT} = 0.7$ for the simulation and the experiment of Masutani & Bowmann (1986). The r.m.s. of concentration profile shown for the experiment is for the downstream location 15 cm., which is a location in the most developed region of the layer for which experimental data is available. The bars in Figure 5.14b represent the error of magnitude $\Delta\xi = 0.07$ given in the experiment of Masutani & Bowmann (1986) for the mean concentration (mixture fraction) values. The figure shows that, the r.m.s. values for simulation with $S_{CT} = 0.7$ are within the magnitude of

error at the center. At the edges, especially the high speed side the r.m.s. values are lower than the experiment.

5.2.6 Effect of mixing models and constant C_ϕ

With all other factors like mixing frequency and diffusion kept the same, Figure 5.16 shows that the Curl model results in notably higher mixing than the modified Curl model, with r.m.s. concentration profile being lower for the Curl model. There is no visible difference in the effect of the two models on mean concentration and the spread of concentration, shown in Figures 5.17 and 5.18, respectively.

The results for the tests with modified Curl model carried out by varying the constant C_ϕ, as discussed in section 4.1.3, are shown in Figures 5.19 to 5.21. As C_ϕ is increased, the mixing frequency is increased, and the r.m.s. of concentration in Figure 5.19 decreases. The mean concentration profiles in Figure 5.20 show a notable variation only for a high value of $C_\phi = 2$. The difference in the spread of concentration is visible in Figure 5.21, downstream of x/H = 0.9.

5.2.7 Effect of convection due to turbulent diffusion

Inclusion of the third fractional step of convection due to turbulent diffusion, i.e., due to the gradient of eddy viscosity, resulted in a deterioration of the fit between the experimental data and the model. Figure 5.22 for the mean concentration shows that, compared to the base run

in Figure 5.7, the fast free stream is reached earlier, whereas the slow free stream is reached much later, at about $\eta_c = -0.07$. The r.m.s. profiles in Figure 5.23 imply higher mixing on the high speed side, as is the case with base run, but the profiles in general show a deterioration in similarity. This point was not further investigated because the physical interpretation is unclear.

5.2.8 Effect of constant mixing frequency

In order to interpret the asymmetry in the r.m.s. concentration profiles, i.e. the lower r.m.s. on the high speed side, a numerical experiment was conducted using a constant mixing frequency ω across the mixing layer. A numerical study by Vanormelingen and Bulck (1999) suggested high sensitivity of r.m.s. profiles to the variation in mixing frequency. The study showed that the asymmetry in mixing frequency, i.e. considerably higher mixing frequency on the high speed side, was responsible for a lower r.m.s. of concentration on the high speed side. The constant mixing frequency shown in Figure 5.24, is an average of the lateral variation shown in Figure 5.10a, at each streamwise location. In comparison with the base run, the mean profile in Figure 5.25 shows no notable difference, whereas the r.m.s. of concentration in Figure 5.26 show higher values indicating slightly less mixing. Therefore, the uniformity of the mixing frequency across the mixing layer does not explain the asymmetry in the r.m.s. profile. The asymmetry with lower r.m.s. values on the high speed side are due to the inflow boundary condition for concentration. In the present simulation, it is the value of the centre of the tangent hyperbolic profile $y_{oc} = 16.9$ cm., in eq. (4.22),

which produces the asymmetry.

5.2.9 Probability Density Function

The plots for the probability density function (p.d.f.) of the scalar mixture fraction or concentration are shown in Figures 5.27 to 5.29 at several cross-stream locations for downstream stations x =18, 21, and 24 cm., that is, x/H=0.56, 0.66, and 0.75. The p.d.f. at downstream station x=21 cm. in Figure 5.27 is discussed first, since the mean and r.m.s. profiles were in best agreement with the experiment at this station. The p.d.f.s at six cross-stream locations are presented starting from a location on the high speed side, that is positive η_c, and then step towards the low speed side, that is negative η_c. The p.d.f.s have been observed to fall into two classes: marching p.d.f.s, in which the most probable value of the scalar varies across the layer, with the most probable value on each side of the layer being closer to the free stream value of that side, and non-marching p.d.f.s, in which the most probable value of the scalar is substantially independent of the position in the layer, (Rogers and Moser 1994).

Figures 5.27(a,b,c) show p.d.f.s for cross-stream locations on the high speed side. Figure 5.27a shows p.d.f. at location η_c=0.05, with most probable (peak) value very near to the fast free-stream mixture fraction or concentration value of ξ=0.0. The curve is truncated to keep the same range of probability density, so that the p.d.f.s at different locations may be compared. For η_c=0.017, a location further away from the fast stream, the peak p.d.f. value moves slightly away from ξ=0.0, as shown in Figure 5.27b, but the peak value is still close

to the fast free stream concentration. Similarly, the peak value for η_c=0.008, shown in Figure 5.27c, moves further away but is still closer to the fast free stream concentration ξ=0.0 than to slow free stream concentration ξ=1.0. This indicates a slight marching behaviour on the high speed side. High values of concentration at the edges of the curves are because of the unmixed fluid; they are not representative of the p.d.f.s, and therefore ignored. On the low speed side, Figure 5.27d shows a peak p.d.f. value near η_c=0.4, and Figures 5.27(e,f), do not show any clear peak values. By the definition given above, this is clearly a non-marching behaviour.

Another observation that is made from Figure 5.27 is that the p.d.f. shape of the passive scalar show higher mixed fast stream fluid probabilities over a larger cross-stream extent of the mixing layer as compared with the slow stream fluid. Figures 5.27(a,b,c), show high probabilities for fast stream fluid, whereas Figures 5.27(d,e,f) do not show high probabilities for the slow stream fluid. This indicates that the mixing layer entrains and subsequently mixes larger volumes of fast-stream fluid. Mixture fraction p.d.f.s at x=18 and 24cm, shown in Figures 5.28 and 5.29, respectively, were found to be qualitatively similar.

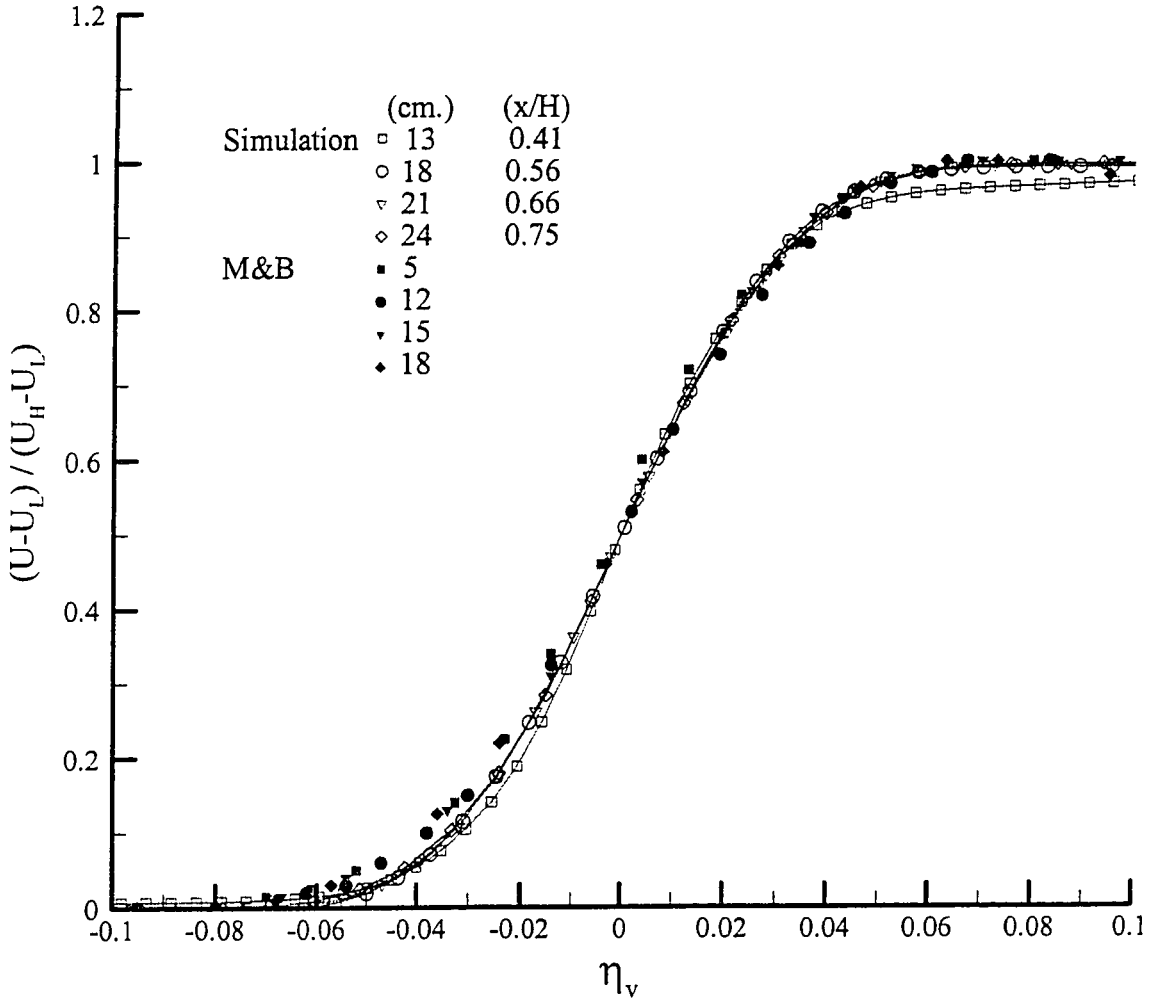

Figure 5.1: The mesh lines show the mean velocity profiles at four downstream locations. Included for comparison is the data from the experiment of Masutani & Bowmann (1986).

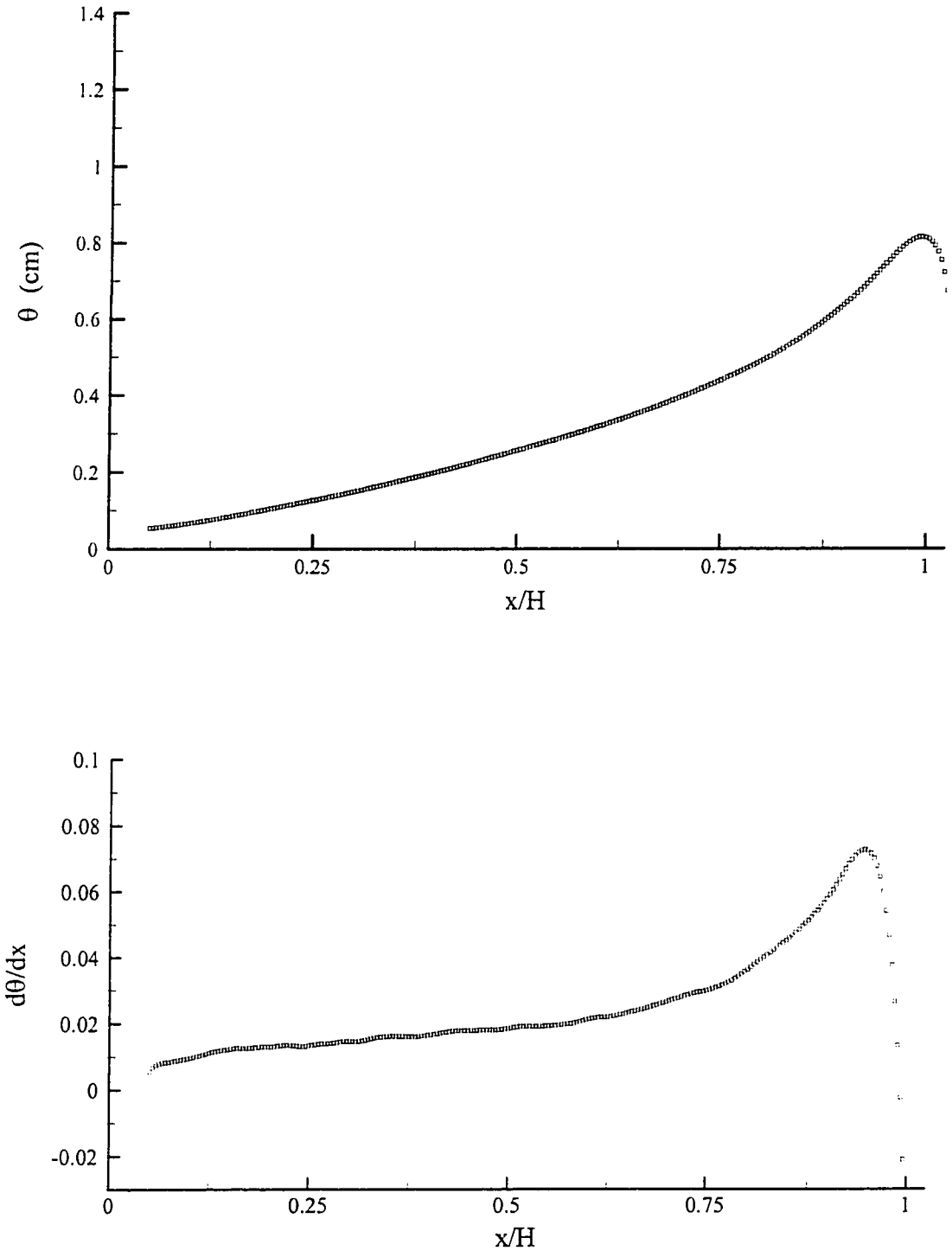

Figure 5.2: (a) Momentum thickness, (b) momentum thickness growth rate, versus x/H.

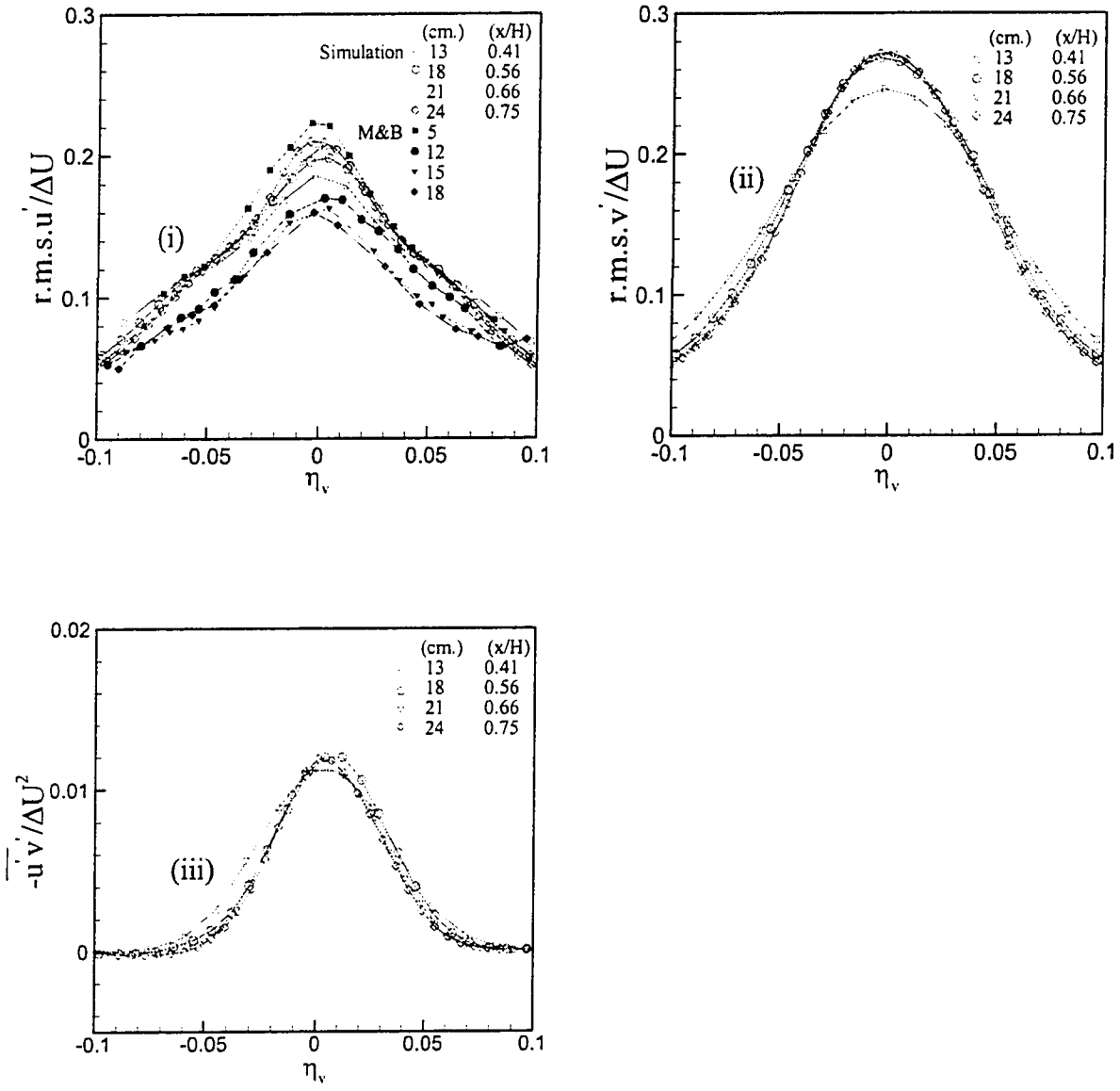

Figure 5.3a: Downstream evolution of (i) r.m.s. longitudinal velocity fluctuations, (ii) r.m.s. lateral velocity fluctuations, (iii) negative cross-stream correlation.

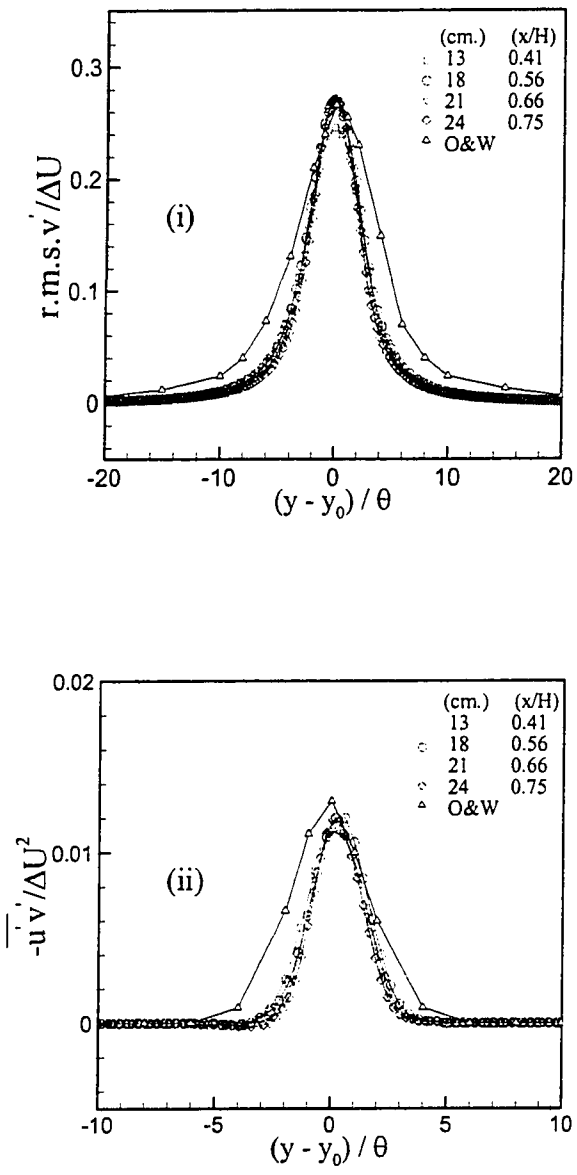

Figure 5.3b: Downstream evolution of (i) r.m.s. lateral velocity fluctuations, and (ii) negative cross-stream correlation, compared with experimental data of O&W (1982)

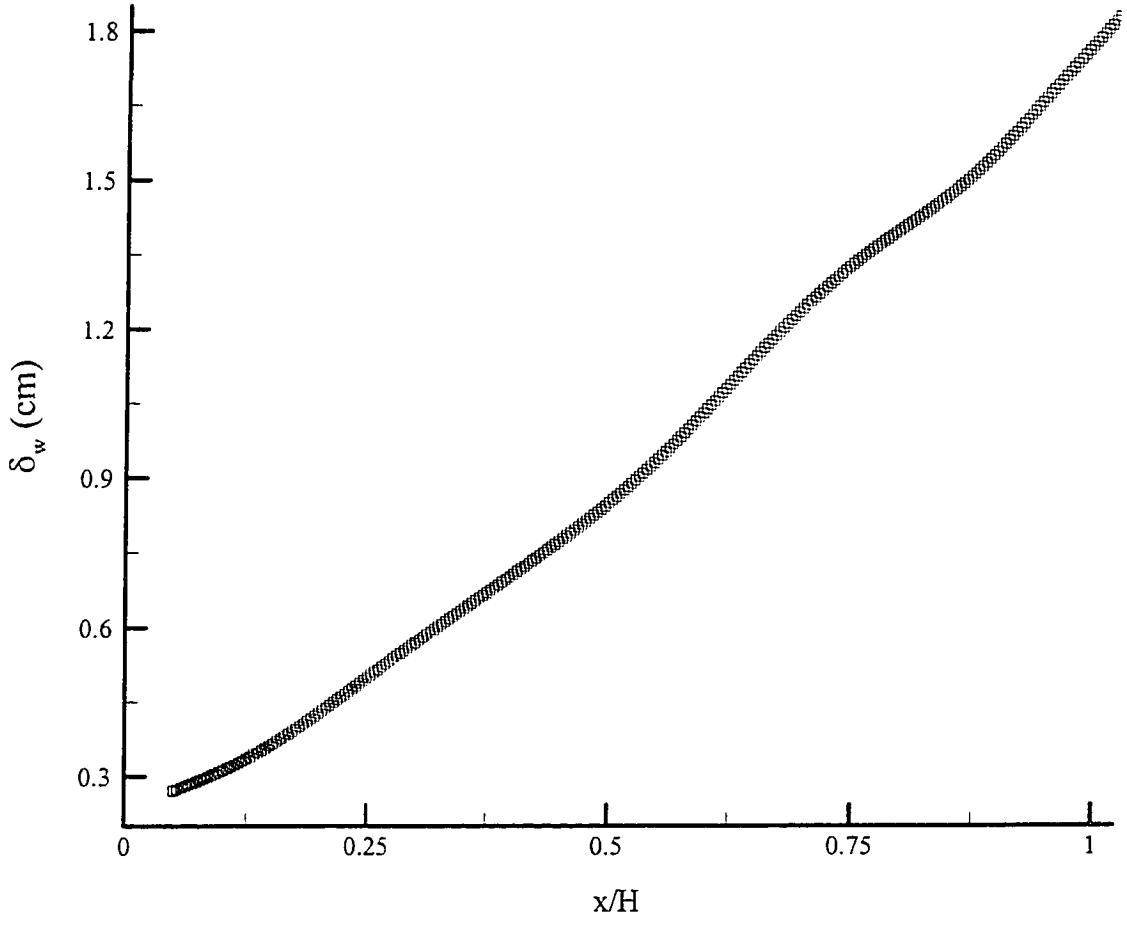

Figure 5.4: Downstream evolution of vorticity thickness.

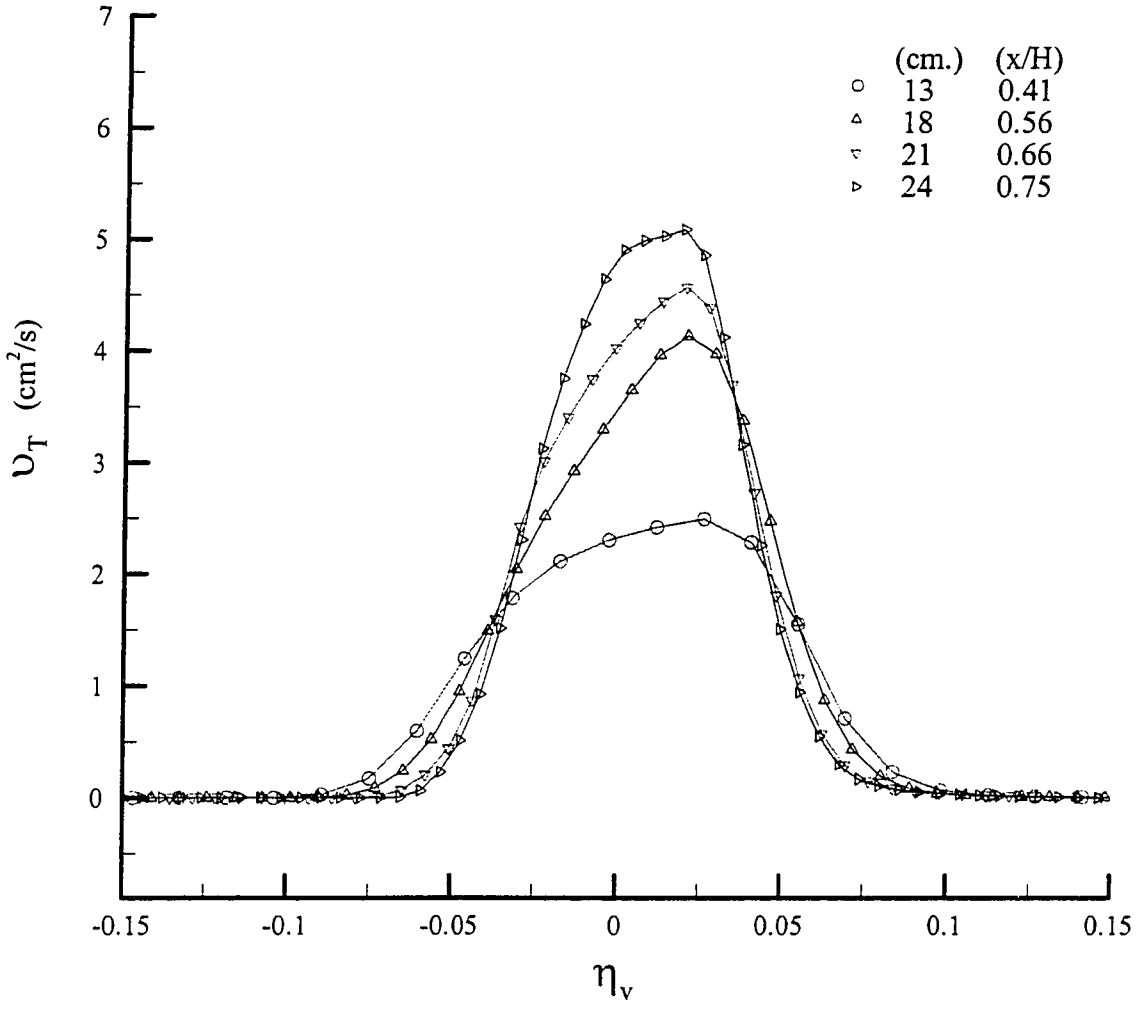

Figure 5.5: Eddy viscosity at four downstream locations.

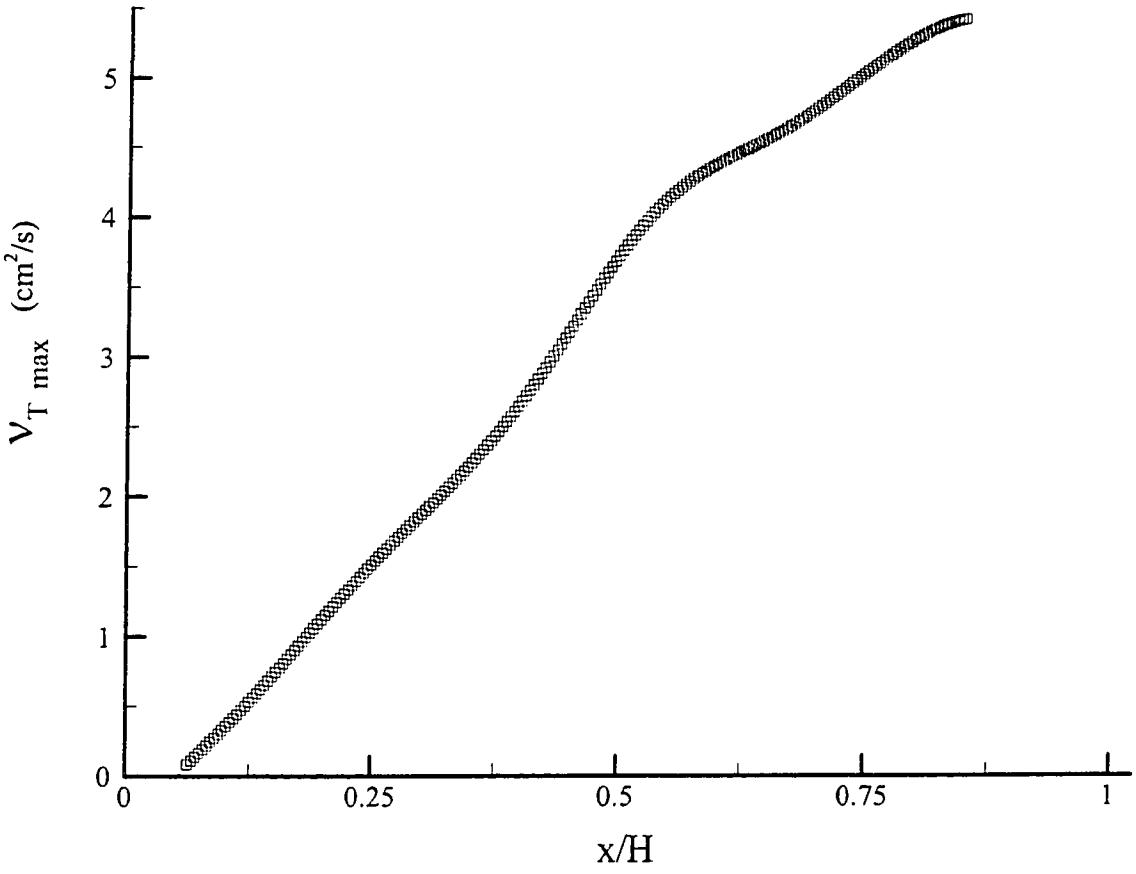

Figure 5.6: Downstream evolution of maximum Eddy viscosity.

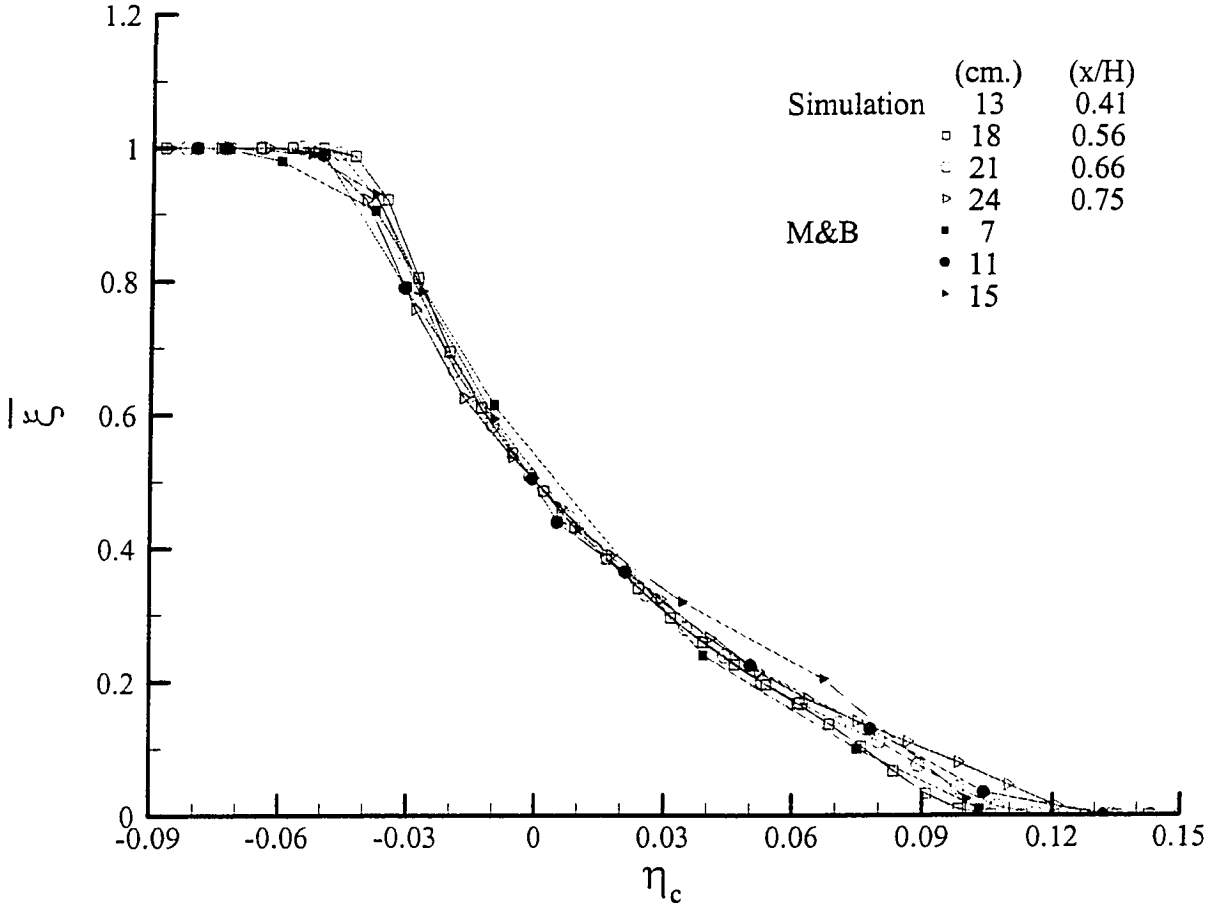

Figure 5.7: Mean concentration profiles at four downstream locations. Included for comparison is the data from the experiment of Masutani & Bowmann (1986).

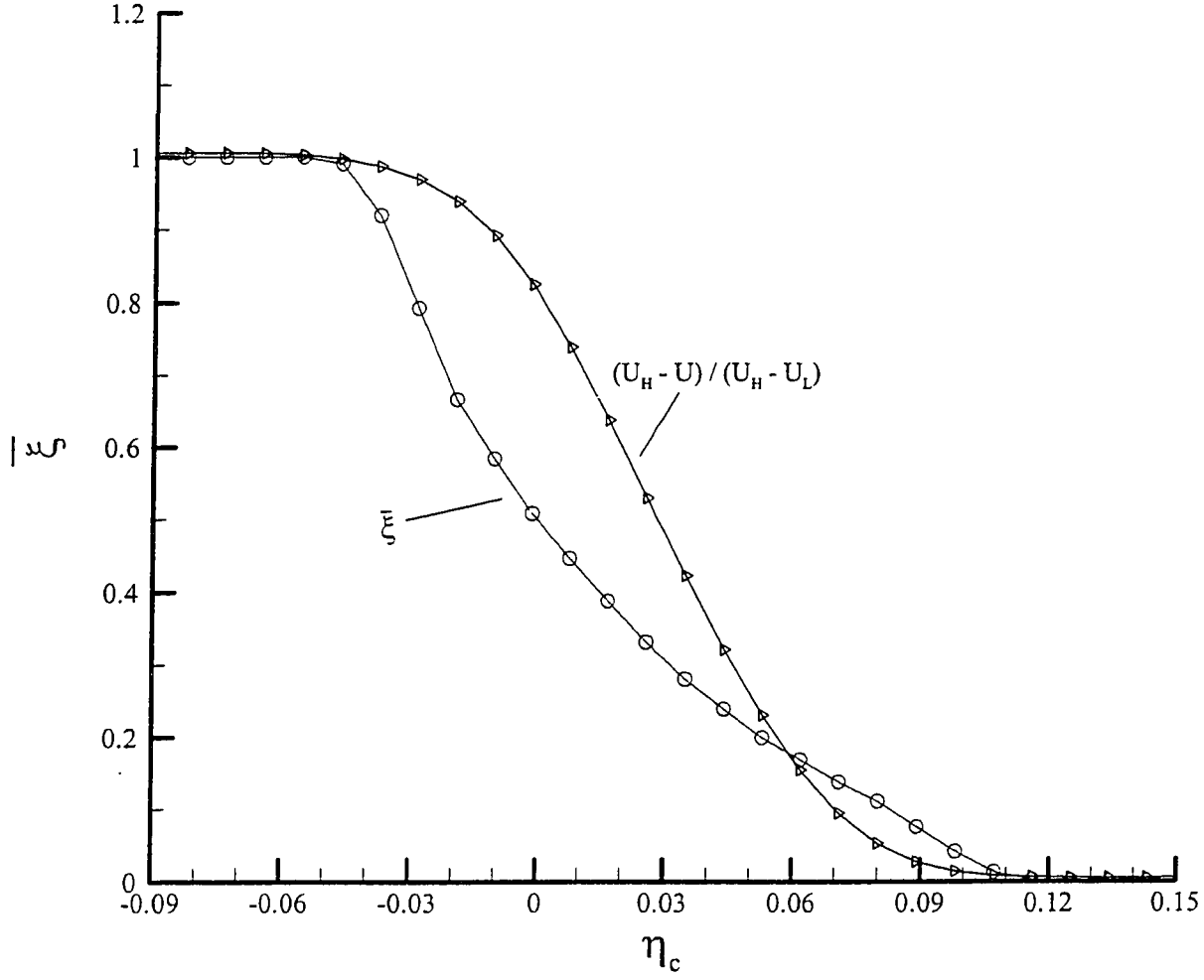

Figure 5.8: Comparison of mean concentration profile and the normalized mean velocity profile at downstream location 21 cm., i.e., x/H = 0.66.

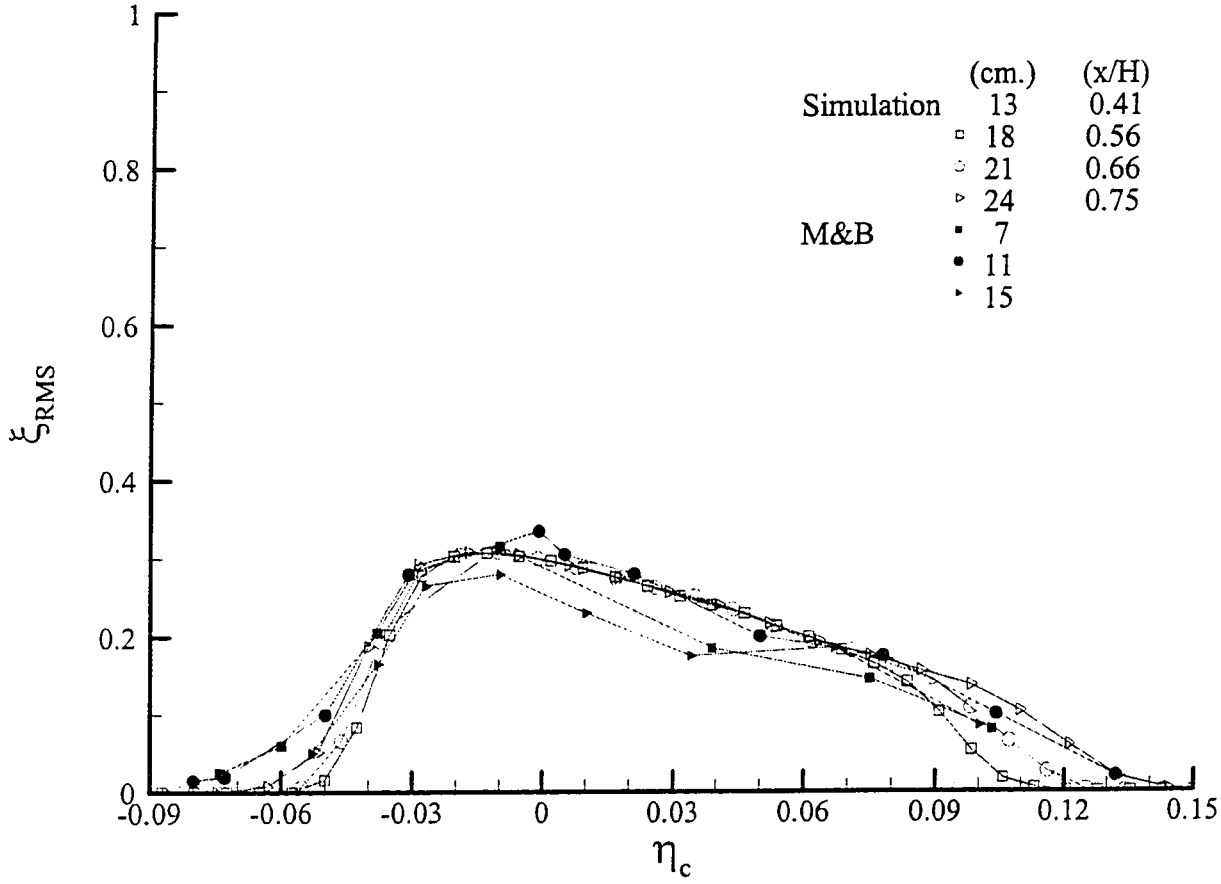

Figure 5.9: RMS of concentration profiles at four downstream locations. Included for comparison is the data from the experiment of Masutani & Bowmann (1986).

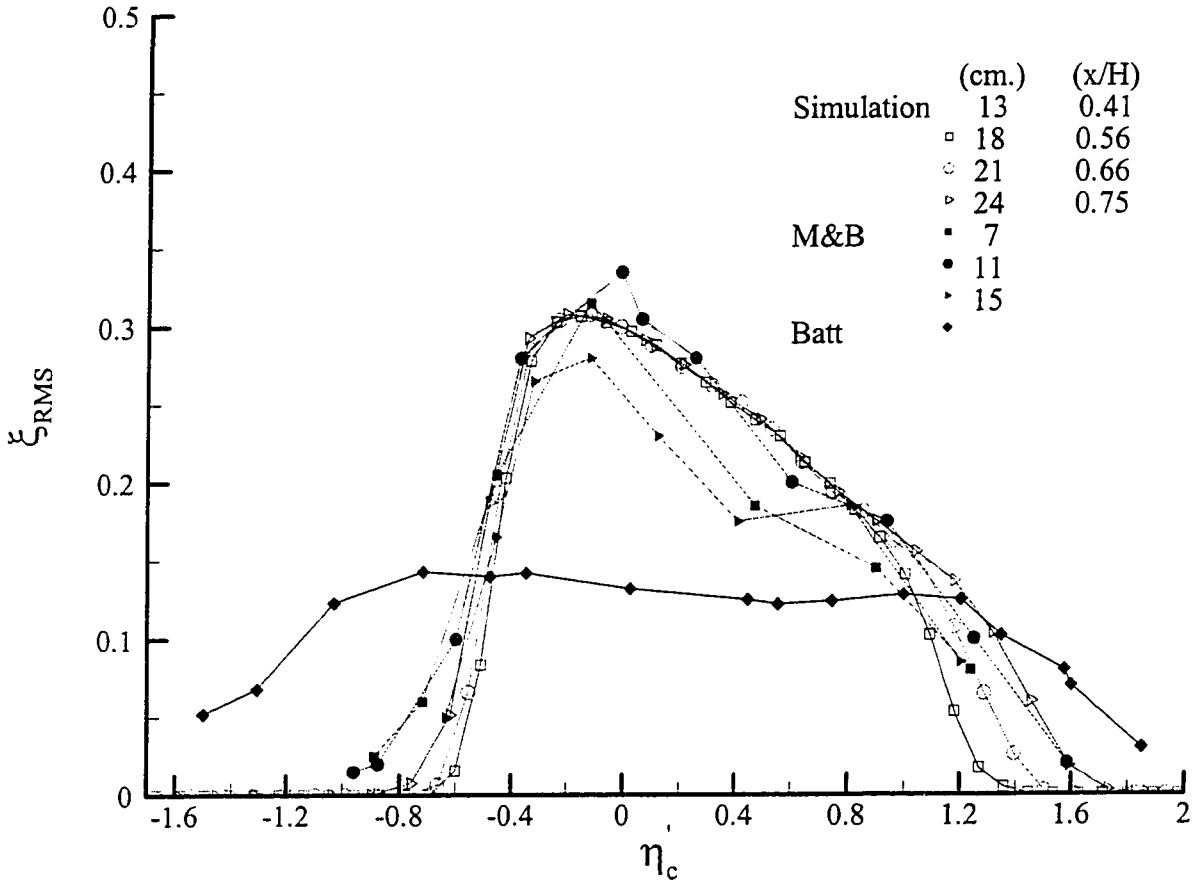

Figure 5.9b: RMS of concentration profiles at four downstream locations. Included for comparison is the data from the experiment of Masutani & Bowmann (1986), and Batt (1977).

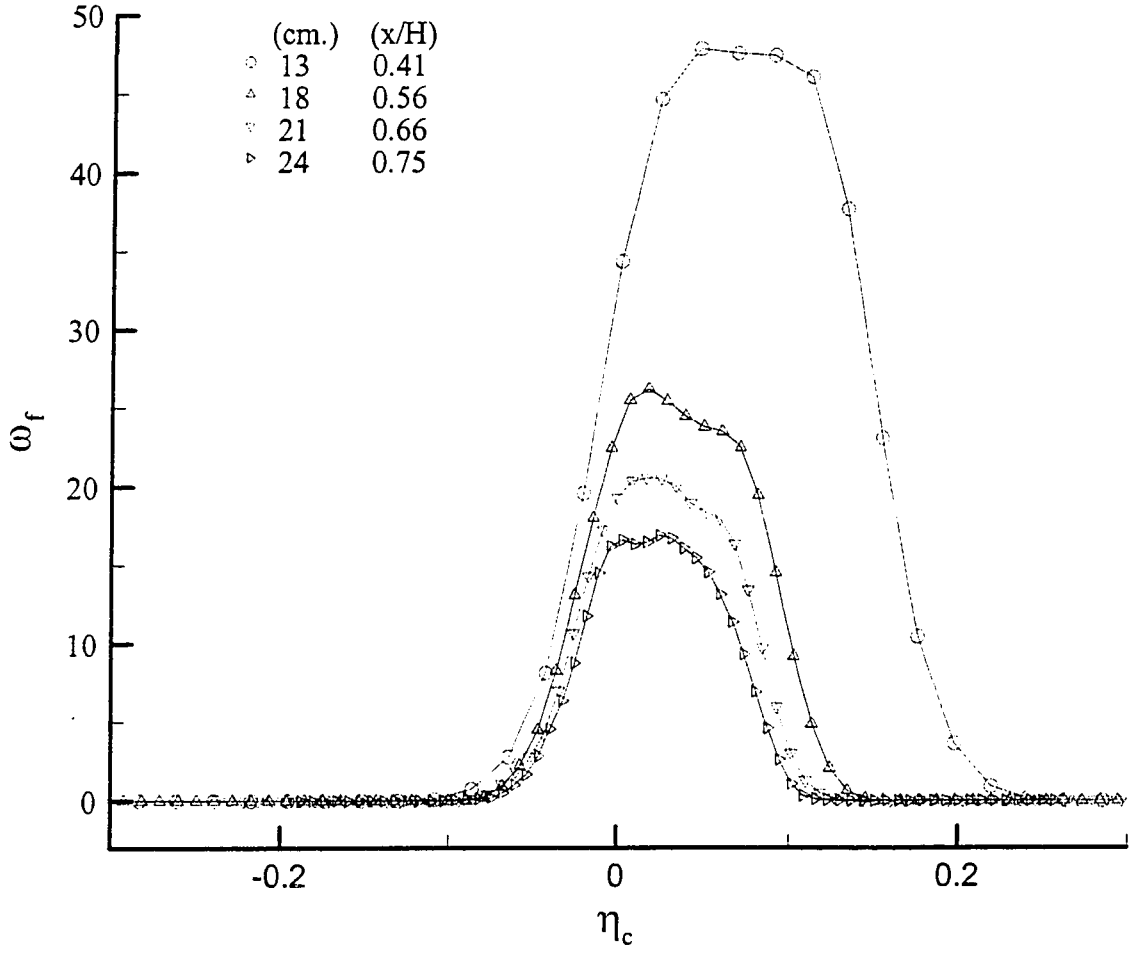

Figure 5.10a: Mixing frequency vs. η_c between downstream locations, x/H = 0.41 to 0.75.

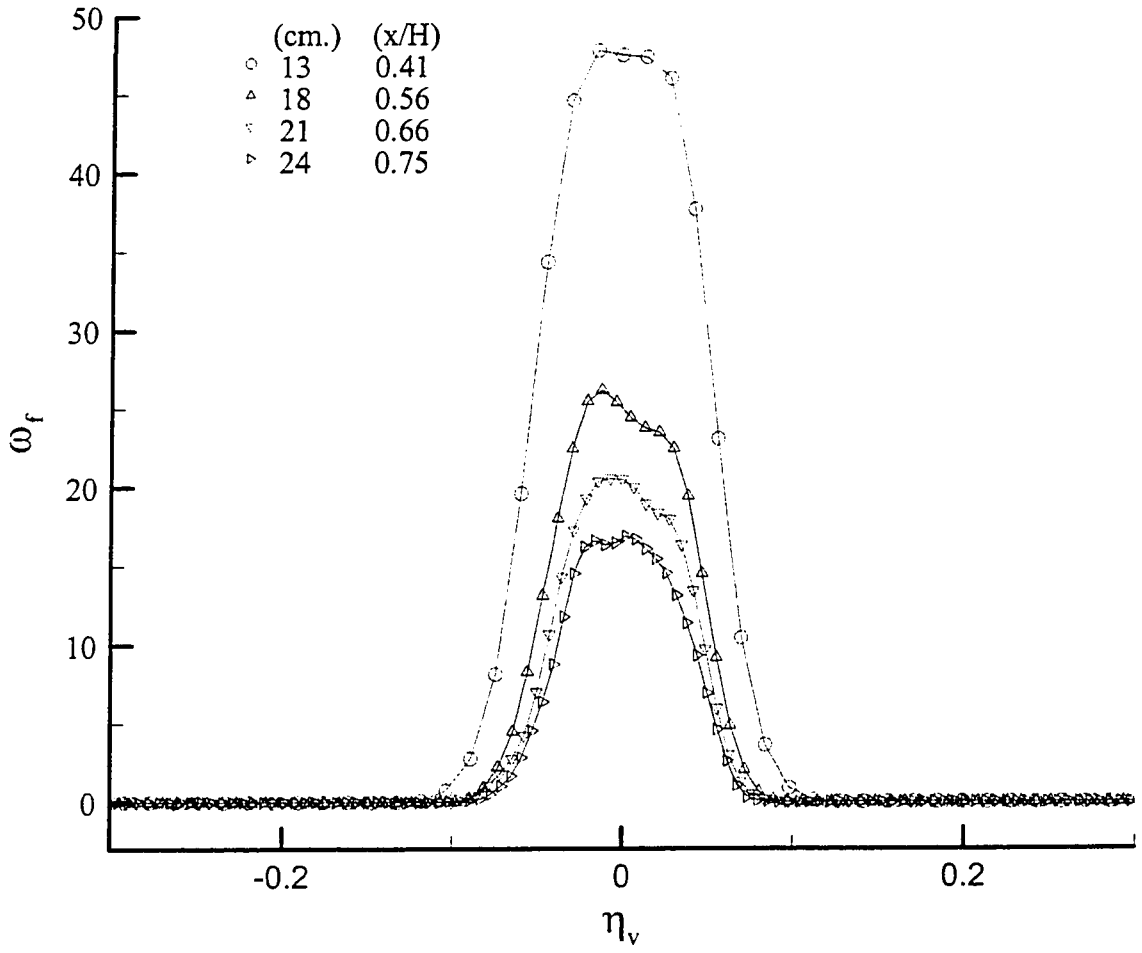

Figure 5.10b: Mixing frequency vs. η_v between downstream locations, x/H = 0.41 to 0.75.

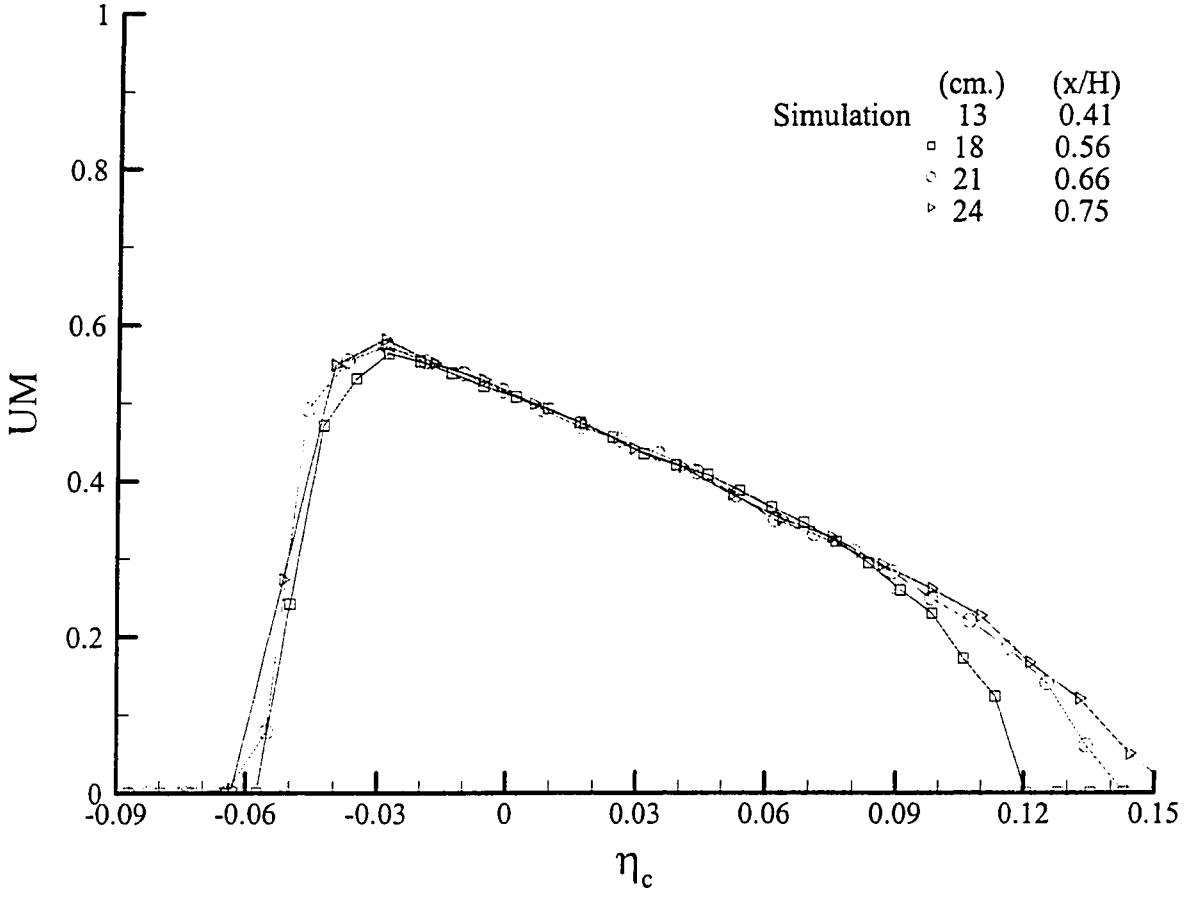

Figure 5.11: Unmixedness profiles at four downstream locations.

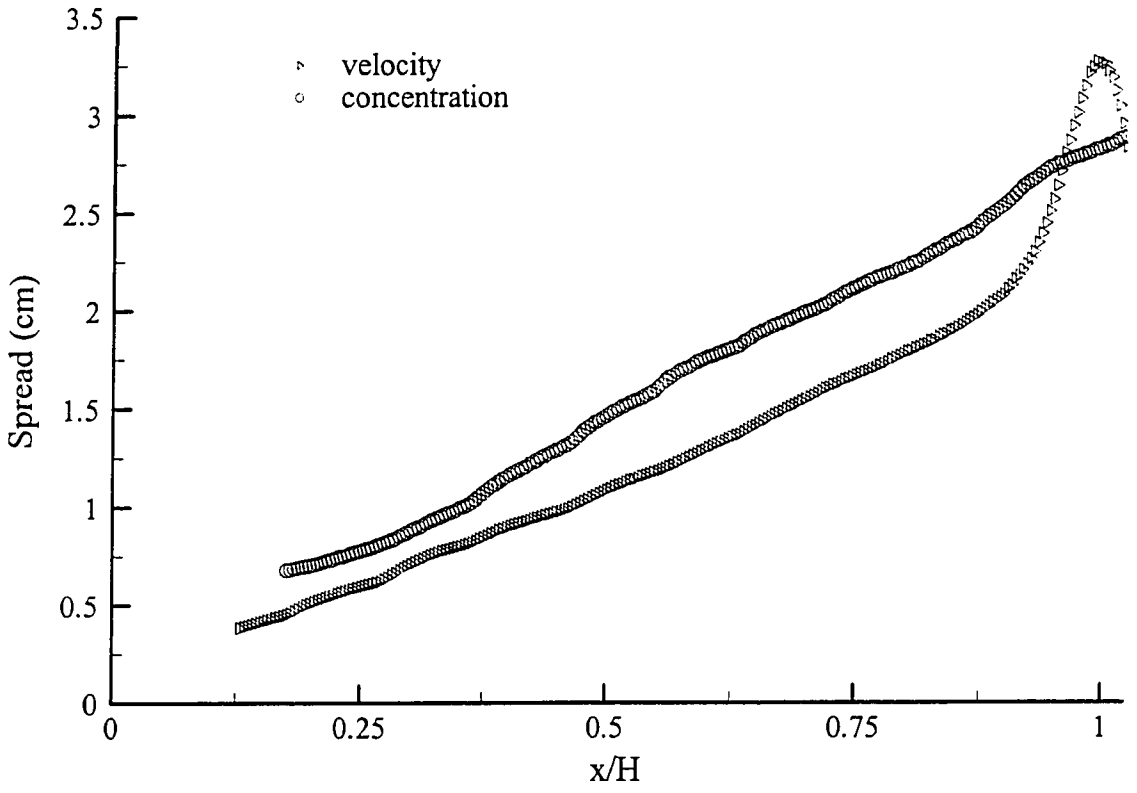

Figure 5.12: Spread of concentration and velocity plot, downstream of respective virtual origins.

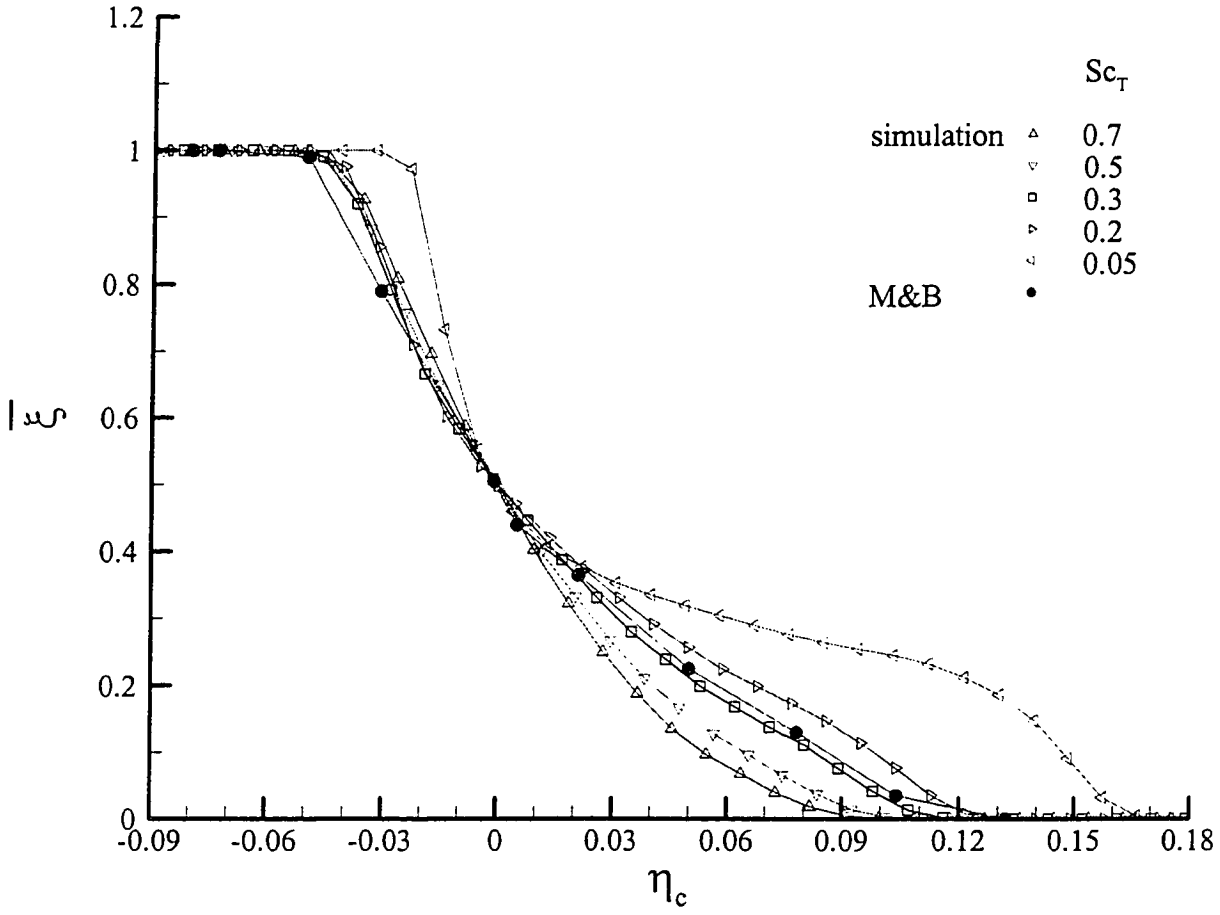

Figure 5.13: Effect of Sc_T on mean concentration profiles, shown at downstream location 21 cm. (x/H = 0.66), for C_ϕ = 0.8. Included for comparison is the data from the experiment of Masutani & Bowmann (1986), at downstream location 11 cm.

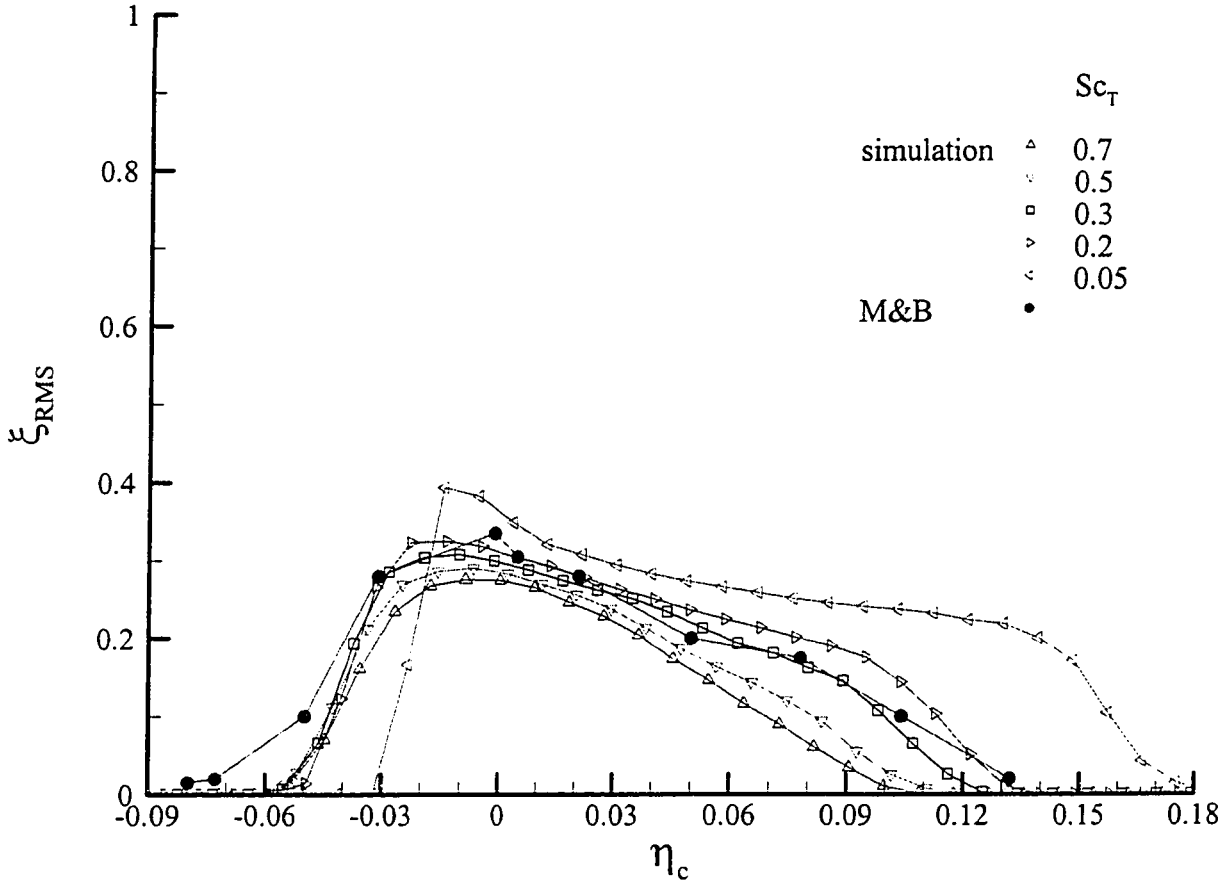

Figure 5.14: Effect of Sc_T on RMS of concentration profiles, shown at downstream location 21 cm. (x/H = 0.66), for C_ϕ = 0.8. Included for comparison is the data from the experiment of Masutani & Bowmann (1986), at downstream location 11 cm.

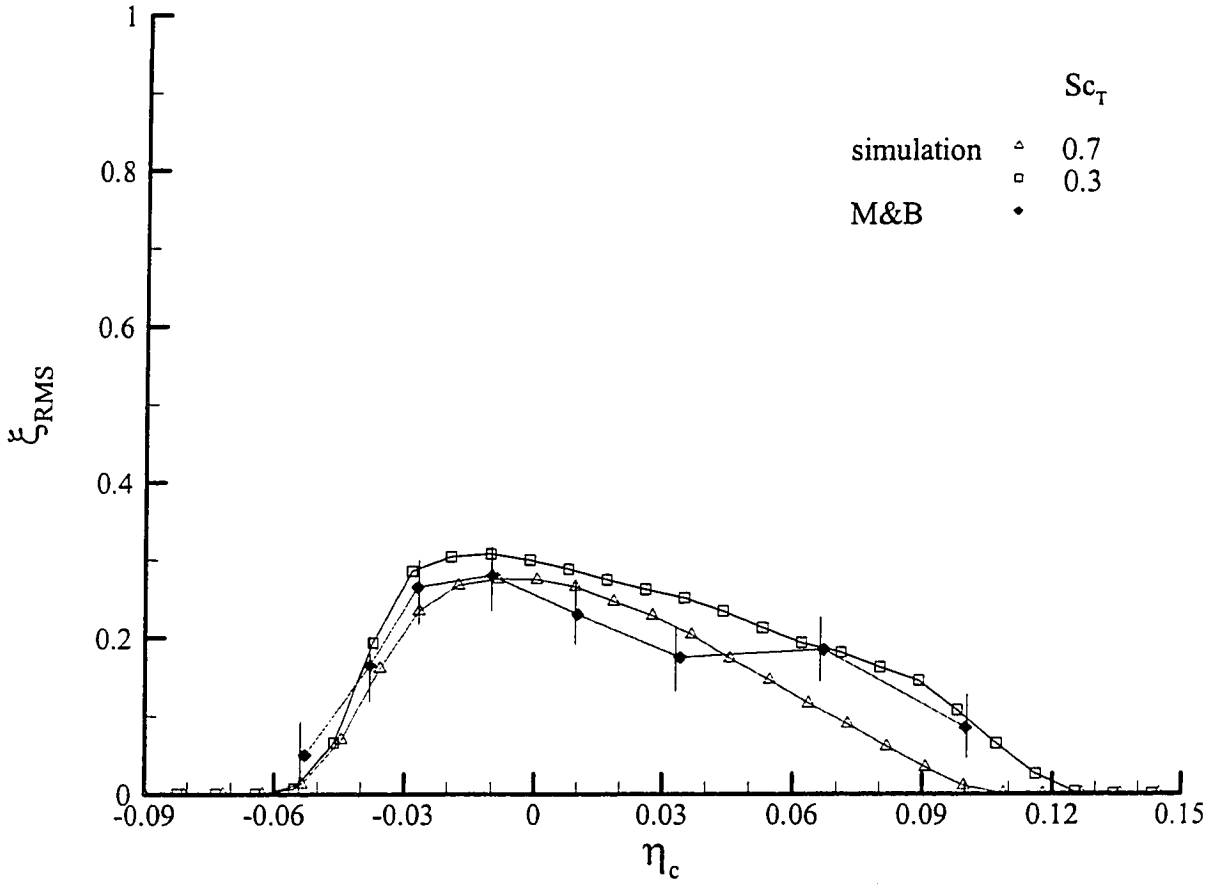

Figure 5.14b: RMS of concentration profiles, shown at downstream location 21 cm. (x/H = 0.66) for Sc_T = 0.3 and 0.7, shown against the data from the experiment of Masutani & Bowmann (1986) at downstream location 15 cm.

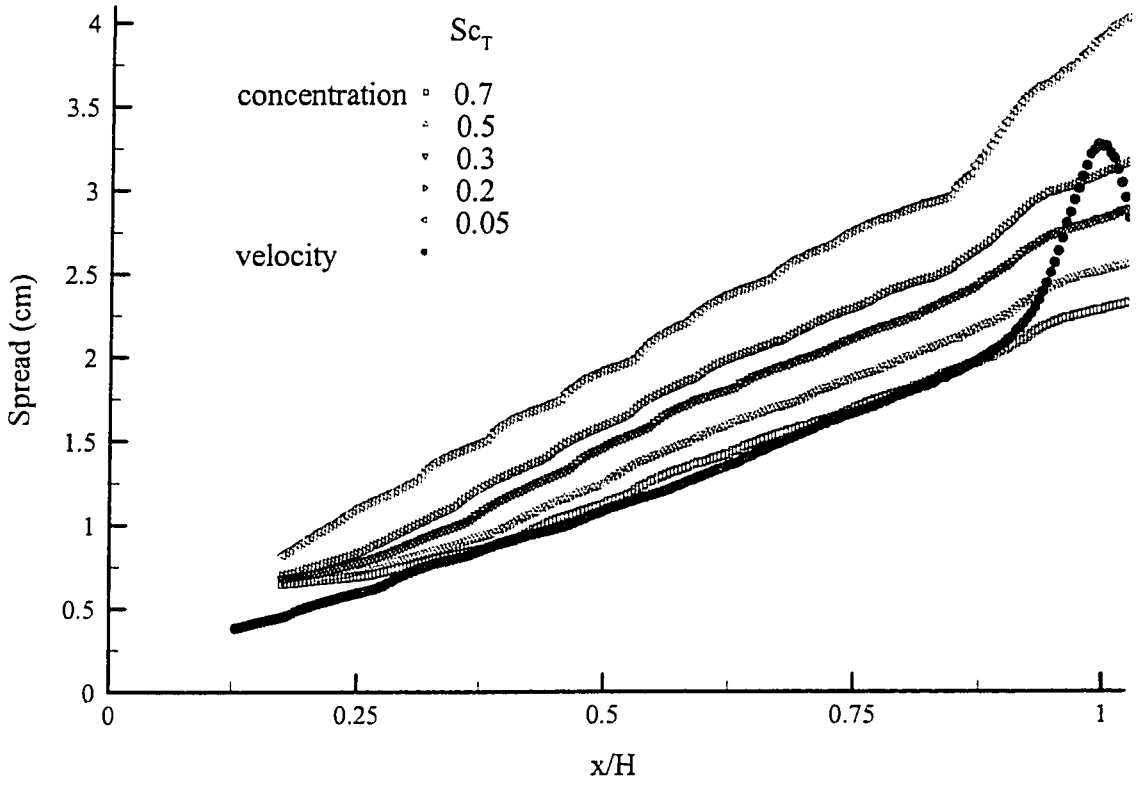

Figure 5.15: Effect of Sc_T on spread of concentration, for $C_\phi = 0.8$. Also shown is the spread of velocity.

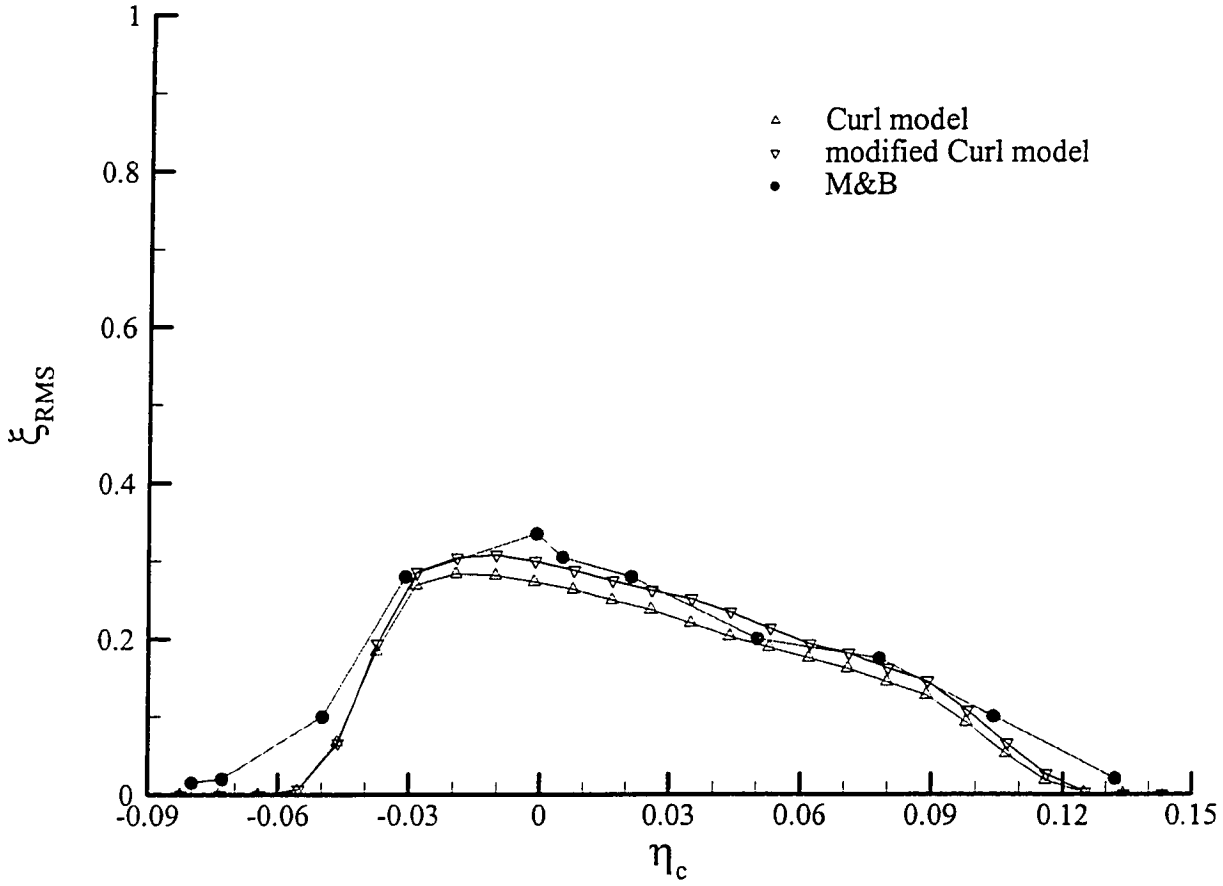

Figure 5.16: Effect of mixing models on RMS concentration profiles, shown at downstream location 21 cm. (x/H = 0.66), for $Sc_T = 0.3$ and $C_\phi = 0.8$. Included for comparison is the data from the experiment of Masutani & Bowmann (1986), at downstream location 11 cm.

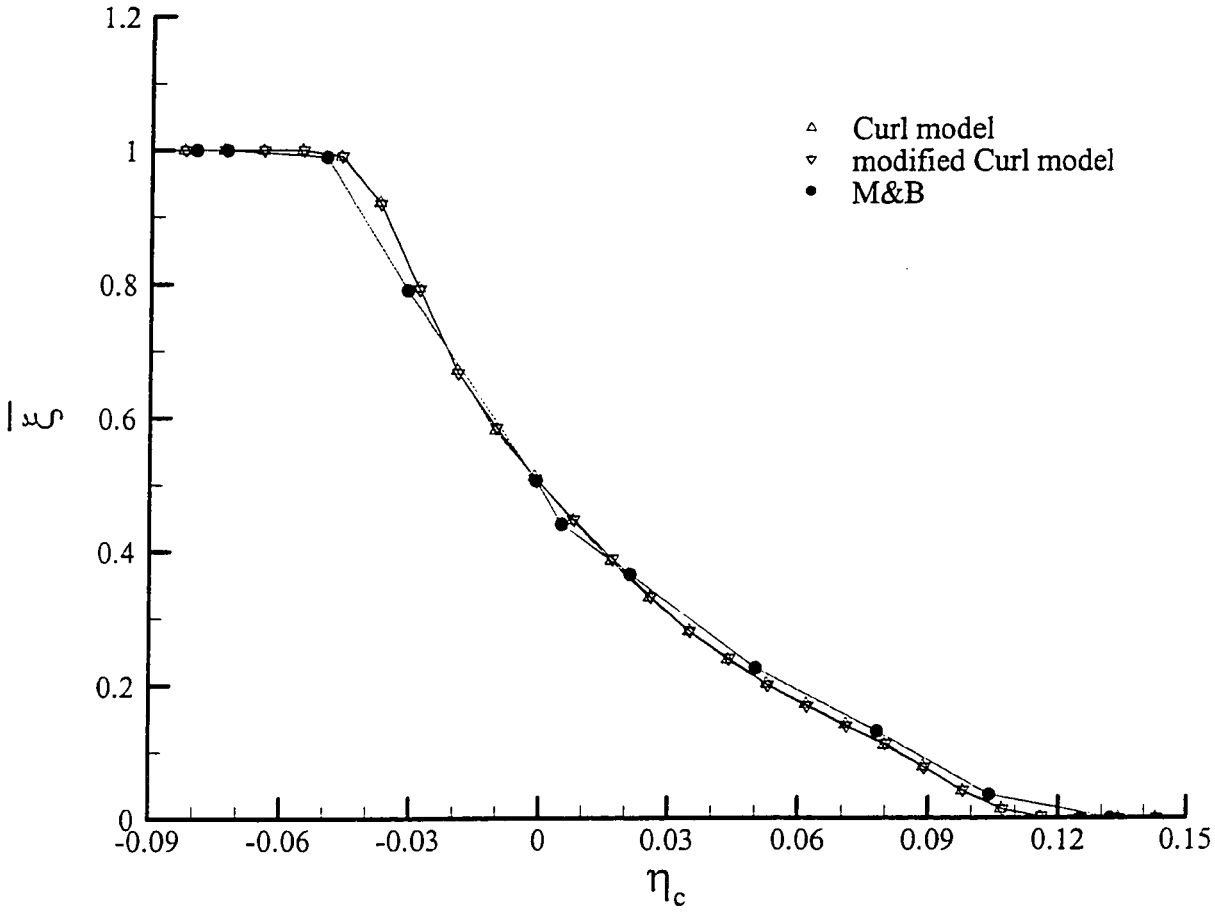

Figure 5.17: Effect of mixing models on mean concentration profiles, shown at downstream location 21 cm. (x/H = 0.66), for $Sc_T = 0.3$ and $C_\phi = 0.8$. Included for comparison is the data from the experiment of Masutani & Bowmann (1986), at downstream location 11 cm.

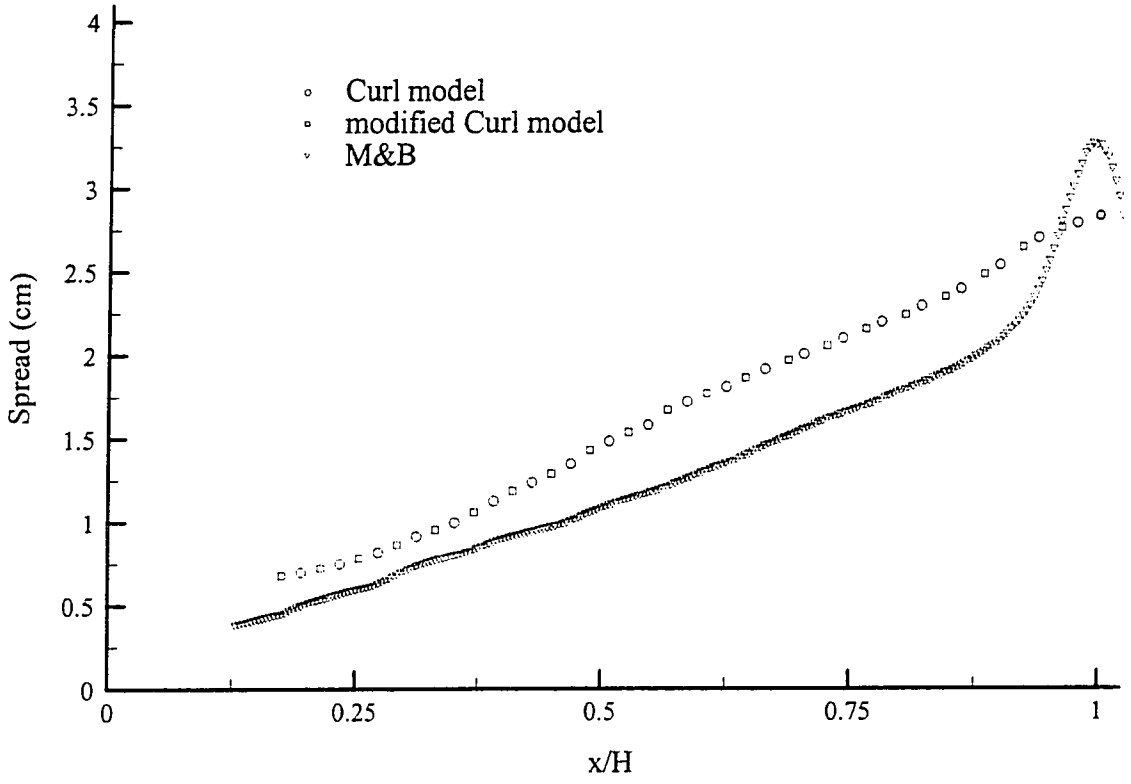

Figure 5.18: Effect of mixing models on spread of concentration. Also shown is the spread of velocity.

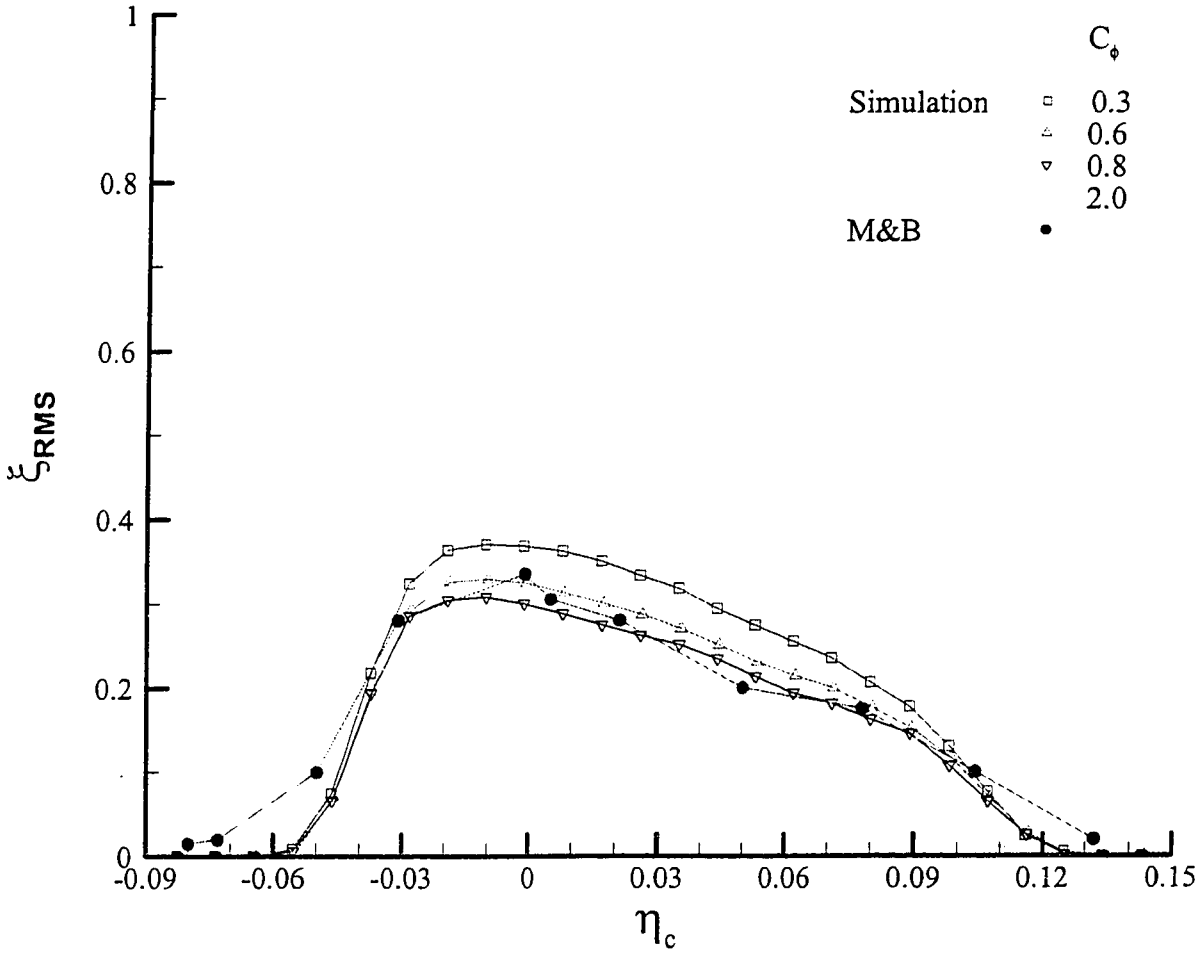

Figure 5.19: Effect of constant C_ϕ on RMS of concentration profiles, shown at downstream location 21 cm. ($x/H = 0.66$), for $Sc_T = 0.3$. Included for comparison is the data from the experiment of Masutani & Bowmann (1986), at downstream location 11 cm.

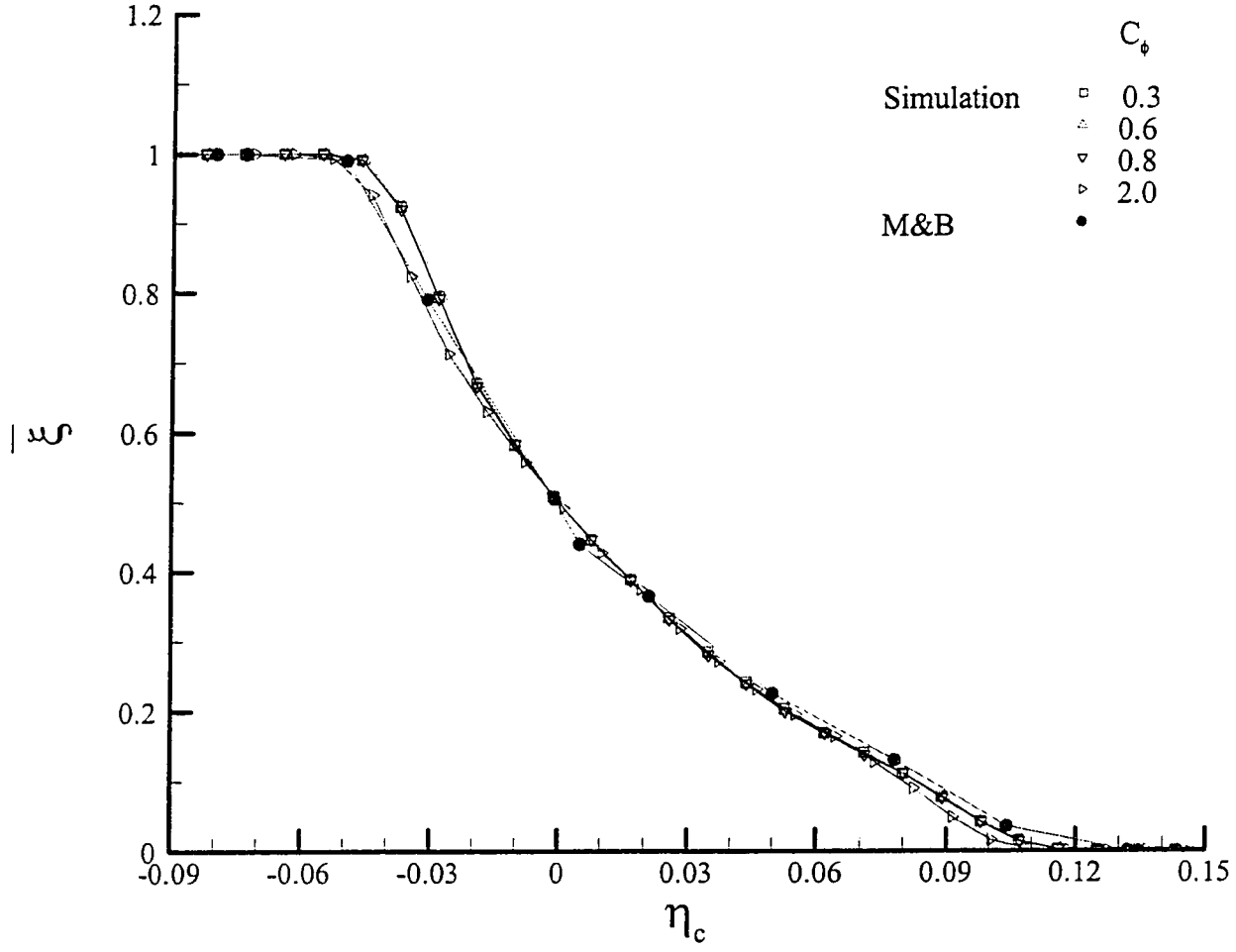

Figure 5.20: Effect of constant C_ϕ on mean concentration profiles, shown at downstream location 21 cm. ($x/H = 0.66$), for $Sc_T = 0.3$. Included for comparison is the data from the experiment of Masutani & Bowmann (1986), at downstream location 11 cm.

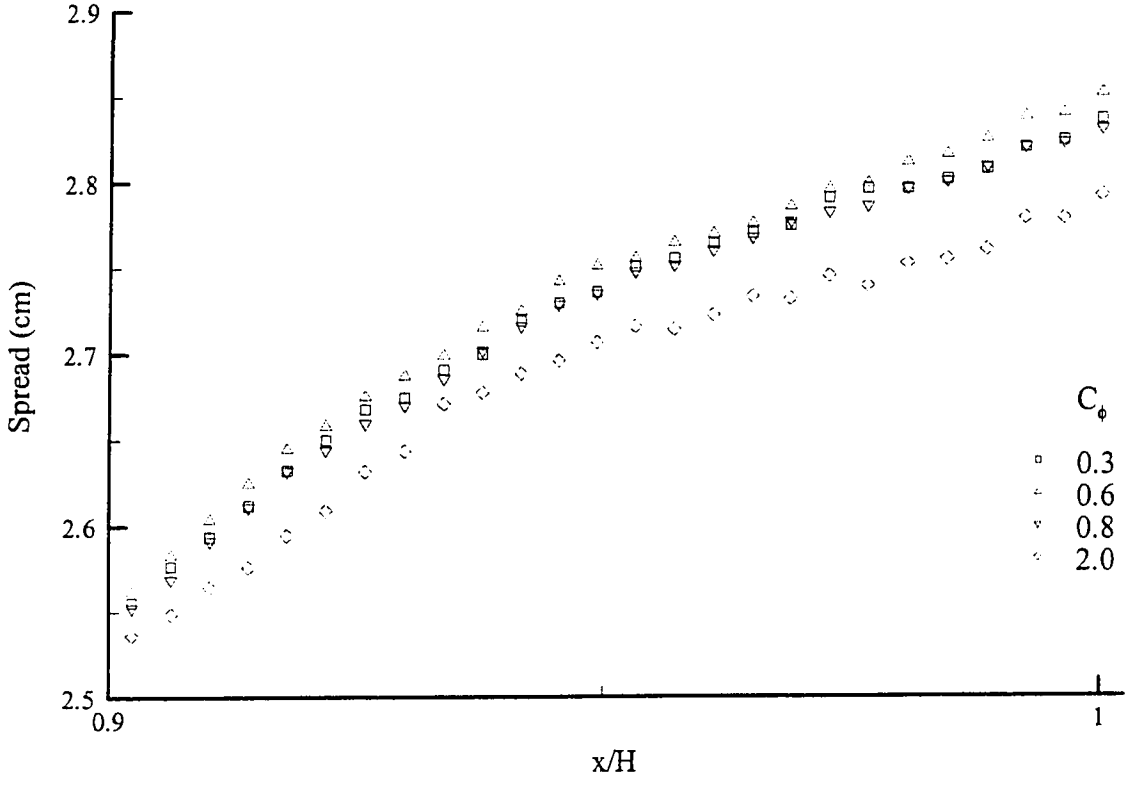

Figure 5.21 : Effect of C_ϕ on spread of concentration shown downstream of x/H = 0.9, for $Sc_T = 0.3$.

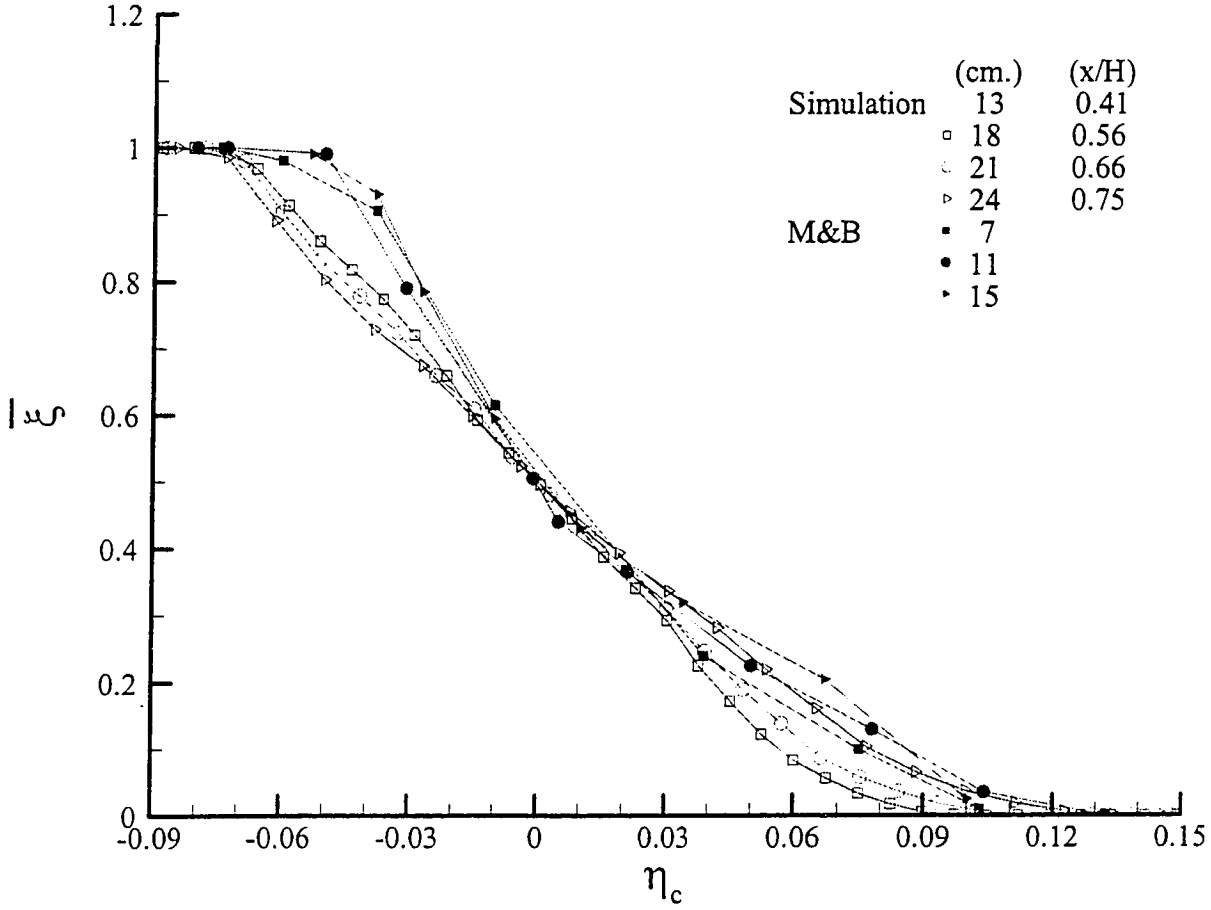

Figure 5.22: Mean concentration profiles at four downstream locations, for simulation with parameters of the base run, but including the third fractional step, the gradient of eddy viscosity. Included for comparison is the data from the experiment of Masutani & Bowmann (1986).

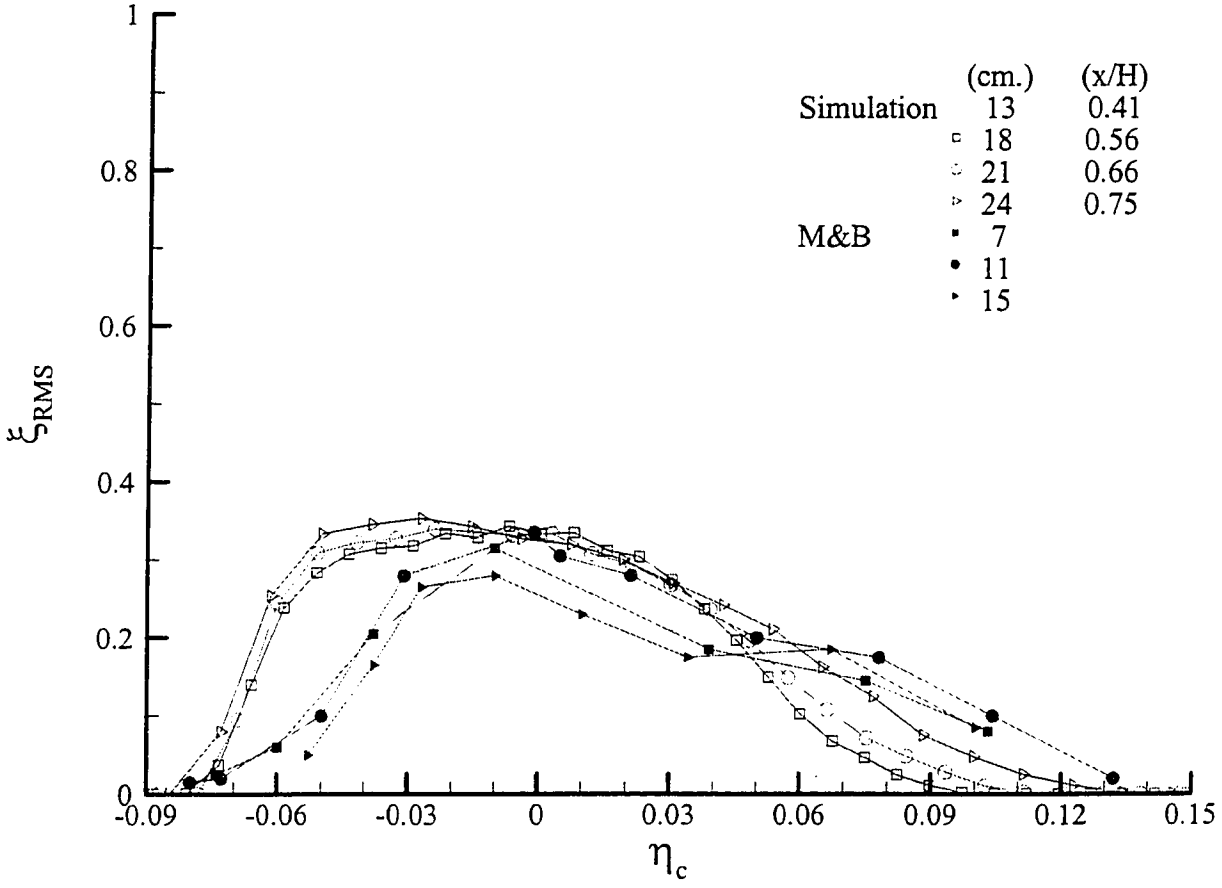

Figure 5.23: RMS of concentration profiles at four downstream locations, for simulation with parameters of the base run, but including the third fractional step, the gradient of eddy viscosity. Included for comparison is the data from the experiment of Masutani & Bowmann (1986).

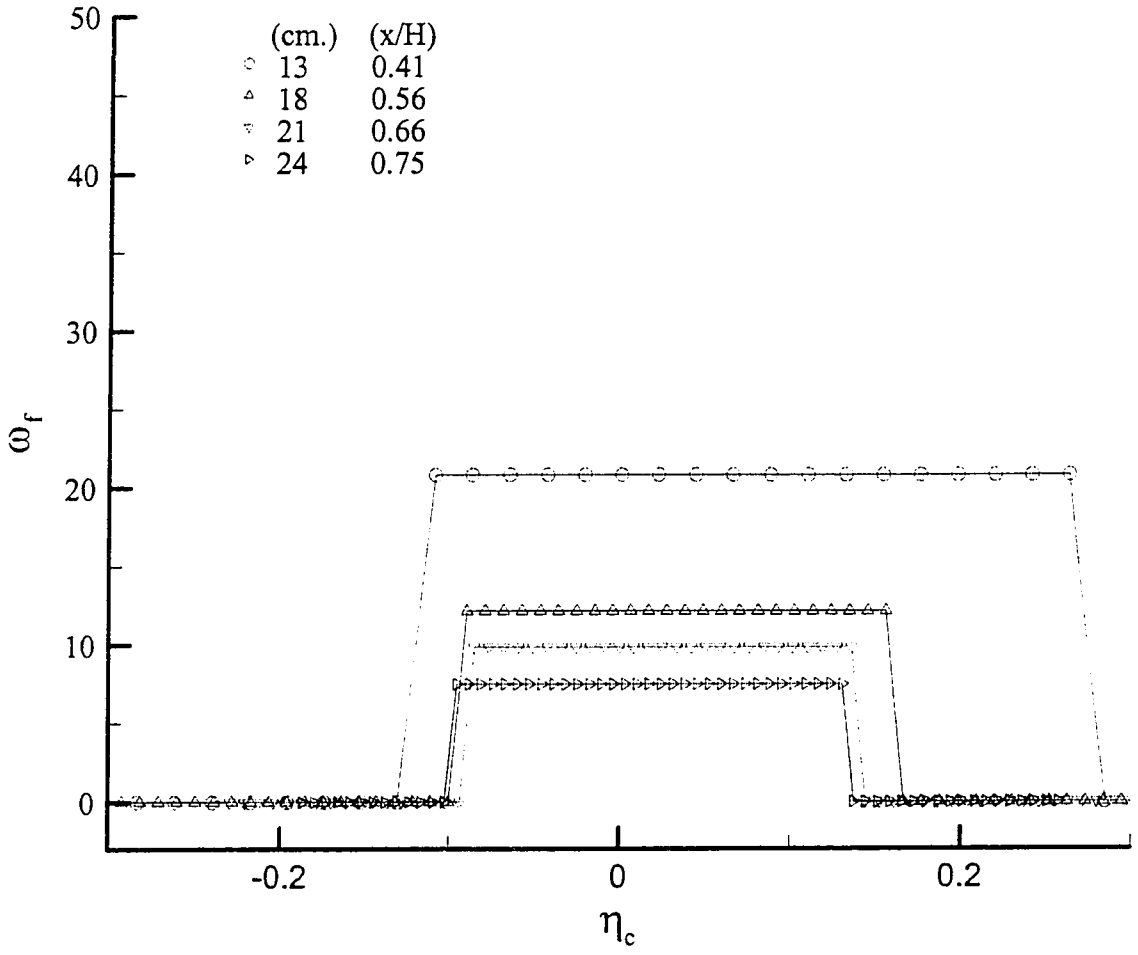

Figure 5.24: Constant cross-stream mixing frequency between downstream locations, x/H = 0.41 to 0.75, for $C_\phi = 0.8$.

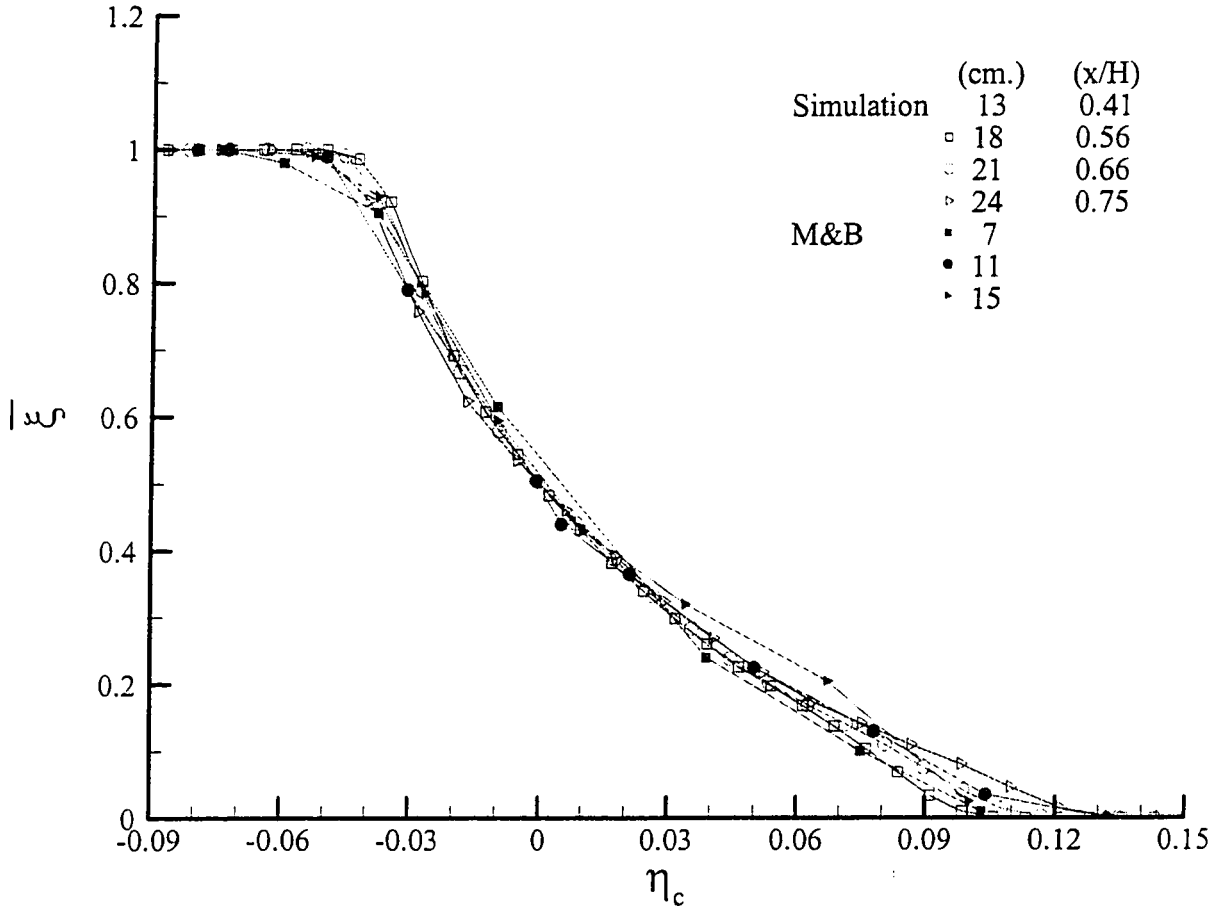

Figure 5.25: Mean concentration profiles at four downstream locations, for a constant cross-stream mixing frequency. Included for comparison is the data from the experiment of Masutani & Bowmann (1986).

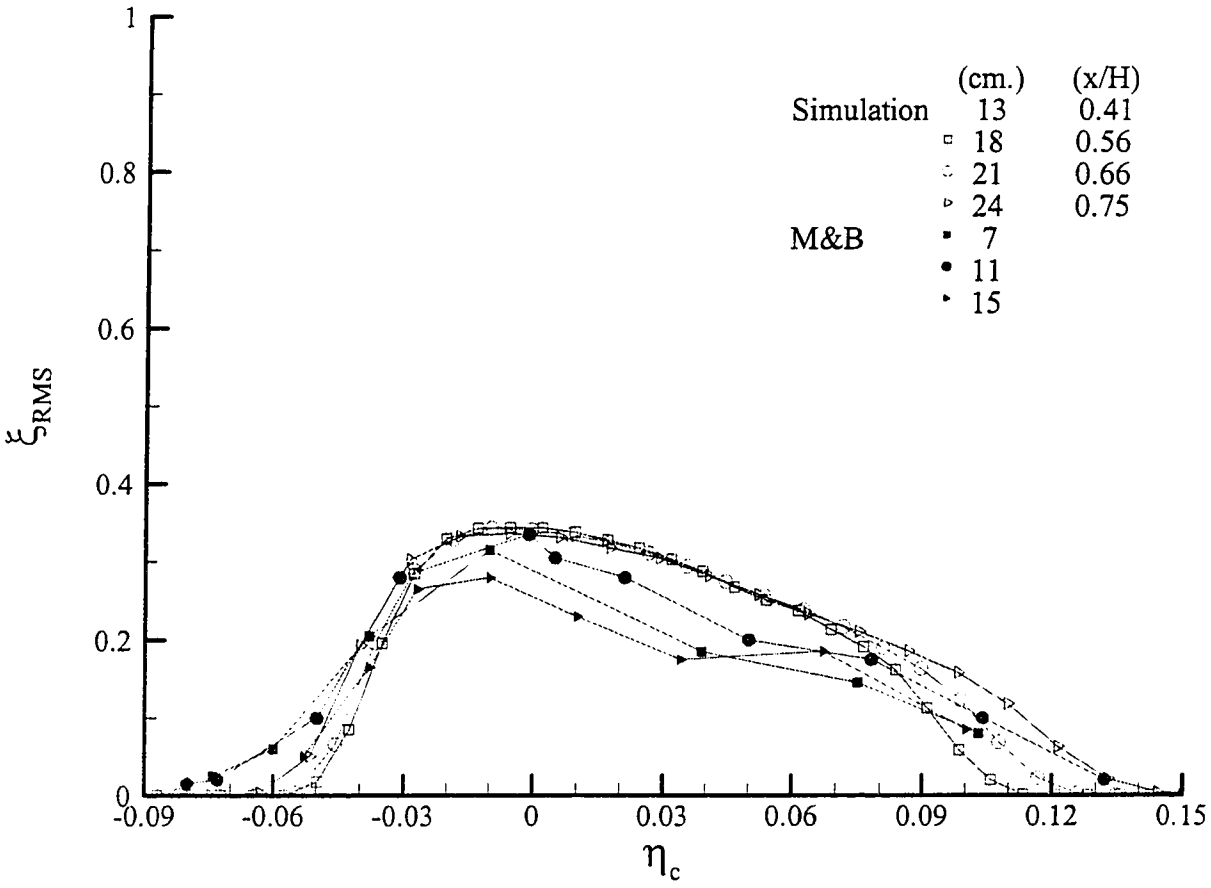

Figure 5.26: RMS of concentration profiles at four downstream locations, for a constant cross-stream mixing frequency. Included for comparison is the data from the experiment of Masutani & Bowmann (1986).

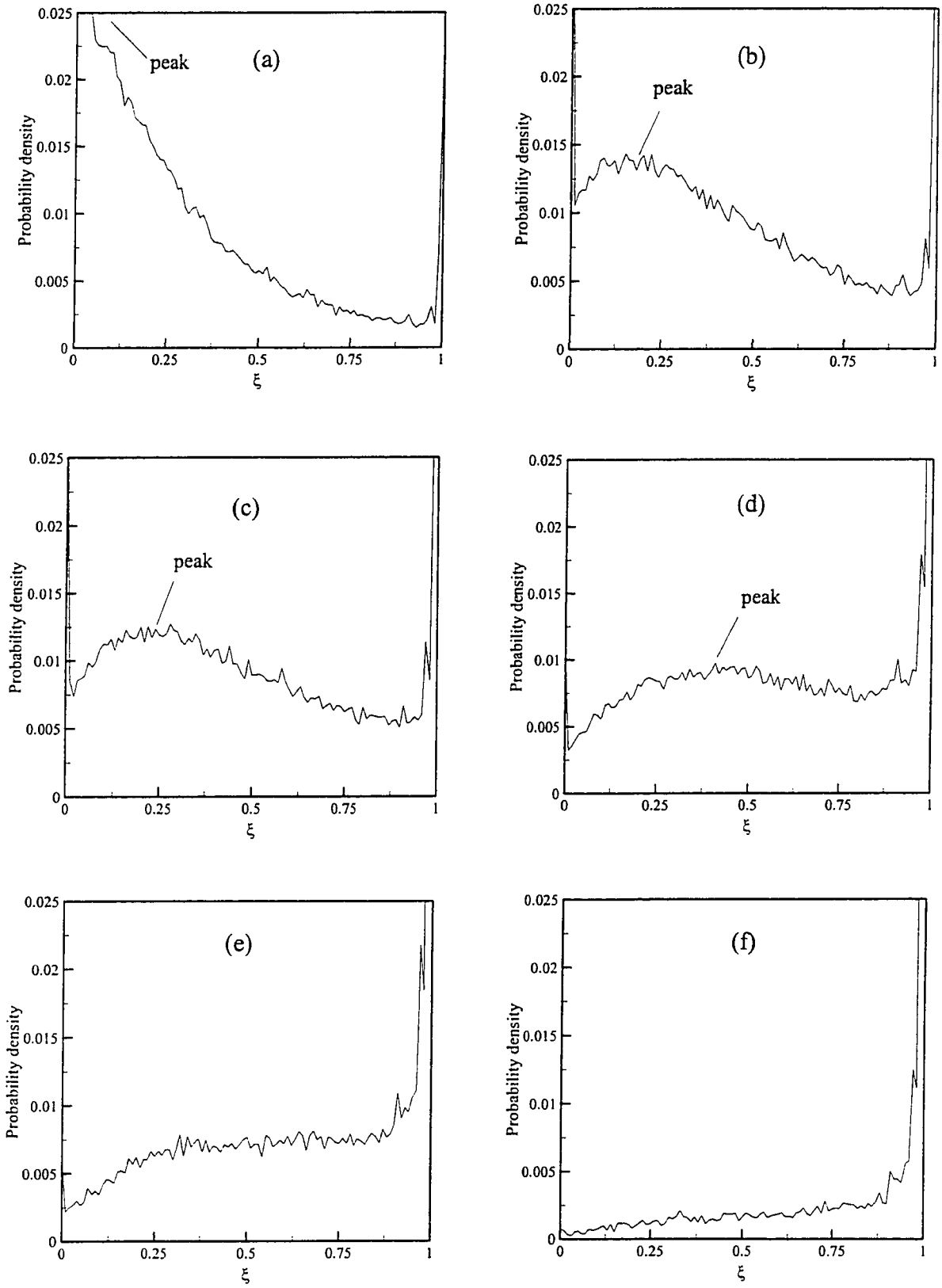

Figure 5.27: PDF shape of passive scalar at several cross-stream locations, for downstream station x=21cm (x/H=0.66). a) η_c=0.05; b) η_c=0.017; c) η_c=0.008; d) η_c=-0.01; e) η_c=-0.02; f) η_c=-0.037.

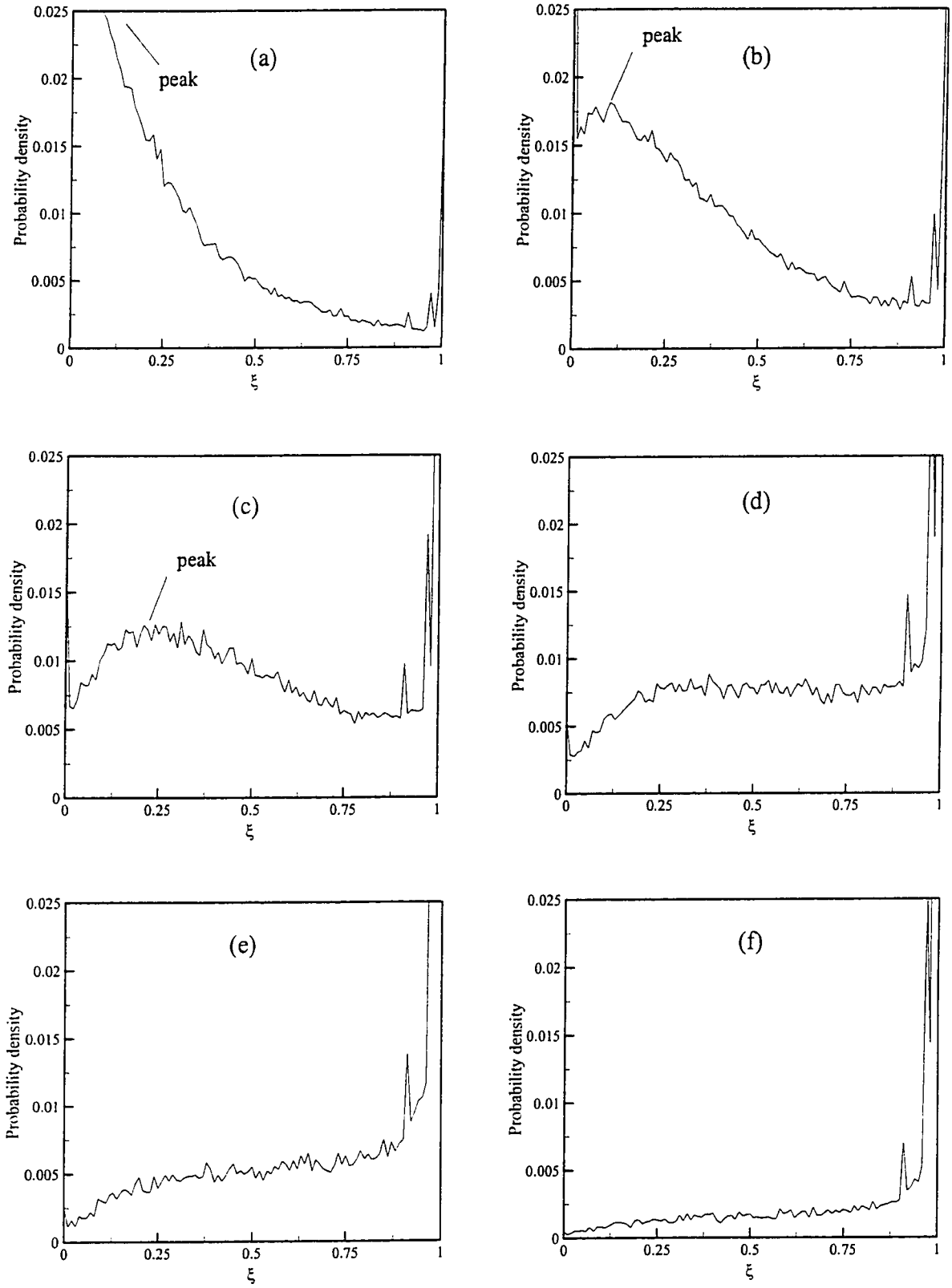

Figure 5.28: PDF shape of passive scalar at several cross-stream locations, for downstream station x=18cm (x/H=0.56). a) η_c=0.052; b) η_c=0.029; c) η_c=0.0064; d) η_c=-0.016; e) η_c=-0.028; f) η_c=-0.04.

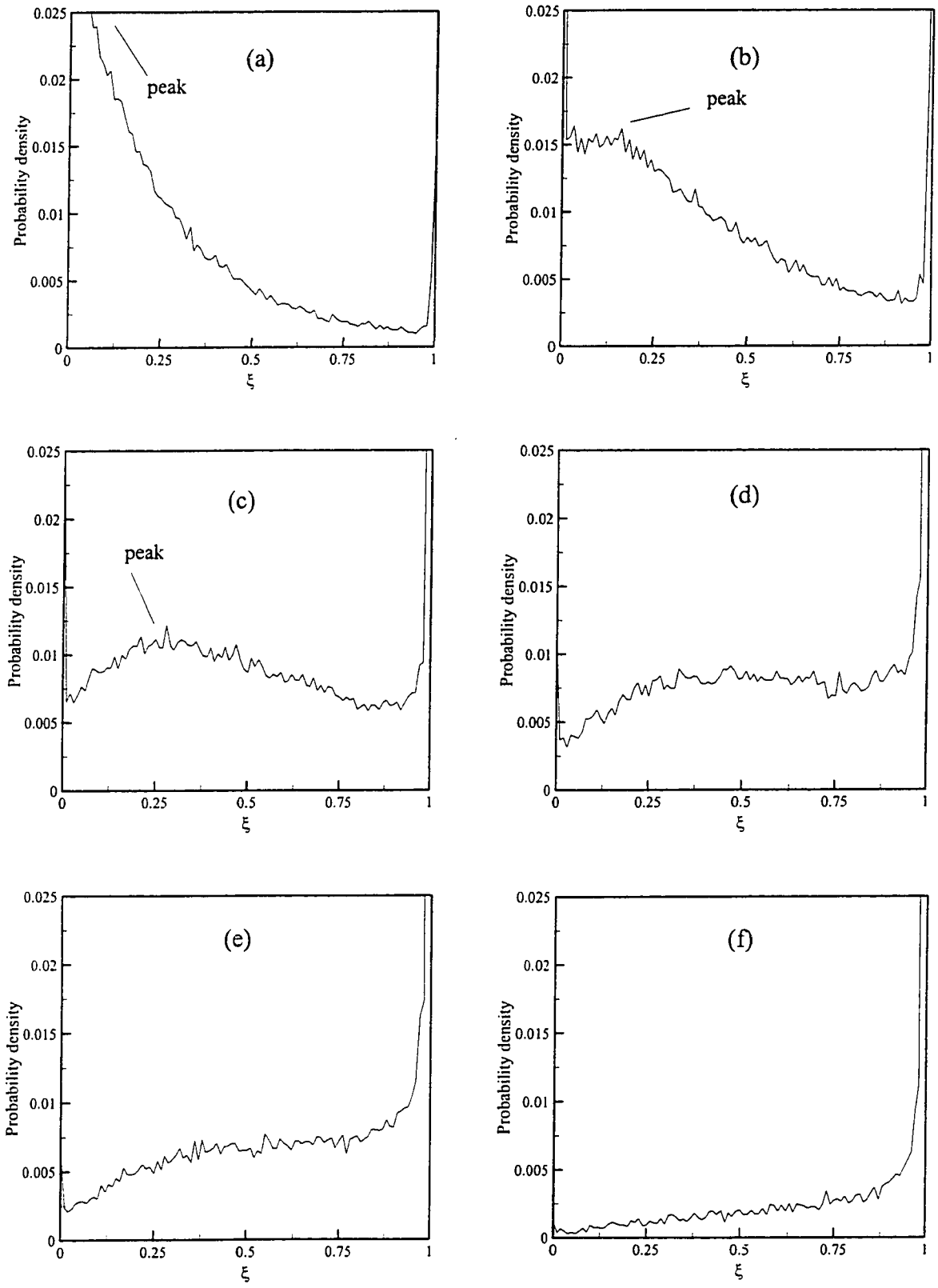

Figure 5.29: PDF shape of passive scalar at several cross-stream locations, for downstream station x=24cm (x/H=0.75). a) η_c=0.054; b) η_c=0.024; c) η_c=0.002; d) η_c=-0.01; e) η_c=-0.02; f) η_c=-0.035.

Chapter 6

Conclusions and Recommendations

6.1 Conclusions

The turbulent flow characteristics for the two-dimensional spatially growing mixing layer are well predicted by the vortex-in-cell (VIC) method. The mean velocity and r.m.s. longitudinal fluctuations in the simulations' region of similarity show a good agreement with the experimental measurements of Masutani & Bowmann (1986). Data for comparison of the r.m.s. lateral velocity fluctuation and the negative cross-stream correlation is not available for the Masutani & Bowmann (1986) experiment, but both show good similarity and have peak values close to the experiment of Oster & Wygnanski (1982) in which a velocity ratio of 0.6 is used. The growth of the momentum thickness $d\theta/dx$ =0.0162 and the growth of the vorticity thickness δ_ω'=0.062 for the simulation, are lower but close to the experimental values of $d\theta/dx$ =0.0165 and δ_ω'=0.0706 , respectively. It is to be noted that the growth of the Masutani & Bowmann (1986) experimental layer is slightly faster than the value measured by the majority of other experiments.

The p.d.f. transport equation using the Monte-Carlo technique is able to predict some

of the features of the scalar field. The mean concentration profiles show that the concentration values in the mixing layer are influenced more by the high speed fluid. Comparison between the mean concentration profile and the mean velocity profile, and the comparison between the spread of concentration and velocity, show that the scalar mixing region extends further into the free stream than does the momentum mixing region, indicating enhanced transport of scalars over momentum. The r.m.s. profiles exhibit mixing asymmetry, with the high speed fluid mixing at a faster rate than the low speed fluid. The asymmetry in the present work, however, is found to be due to the selection of the value of the centre of the hyperbolic tangent profile, used as the inflow boundary condition in the scalar field simulation. The bimodal behaviour in the r.m.s. concentration profile of the Masutani & Bowmann (1986) experiment could not be reproduced in this work, and this is attributed to the use of gradient diffusion hypothesis to model the turbulent transport term, or to the use of inappropriate inflow boundary condition. The p.d.f. shape of the passive scalar shows higher mixed fast stream fluid probabilities over a larger cross-stream extent of the mixing layer as compared with the slow stream fluid, and this indicates that, the mixing layer entrains and subsequently mixes larger volumes of high-speed fluid.

Therefore, it can be concluded that with the VIC technique giving the velocity field, the Monte-Carlo PDF approach is a modelling tool that can be adopted for passive mixing layers. Moreover, it will be very valuable for reactive mixing layers as there is no closure needed for the chemical source term.

6.2 Recommendations

Though this study could predict the scalar statistics quite well, it could not reproduce the bimodal behaviour in the r.m.s. scalar fluctuation. The following aspects could be looked into to improve the results as regards to bimodal behaviour.

1) The turbulent transport term could use instantaneous velocity fluctuations given by the VIC method, instead of using gradient-diffusion model for the term.

2) To close the mixing term in eq.(4.1), the Linear Mean Square Estimation (LMSE) model may be used. Unlike the Curl and modified Curl mixing models, which are stochastic and discontinuous, the LMSE is deterministic and continuous. The model assumes that the molecular mixing has the effect of driving each particle towards the mean.

3) A different approach may be used to compute the mixing frequency. Numerical study of Vanormelingen and Bulck (1999) established, that a substantial non-uniform variation of the mixing frequency with the lateral distance, is needed to produce the bimodal behaviour in the r.m.s. concentration profiles.

4) Investigate various inflow boundary conditions, such as forcing the edge of splitter plate, or adding the wake effect generated by the splitter plate as suggested by Sandham and Reynolds (1989)

With the Monte-Carlo PDF approach established as a valuable modelling tool for passive mixing layers, an isothermal fast chemical reaction may be added. This approach does not require any closure for the chemical source term.

References

Abdolhosseini, R. and Milane, R., 2000, On the effect of Vortex Grid Density in the Vortex-in-Cell Simulation of Mixing Layer, IJCFD 2000, v. 13, pp. 161-183.

Abdolhosseini, R. and Milane, R., 1998, Vortex-in-Cell Simulation of Spatially Growing Mixing Layer, Mechanics Research Communications, v. 25, No. 3, pp. 237-244.

Abdolhosseini, R., 2000, PhD thesis, University of Ottawa.

Abernathy, F. H. and Kronauer, R. E., 1962, The Formation of Vortex Sheets, J. Fluid Mech., v.13, pp. 1-20.

Antonopoulos-Domis, M., 1981 Large-Eddy Simulation of a Passive Scalar in Isotropic Turbulence, J. Fluid Mech. v. 104, pp. 55-79.

Aref, H. and Siggia, E. D., 1980 Vortex Dynamics of the Two Dimensional Turbulent Shear Layer, J. Fluid Mech. 100, pp.705-737.

Ashurst, W. T., 1979 Numerical simulation of Turbulent Mixing Layer Via Vortex Dynamics, Turbulent Shear Flows I, (Ed.) Durst et al., Springer-Verlag, New York, 402-413.

Bray, K. N. C., 1973 Equations of Turbulent Combustion I. Fundamental Equations of Reacting Turbulent Flows. AASU report 330 (1973).

Baker, G. R., 1979 The Cloud-in-Cell Technique Applied to the Roll-Up of the Vortex Sheets, J. Comput. Phys., v.31, pp. 76-95.

Bardina, J., Ferziger, J. H. and Reynolds, W. C., 1980 Improved Subgrid-Scale Model for Large Eddy Simulation, AIAA Pap. 80- 1357.

Batchelor, G, K., 1967 An Introduction to Fluid Dynamics, Cambridge University Press.

Batt, R. G., 1977, Turbulent Mixing of Passive and Chemically Reacting Species in a Low-Speed Shear Layer, J. Fluid Mech., v 82, pp. 53-89.

Bilger, R. W., 2000, Future progress in turbulent combustion research, Progress in Energy & Combustion Science, v 26 n 4, pp. 367-380.

Broadwell, J. E., Breidenthal, R., 1982, A simple Modeling of Mixing and Chemical Reaction in a Turbulent Shear Layer, J. Fluid Mech. V 125, pp. 397-410.

Brown, G. L. and Roshko, A., 1974 On Density Effects and Large Structure in Turbulent Mixing Layers, J. Fluid Mech., 57, pp. 785-796.

Chorin, A. J., 1973 Numerical Study of Slightly Viscous Flow, J. Fluid Mech., vol. 57, pp.785-796.

Chow, C. Y., 1979, An Introduction to Computational Fluid Mechanics. John Wiley.

Christianson, J. P., 1973 Numerical Simulation of Hydromechanics by the Method of Point Vortices, J. Comput. Phys., v.13, pp. 363-379.

Clemens, N. T. and Paul, P. H., 1992, Evolution of Mixing Fraction PDFs in an Axisymmetric Mixing Layer, Bull. Amer. Phys. Soc., Series II, v 37.

Clements, R. R. and Maull, D. J., 1975 The Representation of Sheets of Vorticity by Discrete Vortices, Prog. Aerospace Sci., v.16, pp. 129-146.

Corcos, G. M. and Sherman, F. S., 1984 The Mixing Layer: Deterministic Model of a Turbulent flow, J. Fluid Mech., v.139, pp. 29-65.

Dopazo, C. and O'Brien, E. E., Combust. Sci. Technol. v.13, p. 99.

Dopazo Cesar, 1994, Recent developments in pdf methods. Turbulent Reactive Flows, ISBN 0-12-447945-6.

Feiereisen, W. J., Reynolds, W. C. and Ferziger, J. H., 1981 Numerical Simulation of a Compressible, Homogeneous, Turbulent Shear Flow. Department of Mech. Engng. Rep. TF-13, Stanford University, Stanford, California.

Felici, H. M., 1995 Eulerian/Lagrangian Coupling Procedure for Three-Dimensional Vortical Flows, AIAA journal, v.33, No. 1, pp. 48-55.

Ghoniem, A. F. Heidarinejad, G., Krishnan, A. 1987 Numerical Simulation of Reacting Shear Layer Using the Transport Element Method, AIAA/SAE/ASME/ASEE, AIAA-87-1718 Joint Propulsion Conference.

Ghoniem, A. F. Heidarinejad, G., 1990 Effect of Two-Dimensional Shear Layer Dynamics on Mixing and Combustion at Low Heat Release, Combust. Sci. Technol., v. 72, pp. 79-99

Ghoniem, A. F. and Ng, K. K., 1986 Effect of Harmonic Modulation on Rates of Entrainment in a Confined Shear Layer, AIAA Pap. 86-0056.

Givi, P. and Jou, W. H., 1986 Mixing and Chem. Reac. In a Spat. Dev. Mixing Layer, Pap. Spring Tech. Meeting, Combust. Inst. Centr. St. Sec.

Hawthorne, W. R., Weddell, D. S. and Hottel, H. C., 1949 Third Symposium on Combustion, Flame and Explosion Phenomena. pp. 266

Greengard, C., 1985 The Core Spreading Vortex Method Approximates the Wrong Equation, J. Comput. Phys., v.61, p. 345.

Hinze, J. O., 1975 Turbulence, Second edition, McGraw-Hill Inc.

Ho, C. M. and Huerre, P., 1984 Perturbed Free Shear Layers, Ann. Rev. Fluid Mech., v.16, pp. 365-424.

Inoue, O., 1985 Vortex Simulation of a Turbulent Mixing Layer, AIAA J., vol. 23(3), p. 367.

Inoue, O., 1992 Double Frequency Forcing on Spatially growing mixing layers, J. Fluid Mech., v.234, pp. 553-581.

Inoue, O. and Leonard, A., 1987 Vortex Simulation of Forced/Unforced Mixing Layers, AIAA J. vol. 26(11), p.1417.

Jacobitz, F., Sarkar, S. And Van Atta, C., 1997, Direct Numerical Simulation of the Turbulence Evolution in a Uniformly Sheared and Stably Stratified Flow, J. Fluid Mechanics, v. 342, pp. 231-261.

Karasso, P.S. and Mungal, M.G., 1997, Scalar mixing and reaction in plane liquid shear layer, J. Fluid Mech. V. 323, pp. 23-63.

Karnik, U. and Tavoularis, S., 1987 Generation and Manipulation of Uniform Shear with the Use of Screens, Exper. Fluids, v.5, pp. 247-254.

Kida, S. and Tanaka, M., 1994, Dynamics of Vortical Structures in a Homogeneous Shear Flow, J. Fluid Mechanics, v. 274, pp. 43-68.

Kim, J. and Moin, P., 1989 Transport of Passive Scalar in a Turbulent Channel Flow. Turbulent Shear Flow 6, Springer-Verlag, Berlin, Heidelberg.

Knio, O. M. and Ghoniem, A. F., 1988 On the Formation of Streamwise Vorticity in Turbulent Shear Flows, AIAA Pap. 88-0728.

Kollmann, W. and Janica, J., 1982 The Probability Density Function of a Passive Scalar in Turbulent Shear Layer, Phys. Fluids, v. 25(10), pp. 1755-1769.

Konrad, J. H., 1976 An Experimental Investigation of Mixing in Two-Dimensional Turbulent Shear Flows With Applications to Diffused-Limited Chemical Reactions, Technical report CIT-8-PU.

Koochesfahani, M. M., 1984 Experiments on Turbulent Mixing and Chemical Reactions in a Liquid Mixing Layer, Ph.D. Thesis, California Institute of Technology.

Koumoutsakos, P. D., 2000 Vortex methods: theory and practice. Cambridge University Press.

Kuwahara, K. and Takami, H., 1983 Study of Turbulent Wake Behind Bluff Body by Vortex Method, Proceeding of IUTAM Symposium on Turbulence and Chaotic Phenomena in Fluids, Edited by T. Tatsumi, North Holland Publishing Corp., Amsterdam.

Launder, B. E. and Spalding, D. B., 1972 Mathematical Models of Turbulence, Academic Press.

Libby, P. A. and Williams, F. A., 1980 Turbulent Reactive Flows, Springer-Verlag 113.

Lee, M. J., Kim, J. and Moin, P., 1990 Structure of Turbulence in High Shear Rate, J. Fluid Mech., v.216, pp. 561-583.

Leonard, A.,1974 Energy Cascade in Large Eddy Simulation of Turbulent Fluid Flows, Advances in Geophys., 18A, pp. 237-248.

Leonard, A., 1980 Vortex Methods for flow Simulations, J. Comput. Phys., vol. 37(3), p.289.

Lesieur, M. R., 1995 Mixing layer Vortices, S. I. Green(ed), Fluid Vortices, pp. 35-63.

Leslie and Quarini, 1979 The Application of Turbulent Theory to the Formation of Subgrid Modelling Procedures, J. Fluid Mech., v.91, pp. 65-91.

Lilly, D. K., 1967 The Representation of Small-Scale Turbulence in Numerical Simulation Experiments, Proc. IBM Sci. Comput. Symp. Environ. Sci., IBM Data Process. Div., White Plain, N.Y. pp. 195-210.

Lin, P. and Pratt, D. T., 1987 Numerical Simulation of a Plane Turbulent Mixing Layer, with Applications to Isothermal, Rapid Reactions, AIAA Pap. 87-0224.

Lockwood, F. C. and Naguib, A. S., 1975 Combust. Flame 24, p.109.

Lundgren, T. S., 1969 Phys. Fluids 12, p.485.

Mansour, N. N., 1985, A Hybrid Vortex-in-Cell Finite Difference Method for shear Layer Computations, AIAA Paper, 85-0372

Masutani, S. M. and Bowmann, C. T., 1986, The structure of a chemically reacting plane mixing layer, J. Fluid Mech., v.172, pp. 93-126

Meyer, T. R., Dutton, J. C. and Lucht R. P., 2001, Turbulent Molecular Mixing in Fully-Developed Planar Shear Layers, 39th AIAA Aerospace Sciences Meeting, AIAA Paper No. 2001-0287. Pp. 1-11.

Milane, R. and Nourazar, S., 1997, Large-Eddy Simulation of Mixing Layer using Vortex Method: Effect of Subgrid-Scale Model on Early Development, Mechanics Research Communications, v. 24, No. 2, pp. 215-221.

Milane, R. and Nourazar, S., 1995, On the Turbulent Diffusion Velocity in Mixing Layer Simulated using the Vortex Method and the Subgrid Scale Vorticity Model, Mechanics

Research Communication, v.22, No. 4, pp. 327-333.

Nakamura, Y., Leonard A., and Spalart, P., 1982 Vortex Simulation of an Invicid Shear Layer, AIAA Pap. 82-0948.

Ng, K. K. and Ghoniem, A. F., 1985 Numerical Simulation of a Confined Shear Layer, 10th Int. Colloquium on the Dynamics of Explosions and Reactive Systems, CA. Aug. 4-9.

Ogami, Y. and Akamatsu, T., 1991 Viscous Flow Simulation Using the Discrete Vortex Model- The Diffusion Velocity Method, Computers and Fluids, v.19, pp. 433-441.

Oster, D. and Wygnanski, I., 1982 The forced Mixing Layer Between Parallel Streams, J. Fluid Mech., 123, pp. 91-130.

Pope, S. B., 1976, Combust. Flame v. 27, p. 299.

Pope, S. B., 1980, MIT Report EL-80-012.

Pope, S. B., 1981, A Monte Carlo Method for the PDF Eqn. Of Turb. Reac. Flow, Combust. Sci. Technol.,v. 25, pp.159-174

Pope, S. B., 1985, Prog. Energ. Combust. Sci., v.11, pp.119.

Pope, S. B., 2000, Turbulent Flows, Cambridge Univ Press.

Phillips, O. M., 1969 Shear flow Turbulence, Ann. Rev. Fluid Mech., v.1, pp. 245-264.

Rai, M. M. and Moin, P., 1989 Direct Simulation of Turbulent Flow Using Finite Difference Schemes. AIAA Pap. 89-0369.

Reynolds, W. C., 1990 Turbulence at the Crossroads, Springer-Verlag, pp. 314-343.

Riley, J. J., Metcalfe, R.W. and Orszag, S. A., 1986 Direct Numerical Simulation of Chemically Reacting Turbulent Mixing Layers, Phys. of Fluids, v.29(2), pp. 406-422.

Rogallo, R., 1981 Numerical Experiments in Homogeneous Turbulence, NASA Technical Memo. 81315.

Rogallo, R. and Moin, P., 1984 Numerical Simulation of Turbulent Flows, Ann. Rev. Fluid Mech., 16, pp. 99-137.

Rogers, M. M. and Moin, P., 1987 The Structure of Vorticity Field in Homogeneous Turbulent Flows, J. Fluid Mech., v.176, pp. 33-66.

Rogers, M. M. and Moser, R. D., 1994, Direct simulation of a self-similar turbulent mixing layer, Phys. Fluids, v. 6 (2), pp. 903-923.

Rosenhead, L., 1931 The Formation of Vortices From Surface of Discontinuity, Proc. Roy. Soc., Series A, v.134, pp. 170-192.

Saffman, P. G., 1981 Dynamics of Vorticity, J. Fluid Mech., v.106, pp. 49-58.

Sandham, N. and Reynolds, W. C., 1989 Some Inlet-Plane Effects on the Numerically Simulated Spatially-Developing Mixing Layer, Turbulent Shear Flows 6, Springer-Verlag Berlin Heidelberg, pp. 442-454.

Sarpkaya, E., 1994, Advances in Applied Mathematics, v.31, pp. 113-247.

Schlichting, H., 1968 Boundary Layer Theory, McGrow Hill.

Shirani, E., Ferziger, J. H. and Reynolds, W. C., 1981 Mixing of a Passive Scalar in Isotropic and Sheared Homogeneous Turbulence, Dept. Mech. Engng., Rep. TF-15, Stanford University, Stanford, California.

Sivathanu, Y. R. and Gore, J. P., 1994, Discrete probability function method for a turbulence mixing layer. Fire, Combustion, and Hazardous Waste Processing, ASME Heat Transfer Division Publication, v 296, pp.99-106.

Smagorinski, J., 1963 General Circulation Experiment with the Primitive Equations I, The Basic Experiment, Mon. Wether Rev. 91, pp. 99-164.

Souza, F., 1993 Experiments in Highly Sheared Nearly Homogeneous Turbulence, M.Sc. Thesis, Dept. Mech. Engng., Univ. Ottawa, Ottawa, Canada.

Spencer, B. W. and Jones, B. G., 1971 Stat. Invest. Of Pres. & Vel. Fields in Turb. Two-Stream Mix. Layer, AIAA 4th Fl. And Plasma Dyn. Conf.

Tavoularis, S., 1985 Asymptotic Laws for Transversely Homogeneous Turbulent Shear Flows. Phys. Fluids, 28(3), pp. 999-1001.

Tavoularis, S. and Corrsin, S., 1981, Experiments in Nearly Homogeneous Turbulent Shear Flow with a Uniform Mean Temperature Gradient. Part 1. J. Fluid Mech., v. 104, pp. 311-347.

Tavoularis, S. and Corrsin, S., 1981, Experiments in Nearly Homogeneous Turbulent Shear Flow with a Uniform Mean Temperature Gradient. Part 2. J. Fluid Mech., v. 104, pp. 349-367

Tavoularis, S. and Karnik, U., 1989 Further Experiments on the Evolution of Turbulent Stresses and Scales in Uniformly Sheared Turbulence, J. Fluid Mech., v.204, pp. 457-478.

Tennekes, H. and Lumley, J. L. , 1977 A First Course in Turbulence, MIT Press, Cambridge, Mass.

Townsend, A. A., 1976 The Structure of Turbulent Shear Flow 2nd ed., Cambridge University Press.

Vanormelingen, J. and den Bulck, E. Van., 1999, Scalar Transport in plane mixing layers,

Heat & Mass Transfer, v.35 n.5, pp. 383-390.

Warhaft, Z., 2000, Passive scalars in turbulent flows, Annual Review of Fluid Mechanics, v 32, pp. 203-240.

Wilcox, D. C., 1993 Turbulent Modelling for CFD, DCW Industries, La Canada, CA.

Yanenko, N. N., 1971 The Methods of Fractional Steps, Springer Verlag.

Zhou, X. Y. and Pereira, J. C. F., 2000, Large eddy simulation (2D) of a reacting plane mixing layer using filtered density function closure. Flow, Turbulence & Combustion, v 64 n 4 , pp. 279-300.

Appendix

Appendix A

This simulation work uses two main programs and two post processing programs given below:

1) vic.f: This main program does the vortex-in-solution of the mixing layer, and generate the flow field. The data files written are, p483022B.dat, eddy.dat, p482508.dat, with variables, U, V, ν_T, ϵ/k, Ω, θ, u', v', $u'v'$, $\partial U/\partial y$.

2) vicPP.f90 : A post-processing program for the flow field. It reads output data files of vic.f, computes the similarity variable η_ν, vorticity thickness, velocity spread, filters ν_T and writes data for plotting vs. η_ν. The output is to files eddyC.dat, momThickness.dat and momSlope.dat, MeanVel.dat, stats.dat, statsC.dat, vortTh2.dat, velSpread.dat.

3) pdf.f90 : This second main program does the Monte-Carlo simulation of the pdf transport equation. Reads the data files p483022B.dat, eddyC.dat, p482508.dat, for variables, U, V, ν_T, ϵ/k, θ. Every 1000 steps write out scalar statistics to new data files rms{step number}.dat, pdf{step number}.dat.

4) scalarPP.f90 : Post processing of the Monte-Carlo simulation, reads output data files of pdf.f90, computes the similarity variable η_c, concentration spread, and writes scalar statistics for plotting vs. η_c. The output is to files MeanConc.dat. RMSConc.dat, UM.dat, Mean_Flow.dat, Mean_Scalar.dat, concSpread.dat, scalarPdf.dat.

The flow charts for these programs follows:

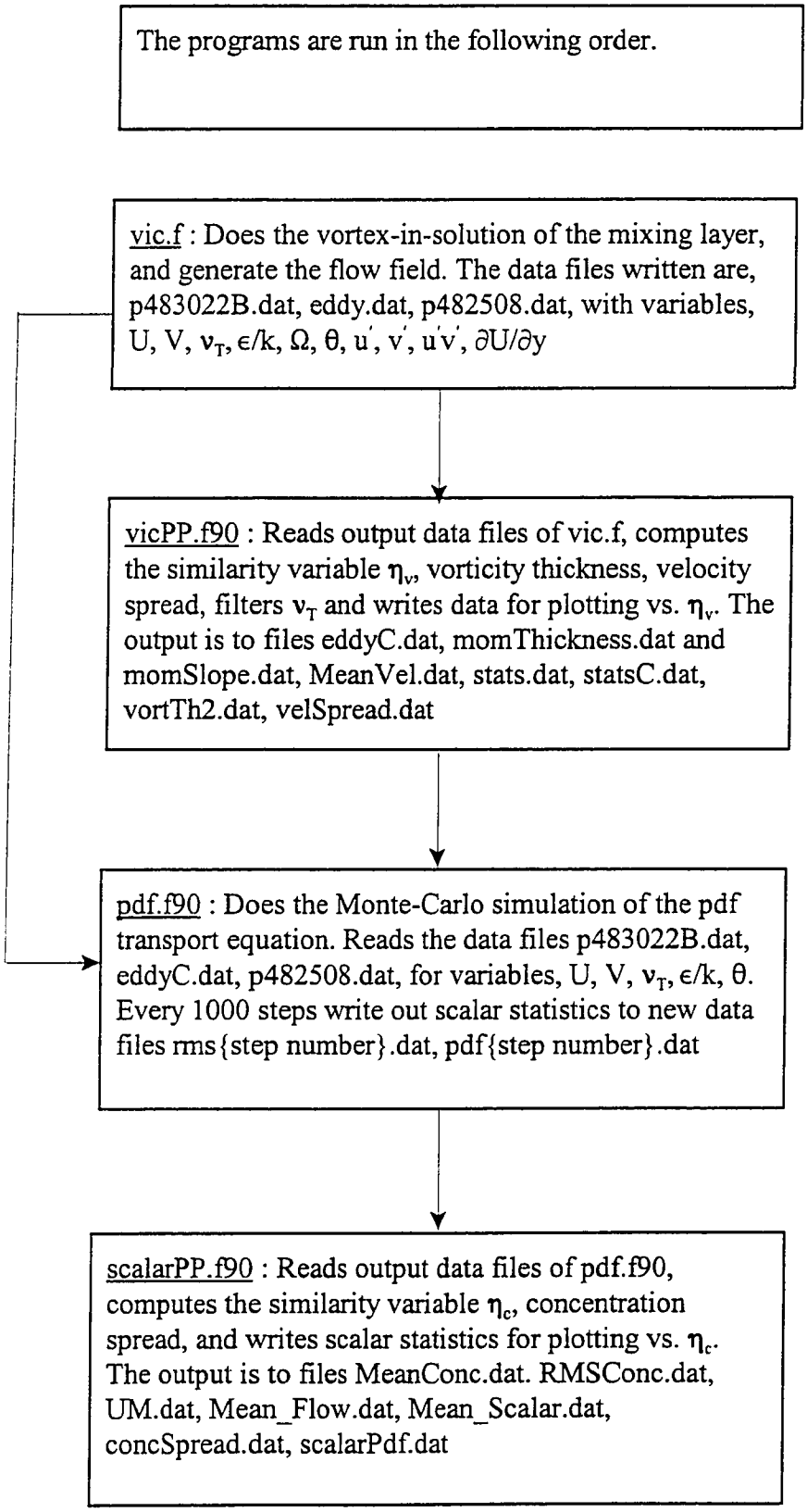
The programs are run in the following order.
vic.f : Does the vortex-in-solution of the mixing layer, and generate the flow field. The data files written are, p483022B.dat, eddy.dat, p482508.dat, with variables, U, V, ν_T, ϵ/k, Ω, θ, u', v', u'v', $\partial U/\partial y$
vicPP.f90 : Reads output data files of vic.f, computes the similarity variable η_v, vorticity thickness, velocity spread, filters ν_T and writes data for plotting vs. η_v. The output is to files eddyC.dat, momThickness.dat and momSlope.dat, MeanVel.dat, stats.dat, statsC.dat, vortTh2.dat, velSpread.dat
pdf.f90 : Does the Monte-Carlo simulation of the pdf transport equation. Reads the data files p483022B.dat, eddyC.dat, p482508.dat, for variables, U, V, ν_T, ϵ/k, θ. Every 1000 steps write out scalar statistics to new data files rms{step number}.dat, pdf{step number}.dat
scalarPP.f90 : Reads output data files of pdf.f90, computes the similarity variable η_c, concentration spread, and writes scalar statistics for plotting vs. η_c. The output is to files MeanConc.dat. RMSConc.dat, UM.dat, Mean_Flow.dat, Mean_Scalar.dat, concSpread.dat, scalarPdf.dat

vic.f:
Flow chart for the main flow program

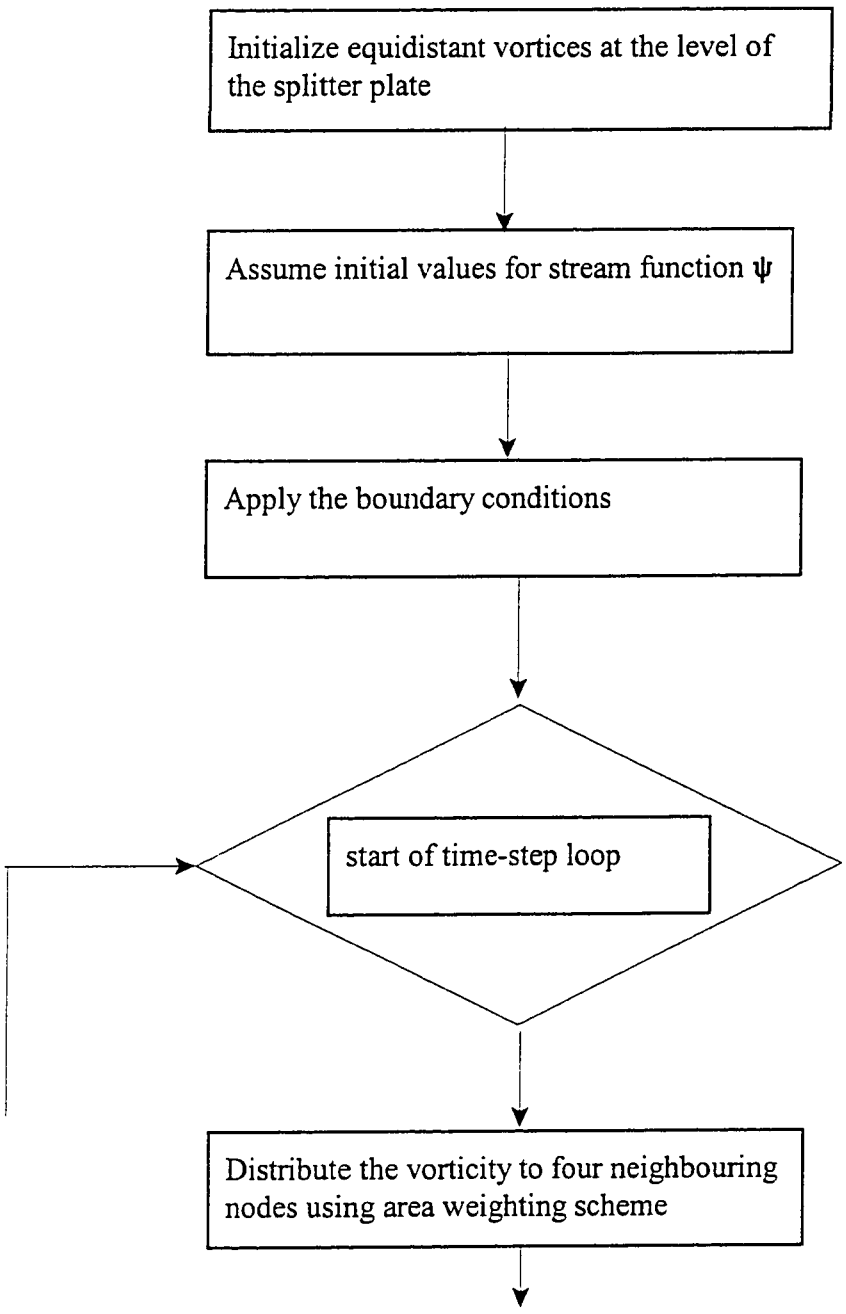

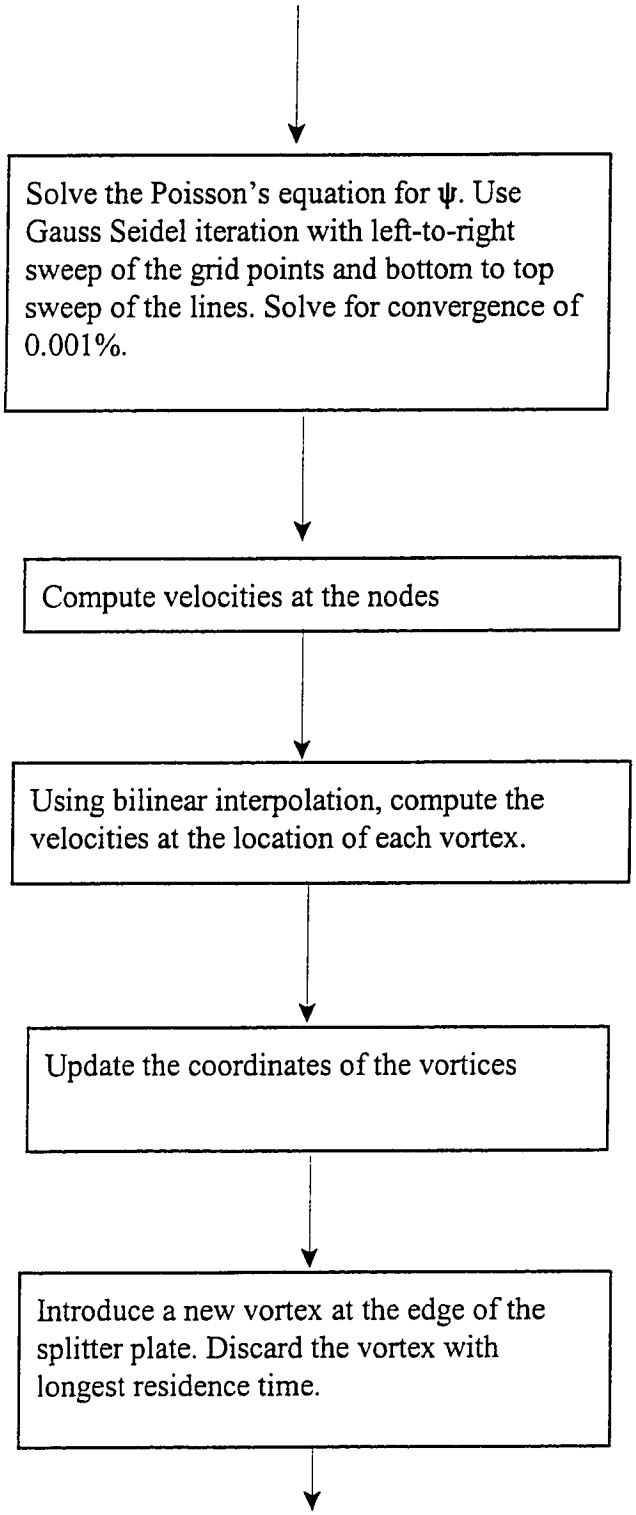
Solve the Poisson's equation for ψ. Use Gauss Seidel iteration with left-to-right sweep of the grid points and bottom to top sweep of the lines. Solve for convergence of 0.001%.
Compute velocities at the nodes
Using bilinear interpolation, compute the velocities at the location of each vortex.
Update the coordinates of the vortices
Introduce a new vortex at the edge of the splitter plate. Discard the vortex with longest residence time.

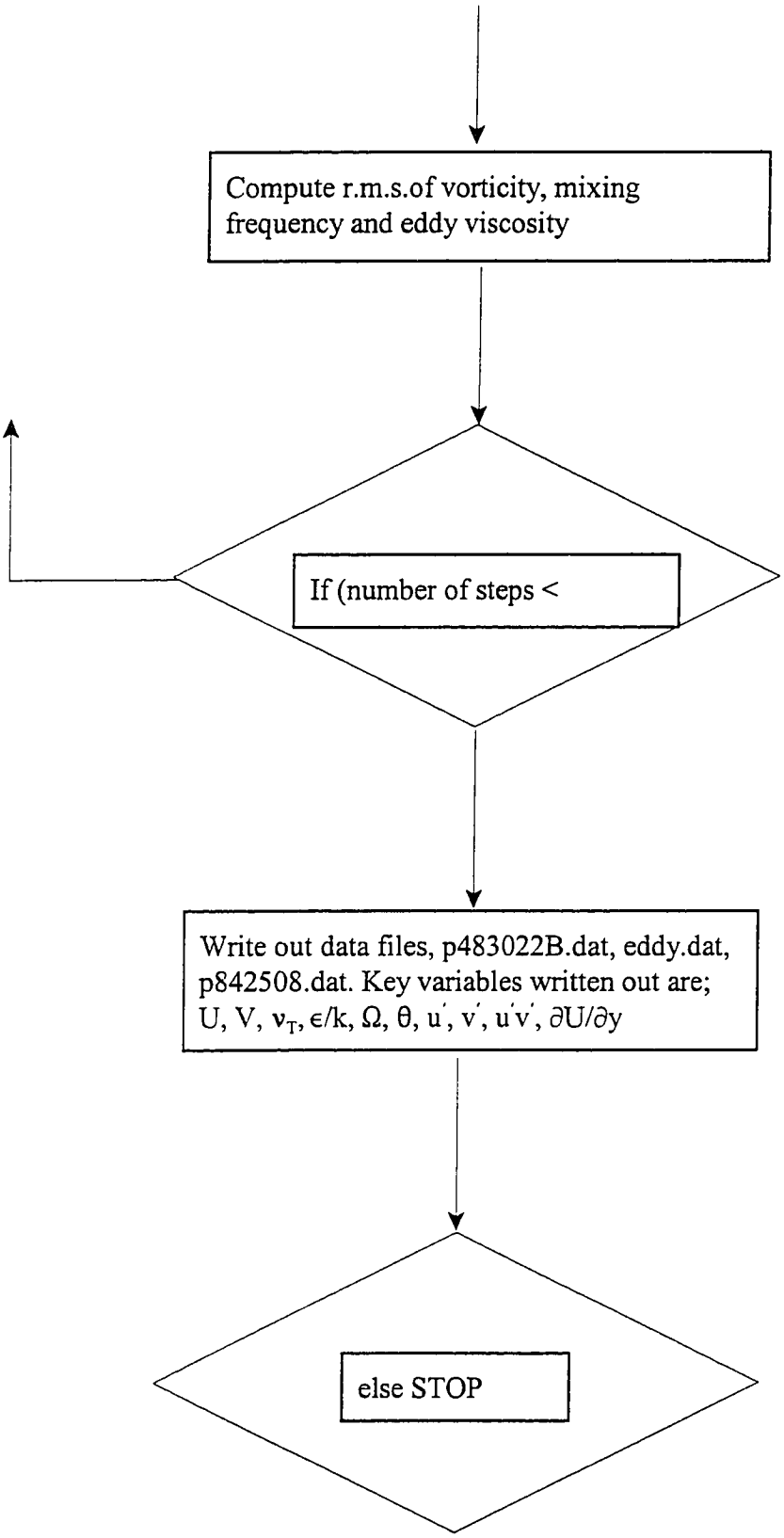
Compute r.m.s.of vorticity, mixing frequency and eddy viscosity
If (number of steps <
Write out data files, p483022B.dat, eddy.dat, p842508.dat. Key variables written out are; U, V, ν_T, ϵ/k, Ω, θ, u', v', u'v', $\partial U/\partial y$
else STOP

vicPP.f90:
The program post processes the data of main flow program vic.f, computes similarity variable, vorticity thickness, and write data files for plotting.

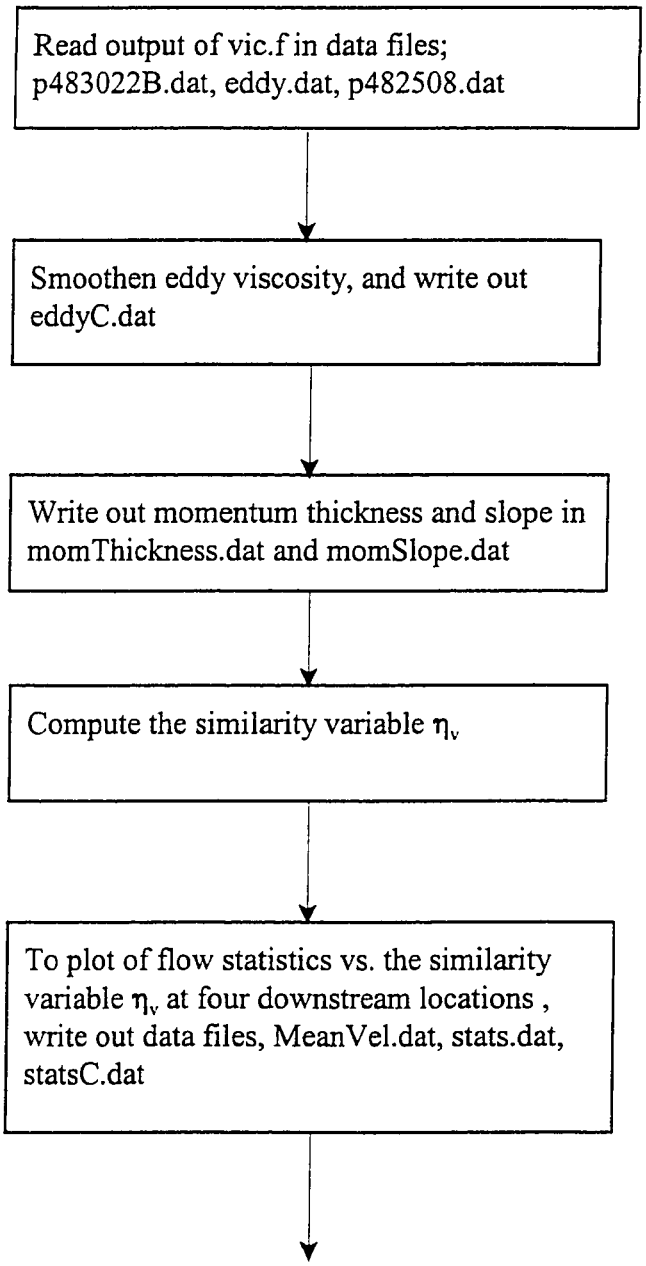

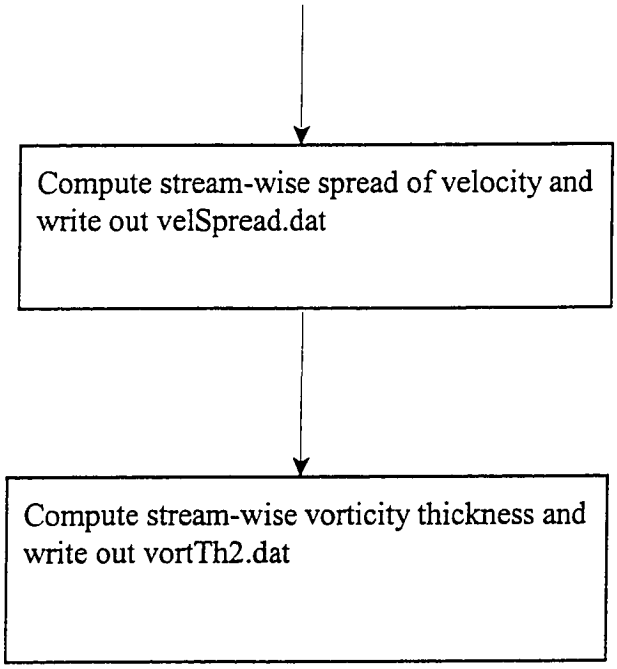
Compute stream-wise spread of velocity and write out velSpread.dat
Compute stream-wise vorticity thickness and write out vortTh2.dat

pdf.f90:
Flow chart for main program doing PDF computation using MonteCarlo technique

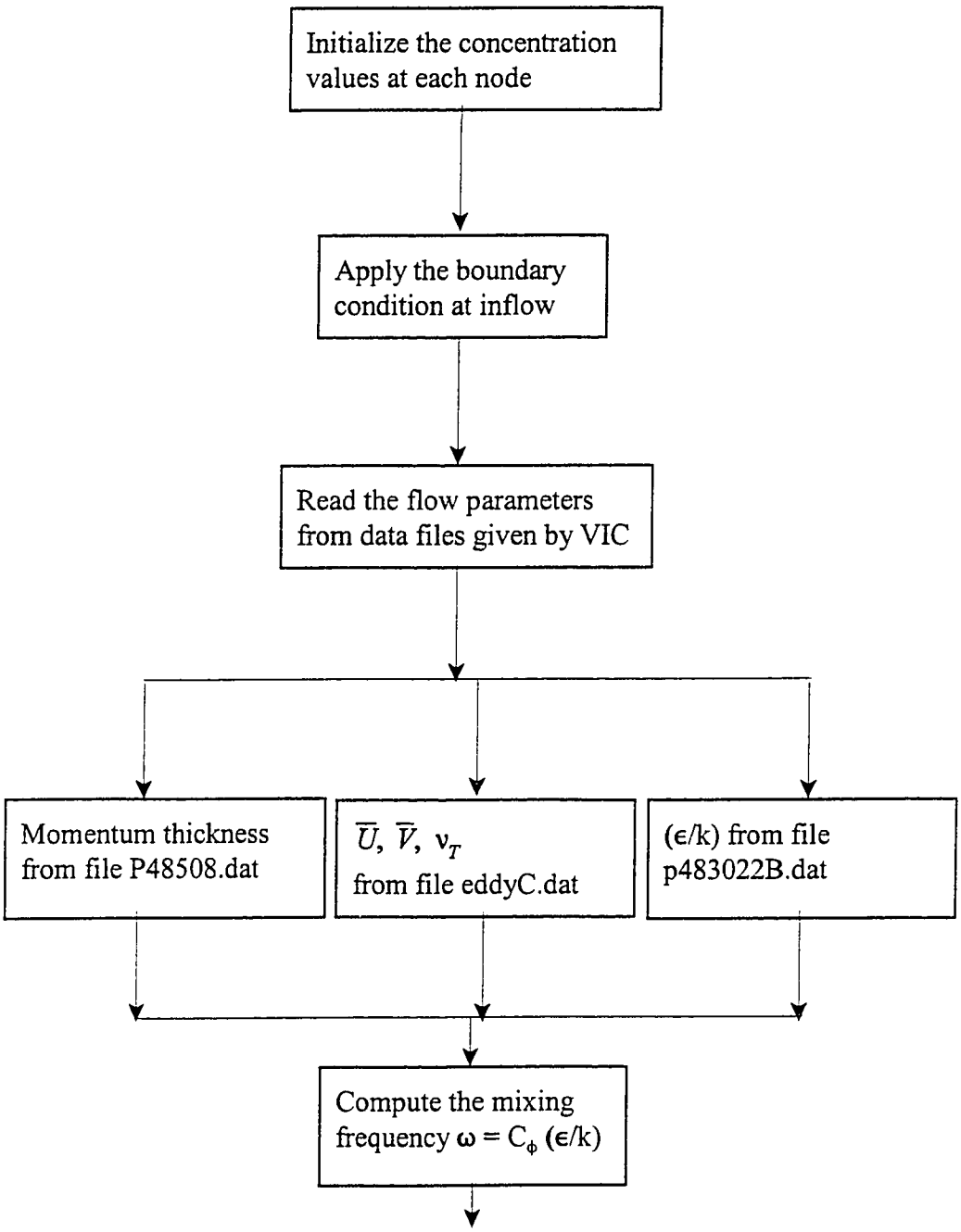

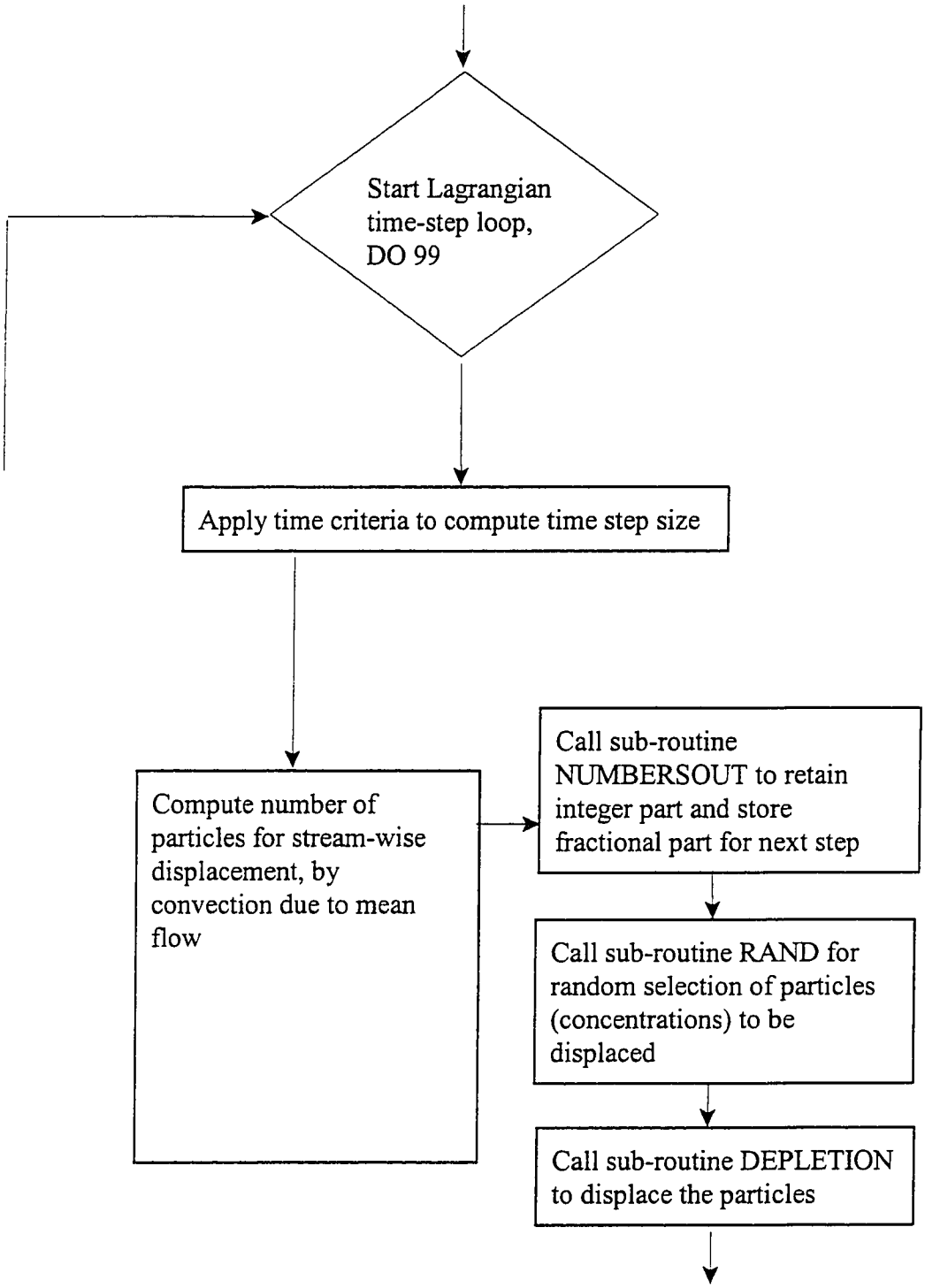
Start Lagrangian time-step loop, DO 99
Apply time criteria to compute time step size
Compute number of particles for stream-wise displacement, by convection due to mean flow
Call sub-routine NUMBERSOUT to retain integer part and store fractional part for next step
Call sub-routine RAND for random selection of particles (concentrations) to be displaced
Call sub-routine DEPLETION to displace the particles

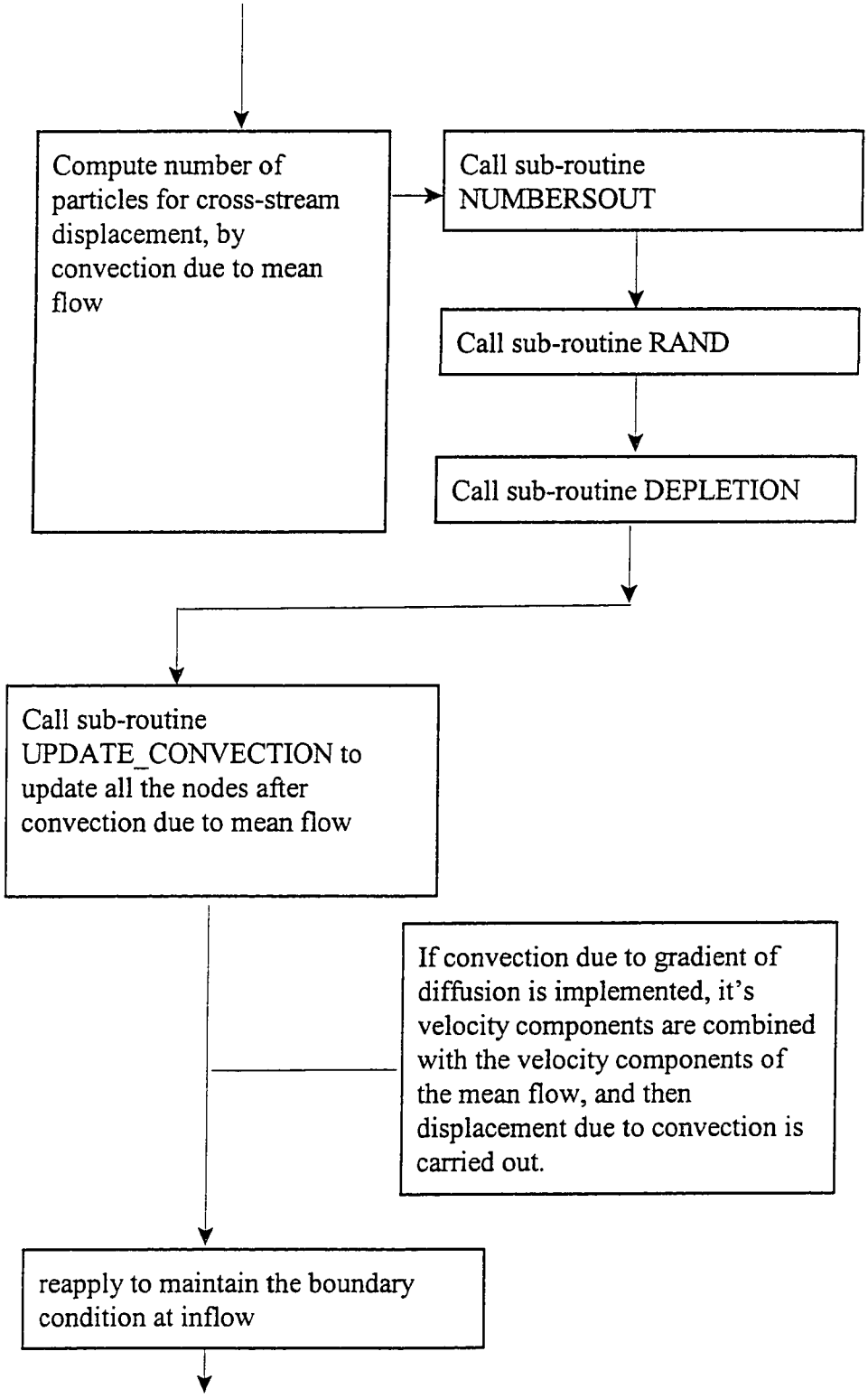
Compute number of particles for cross-stream displacement, by convection due to mean flow
Call sub-routine NUMBERSOUT
Call sub-routine RAND
Call sub-routine DEPLETION
Call sub-routine UPDATE_CONVECTION to update all the nodes after convection due to mean flow
If convection due to gradient of diffusion is implemented, it's velocity components are combined with the velocity components of the mean flow, and then displacement due to convection is carried out.
reapply to maintain the boundary condition at inflow

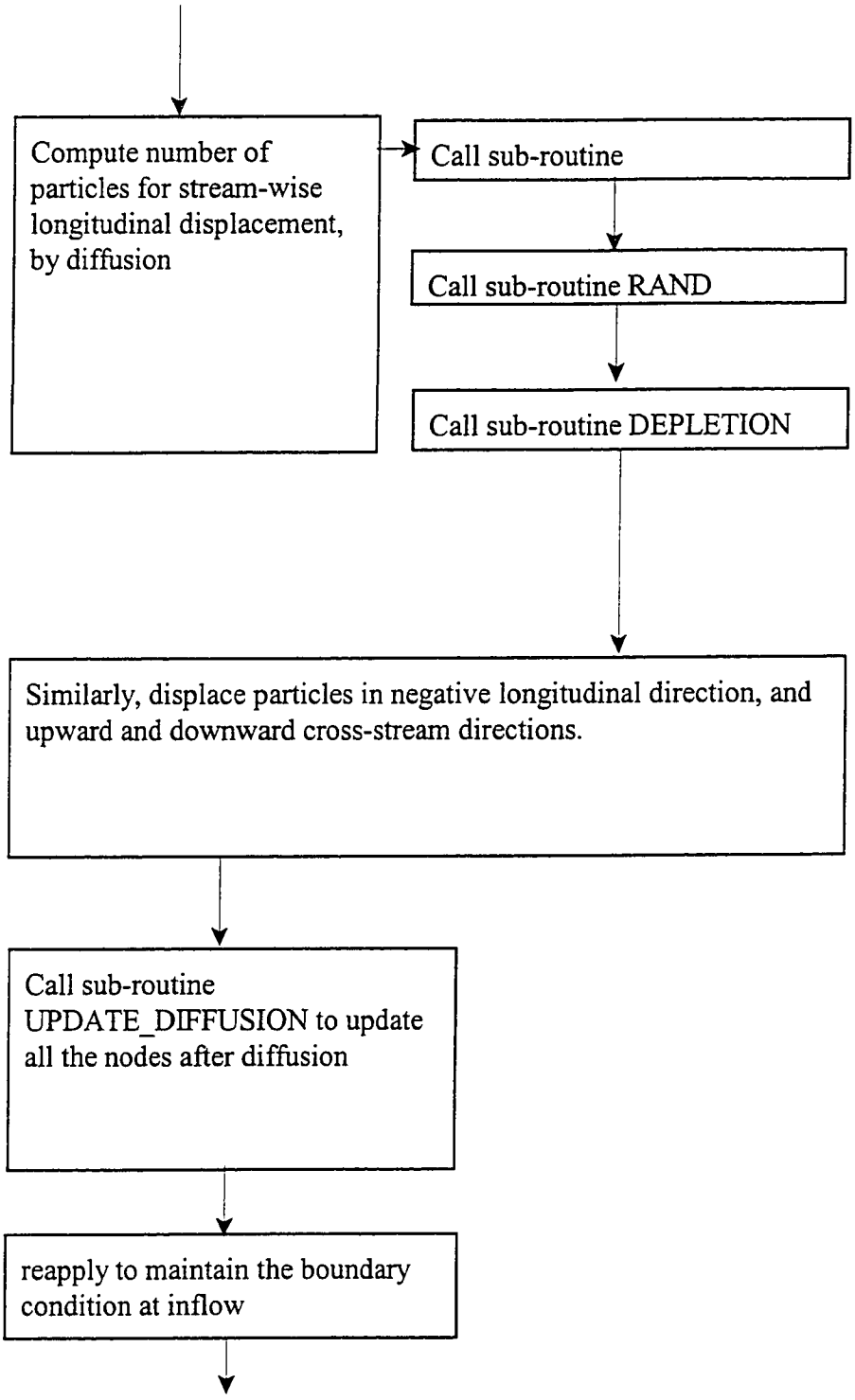
Compute number of particles for stream-wise longitudinal displacement, by diffusion
Call sub-routine
Call sub-routine RAND
Call sub-routine DEPLETION
Similarly, displace particles in negative longitudinal direction, and upward and downward cross-stream directions.
Call sub-routine UPDATE_DIFFUSION to update all the nodes after diffusion
reapply to maintain the boundary condition at inflow

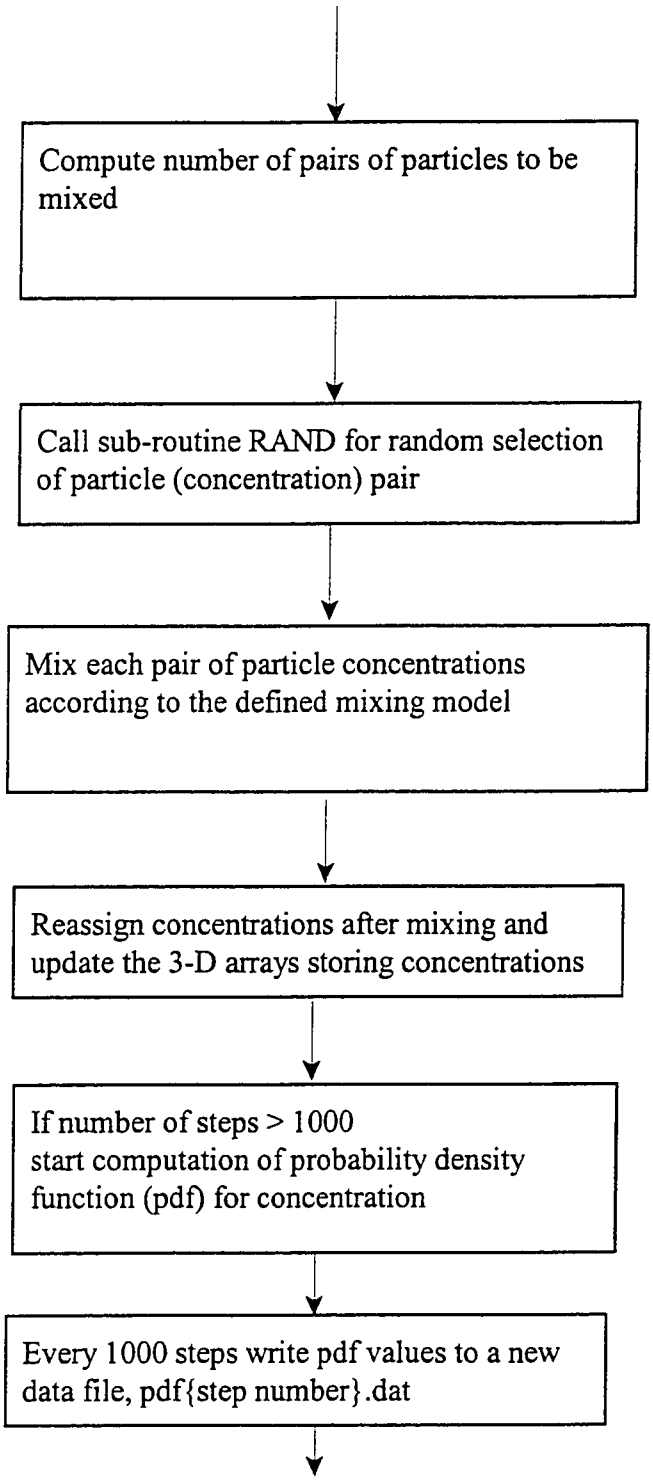
Compute number of pairs of particles to be mixed
Call sub-routine RAND for random selection of particle (concentration) pair
Mix each pair of particle concentrations according to the defined mixing model
Reassign concentrations after mixing and update the 3-D arrays storing concentrations
If number of steps > 1000
start computation of probability density function (pdf) for concentration
Every 1000 steps write pdf values to a new data file, pdf{step number}.dat

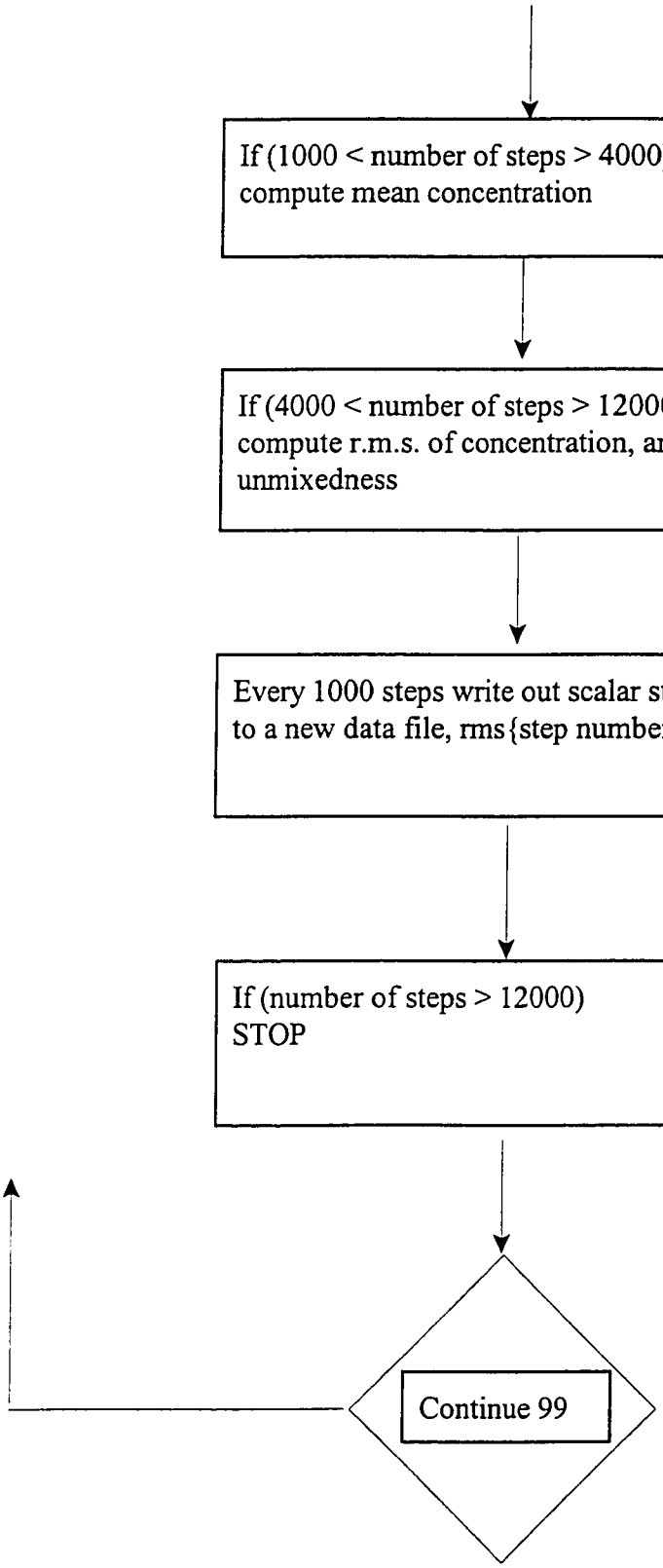
If (1000 < number of steps > 4000)
compute mean concentration
If (4000 < number of steps > 12000)
compute r.m.s. of concentration, and
unmixedness
Every 1000 steps write out scalar statistics
to a new data file, rms{step number}.dat
If (number of steps > 12000)
STOP
Continue 99

scalarPP.f90:
The program post processes the data of main program pdf.f90, and write data files for plotting. Also reads some flow parameters for comparison plots.

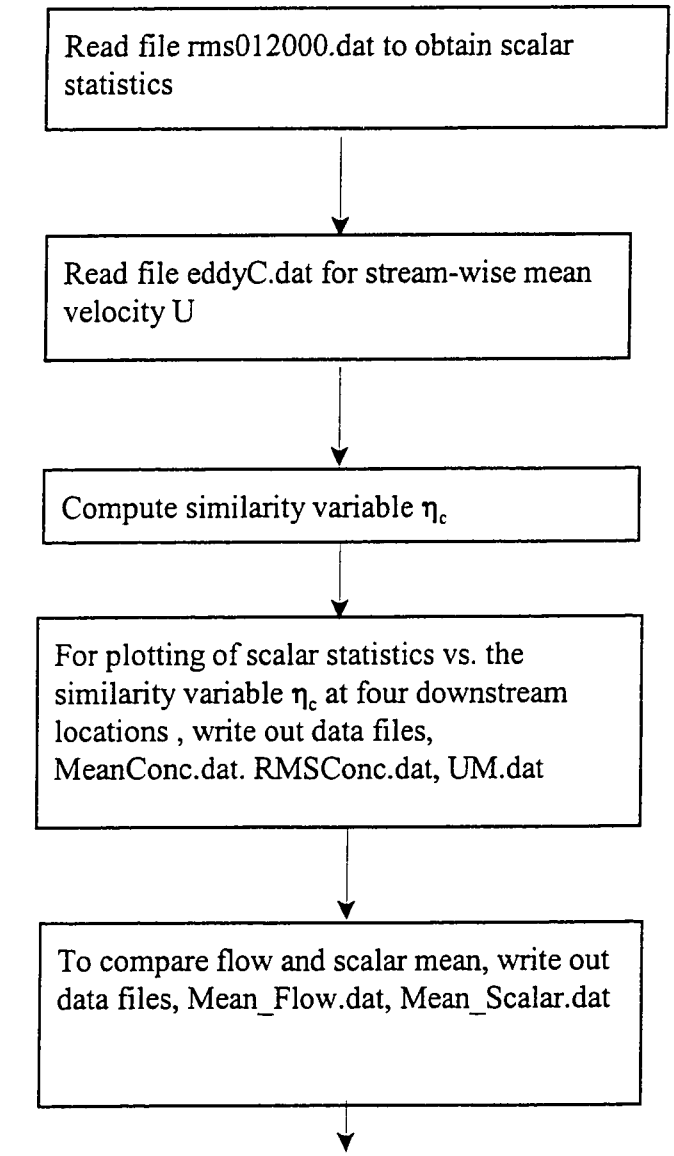

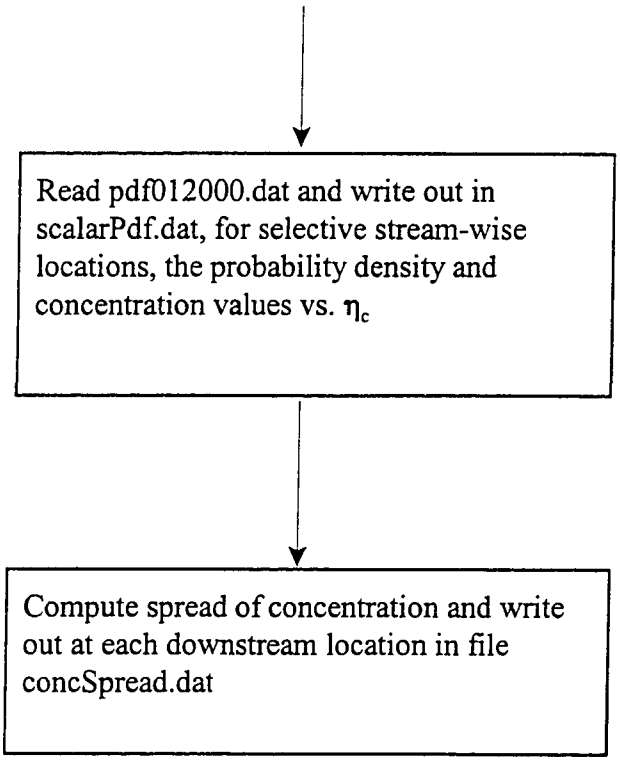
Read pdf012000.dat and write out in scalarPdf.dat, for selective stream-wise locations, the probability density and concentration values vs. η_c
Compute spread of concentration and write out at each downstream location in file concSpread.dat